Title
Photodissociaion Dynamics of Neutral Free Radicals

Author
Negru, Bogdan

Publication Date
2012

Peer reviewed|Thesis/dissertation

Photodissociation Dynamics of Neutral Free Radicals

By

Bogdan Negru

A dissertation submitted in partial satisfaction of the

requirements for the degree of

Doctor of Philosophy

In

Chemistry

in the

Graduate Division

of the

University of California, Berkeley

Committee in charge:

Professor Daniel M. Neumark, Chair

Professor Ronald C. Cohen

Professor Robert Dibble

Fall 2012

Photodissociation Dynamics of Neutral Free Radicals

Abstract

Photodissociation Dynamics of Neutral Free Radicals

By

Bogdan Negru

Doctor of Philosophy in Chemistry

University of California, Berkeley

Professor Daniel M. Neumark, Chair

Photofragment translational spectroscopy was used to study the photodissociation dynamics of the phenyl and *tert*-butyl radicals. These radicals were produced in a collisionless environment from the flash pyrolysis of the appropriate precursor, nitrosobenzene for phenyl and azo-*tert*-butane for the *tert*-butyl radical. The photodissociation dynamics of the phenyl radical (C_6H_5) were investigated at 248 and 193 nm. At 248 nm, the only dissociation products observed were from hydrogen atom loss, attributed primarily to H + *o*-C_6H_4 (*ortho*-benzyne). The observed translational energy distribution was consistent with statistical decay on the ground state surface. At 193 nm, dissociation to H + C_6H_4 and C_4H_3 + C_2H_2 was observed. The C_6H_4 fragment can be either *o*-C_6H_4 or *l*-C_6H_4 resulting from opening of the phenyl ring. The C_4H_3 + C_2H_2 products dominate over the two H loss channels. Attempts to reproduce the observed branching ratio by assuming ground state dynamics were unsuccessful. This discord, between the experimentally observed branching ratio and the theoretically predicted branching ratio led us to reinvestigate the dissociation dynamics of the phenyl radical at 193 nm, while producing the radical under different source conditions.

The photodissociation dynamics of the *tert*-butyl radical (*t*-C_4H_9) were investigated at 248 nm. Two distinct channels of approximately equal importance were identified: dissociation to H + 2-methylpropene (C_4H_8), and CH_3 + dimethylcarbene (C_3H_6). Neither the translational energy distributions that describe these two channels nor the product branching ratio are consistent with statistical dissociation on the ground state, and instead favor a mechanism taking place on excited state surfaces. The studies presented in this dissertation show that although hydrogen atom loss is sometimes expected to be the only major dissociation pathway in the photodissociation of hydrocarbon radicals this is not always a justified assumption.

To my mother and father

Mariana and Dorel

and my bride-to-be

Christine

Contents

Acknowledgments

My deep gratitude goes out to my family and friends. It would not have been possible to write this dissertation without their support. I would like to thank Professor Dan Neumark for accepting me in his group and for his mentorship throughout the years. I could always count on his support, and I will always be grateful for it. His dedication to science and research is truly inspiring; I have never met a scientist as forceful and driven as Dan. His ideas and insights were essential for the advances accomplished on the x-beam project.

I would like to thank Scott Goncher for teaching me about life and for teaching me how to swing. I know I am a better person because of Scott and I hope he knows that. He also introduced me to Machine B. I would like to thank Amy Brunsvold fourteen times for being super-cool and a true friend, and for wearing a dress backwards that one day. I will never forget it. I am grateful Dayoung Park decided to join x-beam as an undergrad. She was unfazed by any sort of emergency in the lab, which I always found calming in times of stress. I would like to thank Gabriel Just for having my back in the pain cave for more than a year; with a no problemo attitude. I am grateful that Neil Cole-Filipiak joined the x-beam project and taught me as much about dissociation as I taught him. Young as he is, Neil showed great knowledge about the ways of the world, internets, and drink. Deep conversations and dart games with Neil filled me with mansuetude to the brim and kept me sane long enough to sort of complete the dissertation that follows. I am also excited to see that Mark Shapero joined the project and has undertaken the daunting task of updating the B Machine.

I am indebted to the Neumark group for their support and acceptance. I always felt as part of a family and I always will. I enjoyed working alongside our group members more than I can express on paper and I hope that I will meet them again along the way. I cannot name them without saying what they meant to me and there is no more time, since today is the last day of this last semester, so I will not attempt it. I have a bit of a katzenjammer because of them right now and I just know it wouldn't sound as éclat as it should. I wish I would have, though, and I hope they know this apopemptic note is for them.

I am also very grateful to the Williams group and the Leone group for making me feel welcome. I have been fortunate to collaborate with Professor Evan Williams and Alex Donald and I would like to thank them for making it possible for us to work together. I also had the pleasure of getting to know Professor Steve Leone, and the fortune of learning from him what it means to be a good manager and careful scientist. I would like to thank Professors Rich Saykally, Ron Cohen, and Robert Dibble for being on my committee and for helping me along the way. I would also like to take this opportunity to thank Professor Ben McCall for getting me started in research and for giving me the first real taste of physical chemistry. I would like to acknowledge Professor Robert Dibble for giving one of the best seminars I had the pleasure of attending at the University of California. In this seminar he spoke of flames, but he also regaled a story from his past, his high school years. As the president of the three member chemistry club, he invited Professor Seaborg from the University of California to visit and give a seminar. I will never forget this story because Professor Seaborg did visit and gave a seminar.

Most of all, I would like to show my gratitude to Christine, for standing by my side and sharing the ups and downs of graduate school. Her love, support, and encouragement made graduate school possible. It all started with the third quantum problem set and I hope it never ends. She became my fiancée in Berkeley and she will be my bride within a month. I don't know what the future holds; I don't even know where we will be two months from now, but I am happy that she will be with me and that we will find out together.

Chapter 1

Introduction

The experiments discussed in this dissertation aim to understand the photodissociation dynamics of neutral free radicals. This chapter will introduce the field of chemical dynamics and unimolecular reactions as well as neutral free radicals and the role they play in chemistry. Studies concerned with the production and photodissociation of the phenyl and *tert*-butyl radicals will be presented later in this dissertation, but the fundamental principles and the analytical tools necessary to investigate photodissociation dynamics are discussed in this chapter and the next.

1.1 Photochemistry of Unimolecular Reactions

One of the principal goals of chemistry as a field of study is to understand chemical reactions. An intuitive way of investigating chemical reactions is by intersecting two molecular beams containing reactants and detecting the scattered products. Experiments of this sort are interested in the identity of the products, their energy states, and the mechanism of the reaction process, but are limited because they are forced to average over a whole range of reactant impact parameters. One solution to this problem is to study half reactions; the dissociation of a molecule into fragments, also named half collisions. These processes are unimolecular reactions since a single isolated reactant molecule undergoes a chemical change, and they can probe a wide variety of chemical systems and processes.

The unimolecular reaction can be initiated by adding sufficient energy to molecules, equal to or larger than the activation energy. There are multiple ways of depositing energy in a chemical system. One of the simplest ways of adding energy to molecules involves thermal heating in which gas phase molecules are energized by collisions with the bath gas or the walls of a chamber. An alternative was found in chemical activation where high energy species are added to molecules to form activated molecules. The drawback of these techniques is that they result in an uncertain energy content of the molecule of interest or in uncertain collisional deactivation rates.[1] Direct

photodissociation of molecules in collisionless environments has permitted excitation to well-defined energy levels that are spectroscopically selected and that are not susceptible to collisional deactivation.

Photodissociation experiments are a major component of photochemistry, which is the study of chemical reactions that involve light as a reactant or product. Photodissociation studies use photons as the energy source to overcome the activation energy for a chemical process and can be performed in a collisionless environment, thus eliminating many unknowns from the system. Photodissociation connects molecular spectroscopy and molecular scattering since it starts with the absorption of light and ends with the scattering of photofragments, and thus represents instances in which molecules break apart due to light absorption. While the use of lasers is a great way of exciting molecules above their dissociation threshold, the dissociation process is still dependent on the shape of the potential energy surface of that system. The study of unimolecular reactions is ultimately a study of potential energy surfaces.

The potential energy surface (PES) is one of the most useful models that help us understand and visualize chemical reactions. The potential energy surface is a multidimensional construct that represents all possible configurations of a system's electrons and nuclei. The surface can be constructed by calculating the electronic energies of different nuclear configurations and piecing them together along the independent coordinates of that system. This process can be carried out by invoking the Born-Oppenheimer approximation and assuming that the motion of nuclei is infinitely slower than that of electrons. Every chemical system has multiple potential energy surfaces, or states, superimposed on the same coordinates; surfaces that are identified by their spin angular momentum and orbital symmetry.[1] The ground electronic state is the lowest potential curve.

The shape of the potential energy surface is different for different types of unimolecular reactions, depending on whether they represent dissociation, isomerization, or elimination events.[2] The shape of the potential energy surface will also determine the disposal of energy among the photoproduct degrees of freedom. For these reasons, identification of photoproducts and their energy content can help visualize the shape of the potential energy surface and elucidate the reaction mechanism.

Dissociation can take place on an excited state surface or on the ground state surface. The excited state surface can be dissociative along a reaction path, so if such an excited state is initially populated the reaction path follows immediate dissociation. The initially excited state, however, can also be a bound state that is coupled to a dissociative state. If a molecule is excited to such a bound state and subsequently undergoes dissociation after passing to the dissociative state it is classified as electronic predissociation. This is termed as predissociation since the molecule spends time in the originally excited state.

Even in cases in which an excited state surface is accessed upon photon absorption, dissociation might not be an excited state process if the molecule undergoes nonradiative decay to the ground electronic state. Radiationless transitions of this sort, where no

photons are emitted, can be either intersystem crossing or internal conversion depending on whether the molecular spin state changes or not during the transition. In either case, the energy of the absorbed photon is converted into vibrational energy. The shape of the ground state potential energy surface can differ along the reaction path from system to system. Most generally, it can be a barrierless process or it can contain an exit barrier along the reaction path.[1,2] The correlation between the shapes of potential energy curves mentioned above and the experimentally observed energy of the photoproducts will be discussed in the next sections together with different experimental methods that can be used to address photodissociation dynamics.

1.2 Photofragment Translational Spectroscopy

Two important features of the photodissociation process are that total energy is conserved, and that the available energy of the photoproducts, E_{avl}, is partitioned between internal and external degrees of freedom. The external energy is composed of translational energy, while internal energy can be vibrational, rotational, and electronic. With this in mind, we can write an expression for the available energy of the photoproducts:

$$E_{avl} = h\nu - D_0 - E_{int} = E_T + E_{int(products)} \quad (1.1)$$

In this equation $h\nu$ is the energy of the absorbed photon, D_0 is the bond dissociation energy of the photolysed bond, and E_{int} is the internal energy of the photodissociated species before photon absorption. The potential energy surface of the system can be probed by experimentally measuring the translational (E_T) or the internal energy of the photofragments ($E_{int(products)}$). If dissociation takes place on an excited state surface that is dissociative the available energy is mainly channeled into translation rather than into internal degrees of freedom. If the potential energy surface is bound, however, the energy distributions are different depending on the presence or absence of an exit barrier. In both cases, the bound surface can trap the molecule allowing for a more statistical vibrational energy redistribution before dissociation. For a barrierless process, the available energy is thus mostly channeled into internal energy where the vibrational modes of the products are populated. If dissociation takes place over a barrier, however, the energy required to overcome that barrier is preferentially deposited as translational energy of the products.

It is important to note that the translational and internal energy of the photoproducts are complementary. It is sufficient to measure one of the two values to infer something about the other. Equation 1.1 can be used to define two major categories of experimental techniques that are used to investigate unimolecular photodissociation events; techniques that probe the internal energy of the photoproducts and techniques that probe the translational energy. These techniques can provide complementary information about the dissociation process, so oftentimes multiple techniques are used to elucidate a dissociation mechanism. This field of research is named photofragment spectroscopy and

it was developed conceptually by Zare and Herschbach[3,4] and pioneered experimentally by Kent Wilson.[5,6,7,8] These experimental and theoretical investigations inspired a gamut of experimental techniques focusing on photofragment detection. One technique uses laser induced fluorescence to study photodissociation dynamics by probing the internal energy of the photofragments. This method is sensitive, but also very selective since it can only be used to detect state selected fragments that have known fluorescence. Many photodissociation techniques focus on probing the translational energy distributions of specific photofragments such as high-*n* Rydberg hydrogen atom tagging and hydrogen atom Doppler spectroscopy as well as resonantly enhanced multi-photon ionization of specific photofragments. These techniques perform photofragment translational spectroscopy, together with the technique used for the work presented in this dissertation.

Photofragment translational spectroscopy coupled to a universal detection scheme is complementary to the more selective techniques described above. It uses a universal detection scheme that can be used to investigate the translational energy of any photofragment of interest, regardless of its chemical character. The goals of a photofragment translational spectroscopy experiment are to obtain information about the identities and the translational energy distributions of the photofragments, the anisotropy and the reaction mechanism of the dissociation process, and the relative importance of each dissociation pathway. This is a very powerful method that can achieve these goals and was successfully applied to previous studies of a wide range of molecular systems, including the work presented in this dissertation.

1.3 Neutral Free Radicals

Photofragment translational spectroscopy is a powerful experimental technique that has been used to study a wide range of chemical systems. It is adept at investigating the photodissociation dynamics of neutral free radicals since it can do so in a collisionless environment. Neutral free radicals are important intermediates in combustion, atmospheric, and interstellar chemistries. Despite their importance, experimental studies are limited due to their high reactivity and transient nature. Neutral free radicals are open shell species that posses one or more unpaired electrons and thus have non-zero spin. Although radicals are very reactive, they are physically stable, meaning that they have a bound ground state surface. They will, however, quickly react with anything they encounter so it is difficult to produce samples with high concentrations and high purity. This is a big experimental challenge that is not easily overcome, a challenge that will be addressed throughout this dissertation. Radicals are present in many different chemical environments, and although they are typically short-lived, they are very important since they are the intermediate species that ultimately dictate the chemistry of the system. For example, long-lived radicals can be found in the diffuse interstellar medium where ambient pressures are very low, while short-lived radicals are found in flames.

Neutral free radicals are inherently different from other molecules, such as closed-shell species, and their dissociation dynamics are expectedly different. Many times, direct

dissociation of a closed shell species results in the formation of two radicals. This is usually a barrierless process since there is no expected barrier for the association reaction of two radicals. For example, the hydrogen molecule is a closed-shell species containing a single bond, H_2, but if the bond is stretched and broken two hydrogen atoms, or radicals, are obtained. This idea can be turned around to show that two radicals reacting together will usually form a closed shell species that is less reactive than the radicals forming it. This is the exact reason why radicals are considered to be chemical intermediates; they are not usually present as a reactant or as a final product of a chemical process. Direct dissociation of a radical, however, usually results in the formation of a closed-shell and open-shell species. An exit barrier is thus expected for this process, since in the reverse reaction the radical reacts with a stable molecule. Most radicals are high energy species that have multiple low lying electronic states that can be accessed with a single ultraviolet photon. This makes their photochemistry complex and a great model to investigate couplings and interactions between excited states on the way to bond dissociation.[9]

1.5 Systems Discussed

The principal theme of this dissertation is the study of the dissociation dynamics of neutral free radicals. The unifying experimental theme that will be encountered throughout this dissertation is concerned with the formation of neutral free radicals in a collisionless environment so that they may be studied. The first radical that will be presented is the *tert*-butyl radical, formed from the pyrolysis of azo-*tert*-butane. The ultraviolet photodissociation dynamics of this radical at 248 nm are shown to proceed along multiple dissociation pathways corresponding to hydrogen atom loss and methyl radical loss. The translational energy distributions used to fit the collected TOF spectra did not coincide with the distributions expected for a statistical process while the measured branching ratio between the two pathways did not coincide with dissociation on the ground state surface. Besides the insights that this work provides on the dissociation dynamics of the *tert*-butyl radical, formation of this tertiary radical proved to be a very good test for the radical source used in this study. The photodissociation dynamics of isobutene, although it is a closed-shell molecule, are also presented since they help clarify some of the data obtained from photodissociation of pyrolysed beams containing the azo-*tert*-butane precursor.

The second radical investigated in this dissertation is the phenyl radical and its dissociation dynamics at 248 and 193 nm. Photodissociation at 248 nm showed one major dissociation channel consisting of hydrogen atom loss. Photodissociation at 193 nm, however, showed the presence of an acetylene loss channel, a dissociation pathway that can only take place after ring-opening of the phenyl radical. The striking result in this study was the measurement of the branching ratio in which hydrogen atom loss was concluded to be the minor channel. Efforts to understand and justify this observation resulted in a second investigation of the dissociation dynamics of the phenyl radical at 193 nm, a study that used different methods for radical formation.

The last system discussed focuses on the dissociation dynamics of the ethoxy radical. Although the potential energy surface for this system is quite complex, the only photodissociation channel identified in this study was methyl radical loss. This study is not complete since formation and photodissociation of the hydroxyethyl radical, an isomer of the ethoxy radical, was not realized. This study leaves a lot of open questions that will hopefully inspire future studies investigating photodissociation dynamics via photofragment translational spectroscopy.

Chapter 2

Experiment

The work presented in this dissertation was performed on an apparatus with a fixed source and rotatable detector. This is a versatile machine that can be easily reconfigured for different experimental investigations. Although the dissociation dynamics presented in this dissertation were performed using photofragment translational spectroscopy the machine can be used for performing molecular scattering and even surface scattering experiments. The greatest variety of choices, however, is in source designs for neutral free radical production. This chapter will describe the machine as well as some of the work that has been performed on it throughout the years.

2.1 The B Machine

2.1.1 The History of the B Machine

The B Machine is the experimental apparatus used to perform the work described in this dissertation. The B Machine was built more than 40 years ago at the University of Chicago by the Lee group following the design published in 1969 by Yuan T. Lee.[10] This was the second machine built by the Lee group, thus receiving the name of Machine B; a name still in use today. B Machine was built in the mid 70's at University of Chicago, and transported to Lawrence Berkeley National Laboratory when Yuan T. Lee accepted a professorship at the University of California, Berkeley. In 1986, around the time that Yuan T. Lee and Dudley Herschbach received the Nobel Prize in Chemistry, the machine was moved to the C level of Giauque Hall on the University of California campus. The laboratory in Giauque Hall was very nicely built, with a spacious pump room located directly below the floor, so that the large pumping power necessary for the B Machine could be provided efficiently. The B Machine resided there for about a decade until Professor Lee became the President of Academia Sinica in Taiwan and ownership of the

machine was transferred to his former graduate student, Daniel M. Neumark. Due to seismic retrofitting of the chemistry department, B Machine was relocated to the D level of Latimer Hall by Jason C. Robinson, where it can still be found today. The machine was first taken to the Lawrence Berkeley National Laboratory for high vacuum cleaning and then placed in a newly designed space in D 10 Latimer Hall.

The space in D 10 Latimer Hall was carefully designed[11] so that it maintains the versatility of the B Machine, making it possible to reconfigure the machine for different kinds of experiments. Throughout its lifetime, the B Machine has been used for a variety of collision dynamics[12,13,14] and photodissociation dynamics.[15,16,17] The bulk of photodissociation investigations focused on closed-shell species ranging from haloalkanes[18,19,20,21] to acetone[22] and alkenes.[23,24] The scientific impact of the B Machine has been tremendous and so far ongoing. Scott J. Goncher looked at the photodissociation dynamics of propargyl radicals,[25] and in so doing started a new scientific direction for the studies performed on Machine B. Production and isolation of beams containing free radicals is much more complex and challenging than the formation of beams composed of stable molecules, while their dissociations dynamics are just as important. This new direction provides a wealth of chemical systems that the B Machine is perfectly suited for; some of which are presented in this dissertation. The B Machine is still evolving, and the next few chapters will show the ongoing research performed on this apparatus, and hint at some of the future directions that are to come.

2.1.2 The Experimental Design of the B Machine

The B Machine is the experimental apparatus used to perform the work described in this dissertation. The B Machine is an impressive, steel box with a daunting amount of cables and pipes connected to it. This stainless steel box is the main scattering chamber and it has a volume about 0.7 cubic meters. The main chamber must be this large so it can properly house the detector chamber within it, a chamber that must be free to rotate for a minimum of 100°. The top wall of this chamber is 6.4 cm thick to support the weight of the detector, while the sides and base are 3.7 cm thick to prevent atmospheric pressure from crushing the chamber.

A smaller, cylindrical chamber connected to the main scattering chamber is the source chamber. The source chamber houses the piezoelectrically activated valve[26] used for production of the pulsed molecular beam. To form the molecular beam, helium or argon gas is flown over the sample of interest and expanded into the vacuum of the source chamber through a small opening about 500 micrometers in diameter. The pulsed valve is positioned 0.7 to 1.4 cm way from two skimmers that separate the source chamber from the main chamber. These skimmers collimate the molecular beam and provide differential pumping between the two chambers, making it possible for the main chamber to reach pressures two orders of magnitude lower than the source chamber and as low as $4 \cdot 10^{-7}$ Torr. The chambers of the B machine are so large that it is necessary to use two 2000 liters/second turbomolecular pumps. The turbomolecular pump connected to the source chamber has chromium plated blades to prevent corrosion caused by the chemicals

used in experiments and is connected to a Welch duo seal roughing pump as well as an Edwards roots blower to better cope with the high pressures of the source chamber.

Inside the main chamber, the molecular beam is crossed at 90° by the photodissociation laser. If the laser beam is replaced with a molecular beam reactive scattering experiments can be investigated. The interaction region between the molecular beam and laser beam is partly surrounded by a closed-cycle liquid helium cold head. Molecules that collide with the cold head and have a higher boiling point than 10 degrees Kelvin will condense. The cold head is built in such a way, so that when the detector is open during an experiment it is facing the cold head. This is one of many built in devices intended for background noise reduction caused by residual gas in the machine. The photofragments created in the photodissociation event enter a triply differentially pumped detector that can rotate in the plane defined by the molecular and laser beams.

The detector is anchored on a rotatable 63.5 cm wide flange that rests on top of the B machine. The seal between the flange and the chamber is created by gravity pushing together two Teflon rings. The detector can rotate more than 90° away from the molecular beam so that in case two molecular beams are used the detector can characterize both beams. The detector of the B Machine is an amazing feat of engineering. The part of this detector that is outside the walls of the B Machine is composed of four turbomolecular pumps and a liquid nitrogen cylinder used for

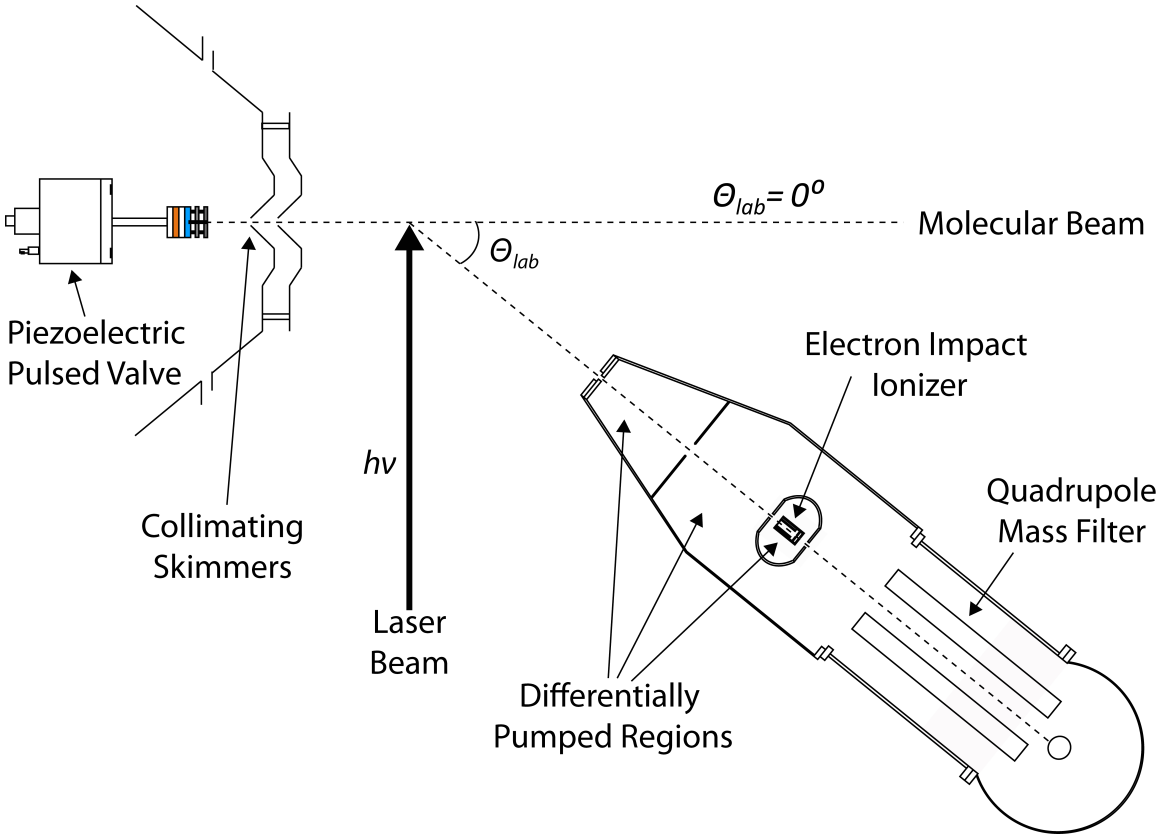

Fig. 2.1 Schematic of apparatus, showing the radical source, photodissociation laser, and rotating mass spectrometer detector.

cryogenic cooling of the detector. Three of the turbomolecular pumps are used to evacuate separate regions of the detector while the fourth is the foreline pump used to back the other three pumps. The part of the detector chamber enclosed within the walls of the B Machine is shown in Figure 2.1 and is composed of three differentially pumped regions. The first region is the entrance to the detector where a pressure lower than $1 \cdot 10^{-10}$ Torr is obtained. The second region houses the detector as well as the third region. The third region is separated from the second region by a liquid nitrogen cooled jacket and it houses the electron impact ionizer used in this detection scheme. The pressure in region two is below $1 \cdot 10^{-12}$ Torr while the pressure in region three is slightly higher because of the ionizer it houses, but still settles below $2 \cdot 10^{-11}$ Torr. These pressures are some of the lowest pressures attainable in laboratory and are comparable to pressures found in outer space. The pumps evacuating the detector are connected to the emergency generator from Hildebrand Hall so that power interruptions will not take place. This detector has been evacuated and thus not exposed to air for more than five calendar years.

The detector can be sealed from the scattering chamber with a slide-valve. If the slide valve is open molecules enter the detector, pass through region one and part of region two before entering region three. In region three the molecules collide with high energy electrons produced by a Brink-type electron impact ionizer.[27] This ionizer uses a thoriated iridium filament that can easily produce 4.0 mA emission currents. After ionization, the cations are guided out of region three by ion optics and into a 19 mm long quadrupole mass filter. A direct current voltage overlapped with a radio-frequency voltage is applied to the electrodes of the quadrupole to select the desired mass to charge ratio. The mass selected ions are accelerated towards a "doorknob" held at -30000 volts. Six to seven secondary electrons are emitted for each ion collision, electrons that are accelerated away from the high voltage surface from which they were released. The accelerated electrons collide with an organic phosphor-based scintillator film which on average produces 4 photons for each electron impact. The emitted photons are collected by a photomultiplier tube and are thus converted to an electric current. The output of the photomultiplier tube is processed by a discriminator connected to a level adapter that removes dark counts generated inside the photomultiplier tube.

Finally, the signal is binned with a multichannel scaler, thus giving time information from the photodissociation event. As such, the spectra collected with this detector are time-of-flight (TOF) spectra that show the time necessary for the photoproducts to travel from the interaction region to detection. This is the principle idea behind this experimental design and the reason why it can be used to perform photofragment translational spectroscopy. The velocity of the fragments can be determined by measuring the time-of-flight over the known distance between photodissociation and detection. Once the velocity is known, the kinetic energy, E_T, of mass selected fragments can be determined. Electron impact ionization coupled to the geometry described in this

section gives this detector the capability to measure the translational energy and angular distribution of any chemical species formed in a photodissociation event.

2.1.3 Translational Spectroscopy with Machine B

The B Machine was built to detect the translational energy of any fragments that originate at the interaction region and enter the detector. Electron impact ionization uses high energy electrons that can ionize any gas phase species, making this a truly universal technique. High electron energies must be used so that the probability of ionization becomes as close to unity as possible. Electron impact ionization, however, has a significant downside that complicates the spectra obtained. Upon collision with a high energy electron a large amount of energy is transferred, more than the necessary amount for ionization. This excess energy can break the fragment apart into multiple "daughter" ions that contain the same translational energy information but are detected at smaller mass to charge ratios. This effect is termed dissociative ionization and it has been well documented for most stable chemical species.[28] Dissociative ionization must be taken into account while determining the branching ratio between different pathways, but also facilitates measurement of the branching ratio since two different photoproducts resulting from two different dissociation pathways can sometimes dissociatively ionize to the same mass to charge ratio, and thus be detected simultaneously.

The B Machine was built so that it could mitigate some of the complications resulting from dissociative ionization; mostly by the use of a rotatable detector. To understand this, we must consider the use of supersonic expansions for formation of molecular beams. Supersonic expansions can produce internally cold reactant molecules which simplifies the collected photodissociation signal. If the reactants are assumed to be produced with no internal energy whatsoever Equation 1.1 can be simplified further

$$E_{T(products)} = h\nu - D_0 - E_{int(products)} \tag{2.1}$$

The maximum translational energy possible can be determined if the fragments are assumed to be produced internally cold, $E_{int(products)} = 0$. In the reactant molecule center of mass frame photofragments have the same momentum if they originate from the same dissociation event, meaning that they are momentum matched partners. Their translational energy distribution can be written as:

$$E_{T(products)} = \frac{1}{2}\mu_{rel}\left|\vec{V}_{rel}\right|^2 \tag{2.2}$$

Where μ_{rel} is the reduced mass of the fragments and $\vec{V}_{rel}$ is the relative velocity of the dissociating fragments. With this in mind, we can calculate the maximum velocity of the photoproducts in the center-of-mass frame. The reactant molecule, however, has a supersonic velocity in the lab frame, so if this velocity is known, the maximum laboratory scattering angle where particular photoproducts scatter can be determined. This is a

Newton diagram,[29] and it can be used to deconvolute the TOF spectra that contain multiple contributions caused by dissociative ionization in the detector.

The Newton diagram shows the maximum laboratory angle away from the molecular beam where certain photofragments can be scattered, so it would make sense for the experimental setup of the B Machine to incorporate a rotatable detector that can move away from the molecular beam. This experimental feature allows the detector to move past the maximum scattering angle of certain fragments and thus partly mitigate the complexity produced by dissociative ionization.

The rotatable detector of the B Machine was built to measure time-of-flight spectra and to determine the translational energy of photoproducts. Energy distributions are obtained from forward convolutions of trial distributions that are pointwise adjusted to fit the acquired TOF spectra. This fitting routine and the assumptions made have been described in detail previously, and will not be presented here except for the functional form that is used to correlate between the experimentally observed TOF spectra and the product energy distributions used to fit them.

$$N_P(T,\omega_D) = C_n^0 \frac{L^3}{T^4} \frac{m_R m_P}{(m_R - m_P)} \int_{\frac{L}{T},\omega_D} \frac{P_n(E_T,\Omega_n)}{u_P} N_R^0(v_R,\omega_R) dv_R d\omega_R d\omega_P \qquad (2.3)$$

In this equation, $N_P^0(T,\omega_D)$ is the number density of photoproduct P that enters the solid angle of the detector, ω_D, after traveling a flight length L as a function of time T. $N_R^0(v_R,\omega_R)$ is the initial density of reactant molecules, while C_n^0 is a constant. The $P_n(E_T,\Omega_n)$ is the center-of-mass translational energy distribution and is the final goal of a dissociation study. It is assumed that the translational energy distribution can be uncoupled from the angular distribution and can be treated separately:

$$P_n(E_T,\theta) = P_n(E_T) I(\theta) \qquad (2.4)$$

The uncoupled angular distribution $I(\theta)$can be fit with Equation 2.5 in which P_2 is the second order Legendre polynomial.[30]

$$I(\theta) = \frac{1}{4\pi}(1 + \beta P_2 \cos\theta) \qquad (2.5)$$

where Θ is the angle of the scattered velocity vector with respect to the electric field of the photon and the value of the β parameter can vary from -1 to 2 and describes whether the transition is parallel, isotropic, or perpendicular. For an isotropic process, β takes a value of zero. The uncoupled $P(E_T)$ distribution is treated iteratively. Although analytical expressions have been published,[31,32] it is not always possible to use only one analytical expression for $P_n(E_T)$ since it strongly depends on the properties of individual systems. A numerical fit using trial $P_n(E_T)$ are commonly employed, where the trial distributions can be altered pointwise.

2.2 Data Collection and Analysis

2.2.1 Molecular Beam Characterization

The first step in performing a photodissociation experiment is to characterize the molecular beam. If the lab frame velocity of the reactant molecules is not known the Newton diagram cannot be drawn and the translational energy distributions of the photoproducts cannot be determined. Characterization of the molecular beam implies an understanding of the flow velocity, the average velocity of molecules in each pulse, as well as the speed ratio of the beam, the spread in velocities. These parameters can be calculated with the use of a slotted chopper disk located in the main chamber between the skimmers and the laser interaction region. This chopper wheel is mounted on a translational stage so that it can be inserted and retracted from the beam path when necessary. The slotted chopper wheel is spun at a frequency of 200 Hz, the same frequency used for the pulsed valve. This means that every single molecular pulse produced by the pulsed valve is chopped and can be used for beam characterization.

If the chopper wheel is spinning at the correct repetition rate the pulsed valve can be triggered off of the chopper. The pulsed valve is triggered in such a way so that the bulk of molecules in the molecular pulse can make it through one chopper slit and onto the detector. The multichannel scalar is also triggered off of the chopper with time zero coinciding with the passage of molecules through the chopper slit. With the detector placed on beam at a lab angle of 0° a TOF spectrum for the desired mass to charge ratio can be collected. This spectrum can be fit with the KEL[11] fitting program to the following functional form:

$$N(v) \propto v^2 e^{-s^2\left(\frac{v-V_0}{V_0}\right)^2} \tag{2.6}$$

where V_0 represents the beam velocity and s the speed ratio. Since the size of the chopper slit can affect the shape of the observed spectrum the chopper function and the detector acceptance function are taken into account so that the correct beam parameters can be derived.

2.2.2 Calibration of the B Machine

The machine parameters must be measured and implemented correctly so that the collected spectra can be used to produce reliable energy distributions. For example, the velocity of the photofragments can only be determined because the distance from

dissociation to detection is known, a distance that must be remeasured if the experimental setup is modified. Starting at the beginning, we must consider the true flight time in terms of the measured flight time. The measured time, $t_{measured}$, can be expressed with the following equation:

$$t_{measured} = t - \alpha_{ion}\sqrt{m} + E_0 \pm M_0 \quad (2.7)$$

In this equation, α_{ion} is the ion flight constant, E_0 is the electronic offset, M_0 is the mechanical offset, m is the mass to charge ratio of the detected cation, and t is the actual flight time. This section will explain these parameters as well as the correct procedure for measuring them.

The measured time-of-flight is obtained directly from the collected TOF spectra. The mechanical offset, M_0, is caused by uncertainty in the location of the photodiode that is used for determining the exact location of the chopper slit. The rough location of the photodiode is known and the exact location can be determined very easily. Depending on the direction of rotation of the chopper wheel the time difference between the alignment of the slit with the photodiode and the molecular beam changes.[33] The mechanical offset is calculated by measuring the beam velocity with the chopper wheel spinning clockwise and counterclockwise and dividing the difference between the measurements by two. The current mechanical offset for the B Machine is of 5.5 μs.

The electronic offset, E_0, can be caused by the inherent rise time and non –zero width of electric pulses used in the triggering scheme. The offset due to the pulsed width produced by the photodiode is mitigated by the use of a time delay generator that can overlap the pulse with the multichannel scalar trigger pulse. Unfortunately, the photodiode pulse cannot be used to trigger the time delay generator, so a homebuilt box is used to transform this pulse into a square pulse, transistor-transistor logic (TTL) pulse, that can be used. The inherent rise time of this process can be measured with an oscilloscope by comparing the difference between the photodiode pulse and the TTL pulse. The current setup used on the B Machine has an offset of about 6 μs.

The final parameter that must be measured is the ion flight constant, α_{ion}. The measured flight time can be separated into two parts, flight of the neutral species, and the life-time of ions from creation to detection. The ion lifetime is equal to $\alpha_{ion}\sqrt{m}$ and thus varies depending on the mass of the detected cation. This constant can be measured by maintaining the neutral flight time constant and monitoring the arrival time of different ion masses produced in the ionizer. The electron impact ionization creates a multitude of daughter ions that have different detection times. A linear least squares fit of the plot between arrival time versus the square root of the ion mass to charge ratio will provide a slope, which is actually the ion flight constant. Usually, $CBrClF_2$ is the neutral molecule of choice, since it can undergo dissociative ionization to form a wide range of ions.

Now that Equation 2.7 is fully understood there is only one more parameter that must be determined. To be able to convert data from time space to velocity space the exact flight

length of the neutral species up to the point of maximum probability of ionization must be known. The only way to measure this distance accurately is to use a beam whose velocity is known. The velocity of continuous noble gas beams is equal to

$$v_{rare\ gas} = \sqrt{\frac{5k_BT}{m}} \tag{2.8}$$

where k_B is Boltzmann's constant, T is the temperature of the expanded gas, and m is the mass of the noble gas atoms. If multiple rare gas beams are used the peak positions can be fit to obtain the neutral flight length for the B Machine, 22.8 cm. This distance however is from the chopper wheel to the ionizer, and is the value used for characterizing molecular beams. The distance from the interaction region to detection is different since the molecular beam is crossed with the laser beam downstream of the chopper wheel. Several measurements using a scope or a calibrated translation stage show that this distance is equal to 2.00 ± 0.05 cm, making the distance from the interaction region to the ionizer equal to 20.8 cm. A lot of forethought went into the design of B Machine since the interaction region is located along the rotational axis of the flange supporting the detector. This must be the case since the distance between the photodissociation event and the detection of photofragments must not change with the lab frame angle of detection.

2.3 Radical Sources

Neutral free radicals are important intermediates in many chemical environments. Because of their high reactivity, radicals are found in complex environments that contain hundreds of species. The chemistry of many radicals is complicated by the presence of multiple excited states that can be accessed by the absorption of a single ultraviolet photon. This makes their photochemistry very interesting. Although very important, studies of neutral free radicals are not easily performed due to the challenges encountered in radical production. Moreover, radicals investigated by photofragment translational spectroscopy must be produced internally cold and in a collisionless environment. This section will outline the design of different sources that can be used for radical production. The discussion presented here, however, will be limited to source designs that can be used for the B Machine and thus be coupled to photofragment translational spectroscopy.

2.3.1 Photolytic Production

The Neumark group has a rich history of neutral free radical investigations. Free radicals typically have positive electron affinities, and this property can be used experimentally to generate pure beams of well characterized radicals. Radicals are produced from photodetachment of the corresponding anion with the use of a dye laser. The anions of interest can be mass-selected by time-of-flight from a mixture of ions formed by a pulsed

discharge source.[34,35,36,37] Unfortunately, this method cannot be coupled to the universal detector used on the B Machine, so different ways of forming neutral free radicals must be applied.

The simplest way to produce and study neutral free radicals with the B Machine is photodissociation. Photodissociation of closed-shell molecular system often results in the formation of two radicals. Depending on the choice of precursors, excitation wavelength, and ultimately the potential energy surface, the radicals produced in the primary dissociation process can be formed with sufficient internal energy to undergo a secondary dissociation.[38,39,40,41] Once the primary photodissociation is understood the secondary dissociation process can be fit. This is a nice technique that has been used to study the dissociation dynamics of many different radicals. Its use on the B Machine however is somewhat problematic because of the dissociative ionization taking place during detection. The TOF spectra obtained are often a conglomeration of peaks where the secondary dissociation signal is overshadowed by primary photodissociation.

The use of a second photodissociation laser, named photolysis laser for simplicity, can change the geometry of the experiment and overcome the complications caused by primary photofragments entering the detector. In this geometry, the photolysis laser is focused in the source chamber right in front of the pulsed valve nozzle output. This allows photolysis of the precursor molecules to take place before supersonic expansion is fully achieved. The laser pulse essentially depletes parent from the most intense part of the molecular pulse. The newly formed radicals are part of the beam and are thus collimated by the two skimmers on their way to the main scattering chamber. Inside the main chamber they are photodissociated as usual at 90°.

The packet of radicals formed in this fashion cannot be directly observed and characterized by placing the detector on-beam due to dissociative ionization of the overabundant parent at the same mass to charge ratio. Instead, the overlap of the photolysis laser with the molecular pulse in the main chamber can be visualized by monitoring the parent mass. At best overlap conditions, a depletion hole that accounts for as much as 10 to 20% of the total precursor molecules can be observed. The packet of newly formed radicals can then be visualized by monitoring the radical photodissociation signal at different delays between the source, composed of the pulsed valve and photolysis laser together, and the photodissociation laser. The photodissociation laser and pulsed valve are triggered at 200 Hz while the photolysis laser is triggered at only half that repletion rate. This allows for subtracting out any photodissociation signal that may be produced by precursor photodissociation.

Although the application of this design is somewhat limited, this setup was successfully implemented by Scott J. Goncher to study the photodissociation dynamics of propargyl radicals[25] and thus began a new focus for the studies investigated on B Machine. The choice of precursors and radicals that can be produced with this design are limited by several strict requirements that must be met. The precursor chosen must absorb very well at the photolysis wavelength and not absorb significantly at the dissociation wavelength. Ideally, the radical species would behave oppositely and absorb well at the

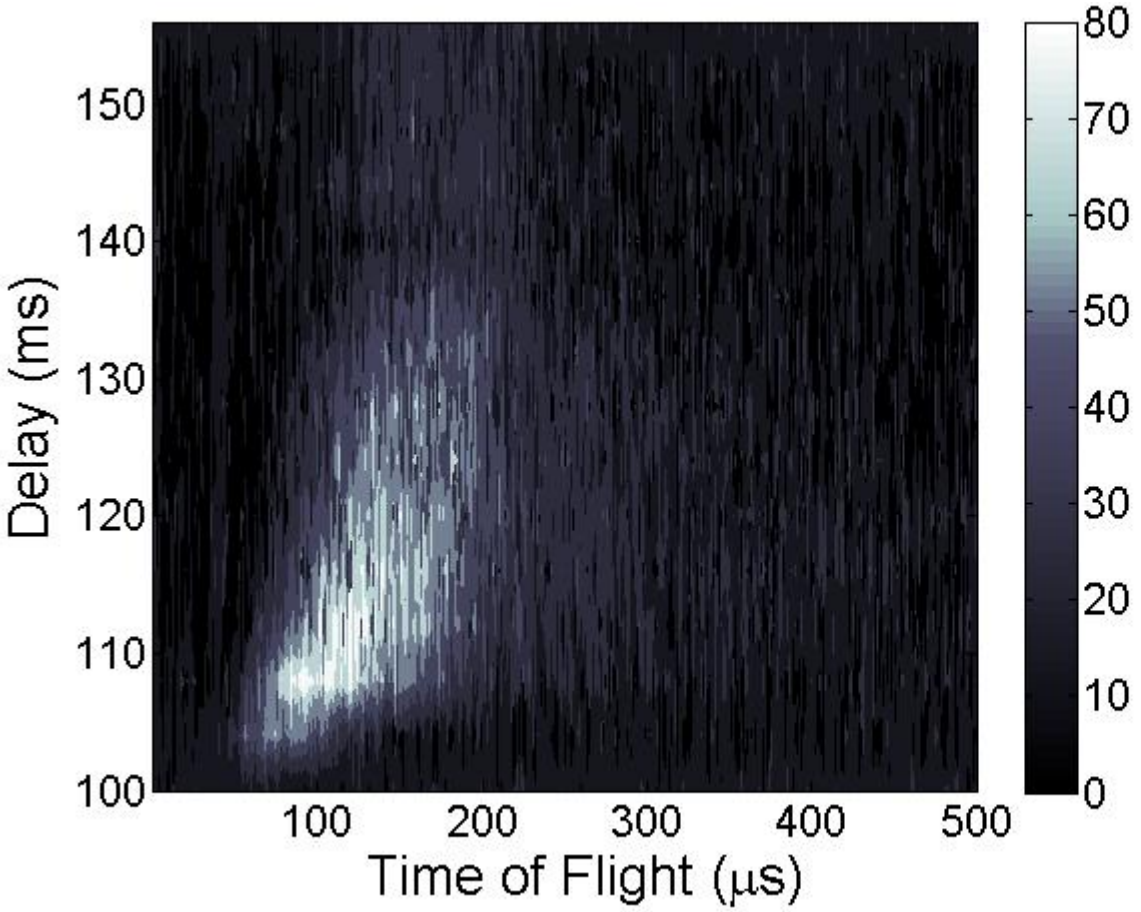

Fig. 2.2 Contour plot of *m/z* = 47 (CH_3S^+) time-of-flight signal with respect to the delay between the pulsed valve and the photolysis laser.

photodissociation wavelength. This limitation is problematic since excimer lasers are used for investigating photodissociation dynamics and the wavelengths that can be produced are limited to only a few, mainly 248 and 193 nm. The second limitation comes from the dissociation pathway through which the radicals are formed. Ideally, the radicals are produced by hydrogen atom loss or H_2 loss. It is necessary for the radical to be the heavy fragment so that it is not scattered from the beam. Production of the hydroxyethyl radical was attempted by photolysis of 2-iodoethanol entrained in a helium beam, and this was not successful although a depletion hole was observed. The heavy iodine atom was detected in the beam after photolysis, while most of the lighter radicals were scattered away from the beam and did not make it through the two collimating skimmers and into the main scattering chamber. For comparison, propargyl radicals were formed from hydrogen atom loss from allene, a precursor that absorbs at 193 nm and does not have significant absorption at 248 nm.[25]

The problems posed by the two-laser design described can be counteracted by yet another change to the geometry of the source design. If the pulsed valve is not collinear with the collimating skimmers, but rather points upwards at 90°, the precursor molecules cannot make it through the collimating skimmers and into the scattering chamber. If the

photolysis laser is placed right above the valve opening only photofragments will make it into the main chamber. The number of radicals formed this way and scattered towards the interaction region will be very small, but this geometry has the advantage of being truly background free. If the photodissociation dynamics of the parent are well understood, the origin of the observed signal is unambiguous.

This technique has been successfully used to produce a beam of CH_3S radicals from the photolysis of dimethyl disulfide (CH_3SSCH_3). Absorption of a 248 nm photon leads exclusively to S—S bond rupture forming two CH_3S radicals.[42] The contour plot in Figure 2.2 shows the TOF spectra of these radicals arriving at the detector as a function of photolysis laser—pulsed valve delay. At short delay times, below 100 ms, the molecular pulse does not have sufficient time to reach the photolysis interaction region. At longer and longer delays only the slower less intense part of the molecular pulse is photolysed. For a truly perpendicular source design the TOF of the radicals would not be expected to change significantly with respect to what portion of the molecular pulse is photolysed (basically depending on the time delay) since the detection axis is perpendicular to the initial velocity of the parent molecules. The spectra in Figure 2.2 is skewed to faster arrival times at shorter delays indicating that the angle between the molecular beam and the detection axis might be larger than 90° since the molecules in the front of the pulse are fastest in the lab frame. In actuality, the spectra shown in Figure 2.2 are expected to have the opposite dependence since slower reactants will produce faster photofragments in the plane perpendicular to the initial velocity vector. It is important to note that the geometry does not have to be perpendicular as long as it is not collinear, and that depending on the precursor used different angles can be favorable.

2.3.2 Production by Electric Discharge

High energy electrons can be used to produce a wide variety of chemical species. For this reason, all of the projects in the Neumark group have built discharge sources except for the cross-beam project. A quick survey of the research taking place in the Neumark

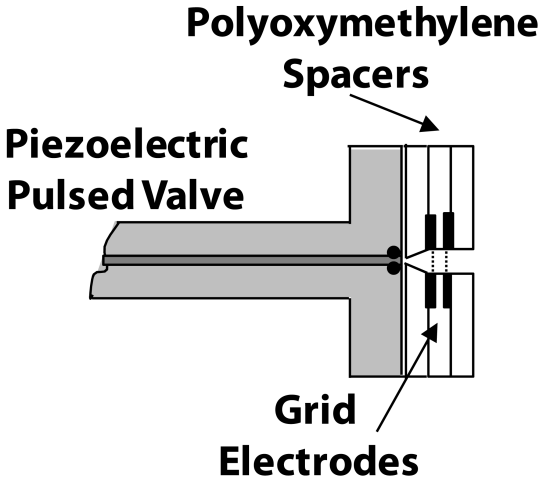

Fig. 2.3 Schematic of the direct current discharge source. Voltage was applied to the electrode closest to the pulsed valve body, while the outermost electrode was grounded.

group will quickly point to the B Machine as the standout. The other experiments use anionic precursor and have long flight tubes so that they can isolate mass-selected ion packets. The B Machine is not equipped to deal with ions in the same fashion, but since discharge sources have been shown to produce neutral free radicals[43,44] the grid discharge source shown in Figure 2.3 was built and installed. Moreover, the grid discharge source has been shown to produce colder anions than other ionization sources,[45] so it is possible that the neutral free radicals formed are internally colder.

This discharge source[46] consists of three polyoxymethylene spacers mounted to the pulsed valve. The spacers sandwich two ring electrodes that are covered with a mesh, so that the molecular beam can flow through them. The inner diameter of the ring electrode and spacers is about 2 mm. A direct current voltage between -800 and -1500 volts can be applied continuously to the electrode closest to the pulsed valve. Discharge does not take place in vacuum, but when molecules are present the source discharges. The discharge is stabilized by kΩ resistor that connects the high voltage power supply to the electrode.

Figure 2.4 shows the performance of the grid discharge source when used with a nitrosobenzene (C_6H_5NO) beam. It can be seen that at a high discharge voltage a very high percentage of the nitrosobenzene molecules present in the beam can be depleted, while the mass to charge ratio corresponding to the phenyl radical (C_6H_5) is still present. It was verified that this signal was not generated by anions in the beam with the introduction of a deflection plate before the entrance to the detector. Unfortunately, work in the Endo group on neutral free radical production has shown that discharge source geometry can have a big influence on the formation of some radicals; making it almost impossible to choose or discover an appropriate source design.

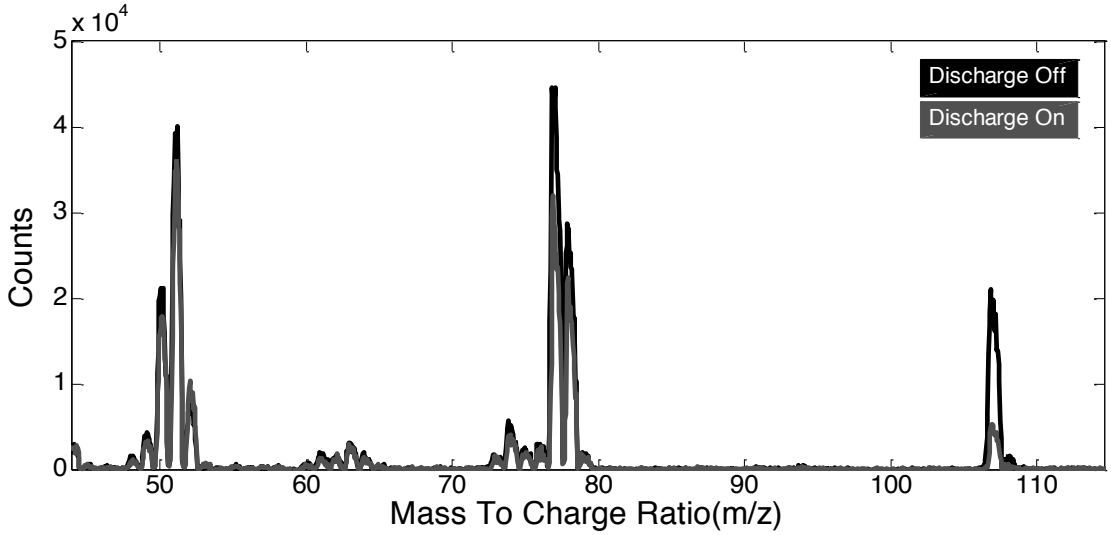

Fig. 2.4 Mass spectrum of nitrosobenzene molecules seeded in a helium beam taken with the discharge source off (in black) and at a voltage of -1.4 kV (in gray).

2.3.2 Pyrolytic Production

A flash pyrolysis source can also be used for producing neutral free radicals.[47,48,49,50,51] This source can create radicals by pyrolysis of carefully chosen precursor species with known energetics. This is a universal technique for radical production since the precursors used are stable, and chosen in such a way that they will undergo thermal unimolecular dissociation in a predictable way. Thermal unimolecular dissociation is a statistical process in which thermal energy is gradually deposited in all vibrational modes of the precursor molecule. This process can be modeled with RRKM theory,[52,53,54,55] according to which a system will start undergoing thermal unimolecular dissociation if the internal vibrational energy of the molecule is greater than the activation energy for the lowest lying dissociation pathway. If the precursor molecule is in thermal equilibrium with its surrounding environment at temperature T, each oscillator will have an energy of k_BT. This means that for a system with n normal modes dissociation will only start taking place when $nk_BT > E_0$, where E_0 is the activation energy for that process. The only variable in this equation is temperature, so if T is increased to very high temperatures

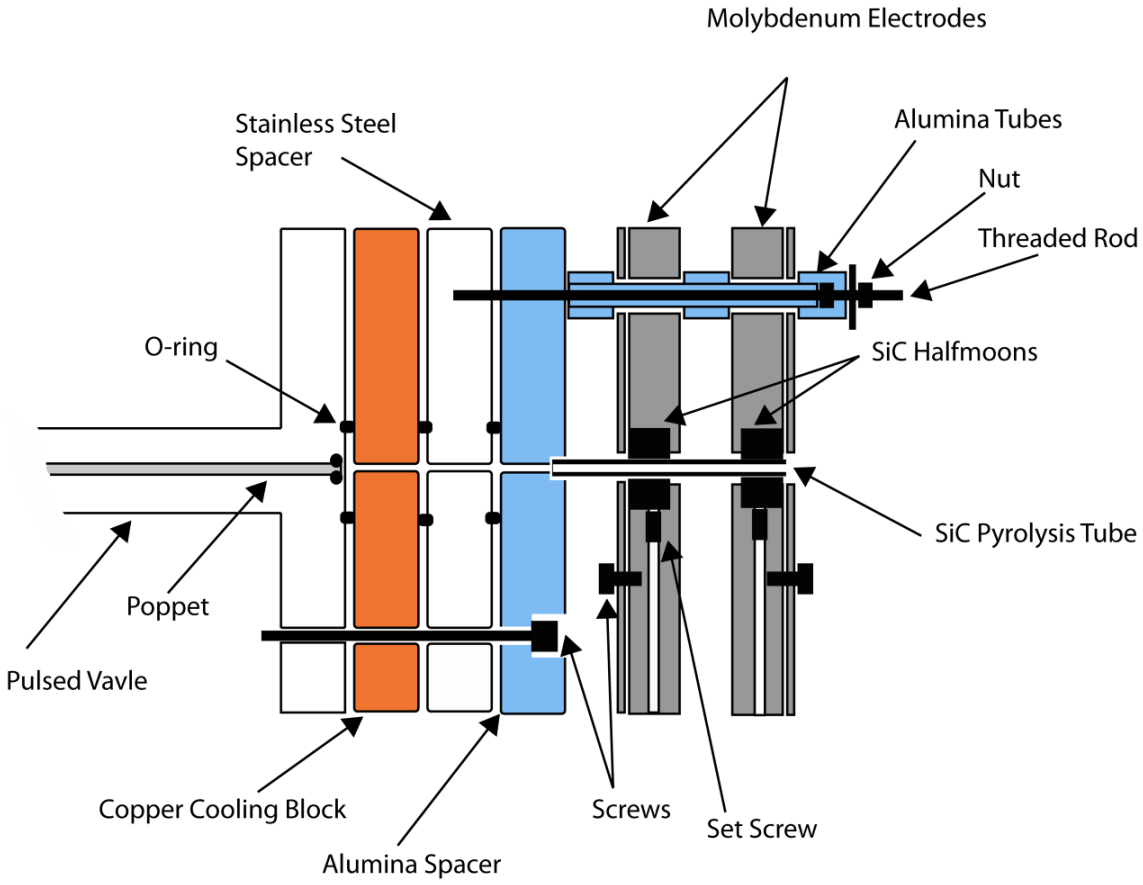

Fig 2.5 Cross section of the flash pyrolysis source, showing the Silicon Carbide pyrolysis tube, molybdenum electrodes, and the spacers necessary for connection to the pulsed valve. The source is three-fold symmetric along the molecular beam axis with respect to the screws that hold it together; meaning that there are two more threaded rods spaced 120° apart.

complete thermal dissociation of all of the precursor molecules in a molecular beam can take place. Supersonic expansion of the beam after it is heated to such high temperatures will internally cool the newly formed radicals and isolate them from other radicals in the beam.

The main part of the source is a silicon carbide, SiC, tube that is about a centimeter and a half long with an outer and inner diameter of 2 and 1 mm produced by Saint Gobain Incorporated. This tube is mounted to the pulsed valve with the help of two molybdenum electrodes that also provide the electrical connection necessary to heat the tube. These electrodes are then mounted to the pulsed valve with the help of a water-cooled copper cooling block and an electrically insulating alumina block as shown in Figure 2.5. The electrodes were made out of molybdenum since they can withstand high temperatures much better than steel, and since their thermal expansion coefficient is much closer to that of the SiC tube. Each electrode incorporates two SiC half-moons that are pressed around the SiC pyrolysis tube by a setscrew. The SiC tube is nested inside of the alumina piece to provide a better seal so that the molecular beam is forced to go through the pyrolysis tube.

The silicon carbide tube is resistively heated by a current limited direct current power supply. By controlling the current applied to the tube the temperature of the tube can be changed. This can be inspected visually since the tube begins to glow at high temperatures. Temperatures ranging from 500° to 2000° can be achieved with this design, and the source is sufficiently robust to operate for extended periods of time without distorting. For photofragment spectroscopy studies to be possible the source must be able to maintain a constant temperature for multiple hours and it must not become misaligned from the two skimmers that it is originally aligned to. Figure 2.6 shows the performance of the flash pyrolysis source on the allyl iodide precursor, C_3H_5I. The mass spectrum of allyl iodide shows a peak at m/z = 168, 127 and 41. If higher powers are applied to the pyrolysis tube the peak corresponding to the parent mass, 168, is fully depleted while the peak corresponding to the allyl radical mass, m/z = 41, is still detected. At higher and higher temperatures it can be seen that the I^+ signal at m/z = 127 becomes more and more intense. The appearance of a peak at m/z = 63.5 is indicative of iodine atom formation in the pyrolysis source since doubly ionized iodide cannot be observed from dissociative ionization of allyl iodide. I^{++} detection is a nice way of monitoring source performance when iodine containing precursors are used.

Since the temperature of the pyrolysis source can be increased to values high enough to fully deplete the molecular precursor, it was assumed that those are the best conditions with which photodissociation signal can be collected. This is definitely true since parent contamination of the radical beam would not be a problem under such conditions. However, the third chapter of this dissertation will show that the chemistry taking place inside the pyrolysis source is not as simple as previously thought, and that sometimes it may be necessary to maintain the source at lower temperatures where the precursor molecules are not fully depleted from the molecular beam. *tert*-Butyl radicals were

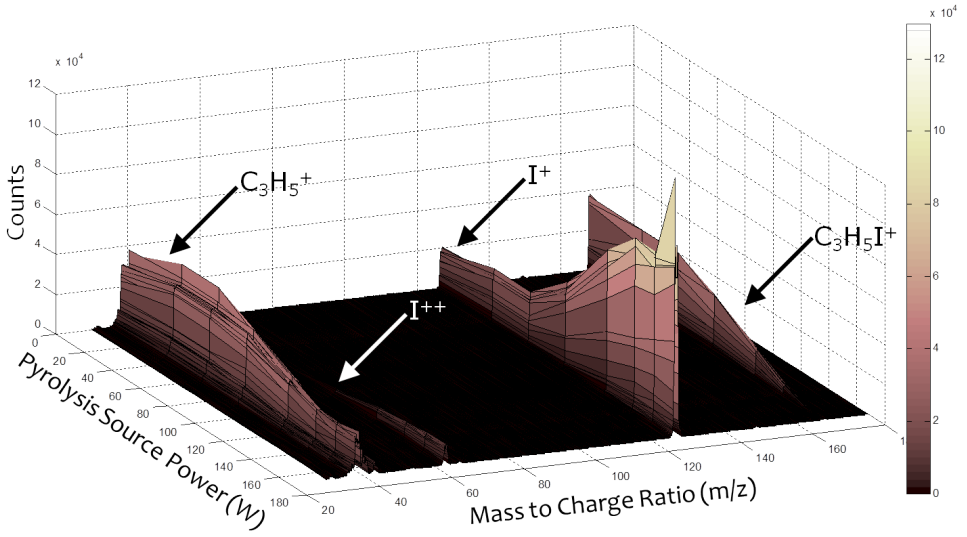

Fig. 2.6 Mass spectra of the allyl iodide (C_3H_5I) at different pyrolysis temperatures. The peak at *m/z* = 168 is fully depleted at high temperatures, while the peak at *m/z* = 41 persists.

produced by pyrolysis of azo-*tert*-butane precursor entrained in a helium beam. In this case, the precursor used did not absorb at 248 nm while the radical did; which explains why photodissociation signal is not observed in the upper most trace of Figure 2.7 obtained with a cold pyrolysis source. At intermediate source temperatures photodissociation signal was observed, while at even higher source temperatures photodissociation signal could not be detected. This was interpreted to mean that at high temperatures the pyrolysis source also pyrolysed the radicals produced, thus depleting them from the beam. The maximum photodissociation signal was observed at temperatures where the *m/z* = 56 and 57 peaks are equal in intensity.

While this source is somewhat universal and can be applied to a wide variety of systems it is limited in that the formation of a radical that is more weakly bound than the precursor is not easily achieved, if at all. In this situation, radicals are formed in an environment too hot for them to survive. Another limitation of the pyrolysis source is in the radical concentrations that can be produced. The precursor molecule is seeded in a rare gas beam at concentrations below 1% since higher concentrations can lead to polymerization of the radicals. Luckily, if the radicals polymerize it can be checked by collecting mass spectra over a larger mass range, up to a mass to charge ratio two to three times larger than the mass of the radical or precursor used.

The pyrolysis source uses high temperatures to produce neutral free radicals, but it is not necessary to know the actual temperature since the mass spectrum of the molecular beam can be used to probe the chemistry taking place inside the source. A pure noble gas beam can be used to determine the source temperature as well as a pyrometer, since the SiC tube glows, but usually the source is monitored with the mass spectrometer. Even if we

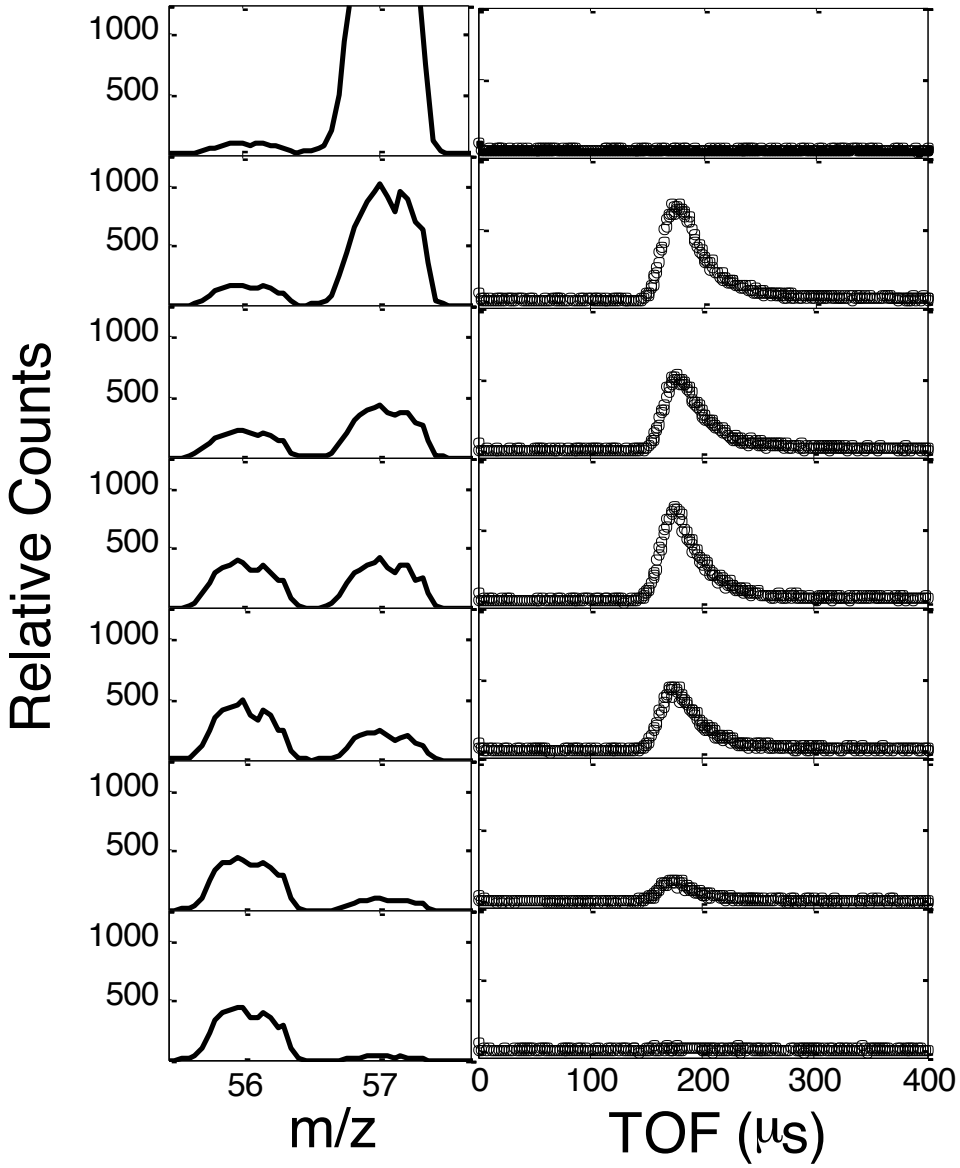

Fig. 2.7 Time-of-flight signal collected at *m/z* = 56 at a lab angle of 6° for the 248 nm photodissociation of a azo-*tert*-butane ($C_4H_9N_2C_4H_9$) molecular beam at different pyrolysis temperatures. The mass spectra on the left show the variation in intensity of the *m/z* = 56 and 57 mass peaks with increasing pyrolysis temperatures. The spectra on the right were later determined to be produced from hydrogen atom loss from the *tert*-butyl radical (*t*-C_4H_9) (see chapter 3).

identify the products made, the dynamics taking place inside the pyrolysis tube are not well understood. Preliminary fluid dynamics simulations performed by the Ellison group[56] estimate the pressure inside the tube to be about 10% of the stagnation pressure and the residence time to be between 50 and 100 μs. They also hypothesize that the gas temperature is within 200 K of the wall temperature as it approaches the tube exit.[56] This means that microtubular reactors such as the flash pyrolysis source are quite good at thermally heating molecular beams, and that a supersonic expansion can be obtained at the exit of the tube. These characteristics agree with the observed performance and

exemplify the versatility of the flash pyrolysis source in producing neutral free radicals in collisionless environments.

Chapter 3

Photodissociation Dynamics of the *t*-Butyl Radical via Photofragment Translational Spectroscopy at 248 nm

*The content and figures of this chapter are reprinted or adapted with permission from Negru, B.; Just G. M. P.; Park D.; Neumark D. M., "Photodissociation dynamics of the t-Butyl radical via photofragment translational spectroscopy at 248 nm," Phys. Chem. Chem. Phys., **2011**, 13, 8180-8185. Copyright 2011 Royal Society of Chemistry.*

The photodissociation dynamics of the *t*-butyl radical (*t*-C_4H_9) were investigated using photofragment translational spectroscopy. The *t*-butyl radical was produced from flash pyrolysis of azo-*tert*-butane and dissociated at 248 nm. Two distinct channels of approximately equal importance were identified: dissociation to H + 2-methylpropene, and CH_3 + dimethylcarbene. Neither the translational energy distributions that describe these two channels nor the product branching ratio are consistent with statistical dissociation on the ground state, and instead favor a mechanism taking place on excited state surfaces.

3.1 Introduction

Alkyl radicals are prototypical open-shell species that play a central role in chemistry. They are key intermediates in combustion chemistry and hydrocarbon cracking; many combustion mechanisms are initiated by unimolecular or bimolecular reactions of closed-shell hydrocarbons to form alkyl radicals;[57] the subsequent chemistry of these species is of considerable interest in optimizing the efficiency of combustion. Alkyl radicals also play a key role in planetary atmospheric[58] and interstellar[59] chemistry. While the energetics, kinetics, and ground state spectroscopy of many of the smaller alkyl radicals

are reasonably well understood, characterization of their electronic spectroscopy and photochemistry is complicated by their high reactivity and, in contrast to many other radicals, the general absence of low-lying, long-lived electronic states.[60,61] In this paper, the photochemistry of the simplest tertiary alkyl radical, the *t*-butyl radical (*t*-C_4H_9) is investigated by photofragment translational spectroscopy in order to unravel its primary photochemistry and its dissociation dynamics subsequent to electronic excitation at 248 nm.

The *t*-C_4H_9 radical has been investigated extensively by both experimental and theoretical methods. The geometry of the *t*-butyl radical was under dispute for many years[62,63] until its pyramidal structure of C_{3V} symmetry was identified by electron spin resonance[64,65] and later confirmed by unrestricted Hartree-Fock calculations.[66] The recommended[67] heat of formation at 298 K, 12.3±0.4 kcal/mol, was obtained from temperature-dependent kinetics studies combined with thermochemical calculations.[68] The ground state of this radical was explored by infrared spectroscopy[69,70,71] while ultraviolet absorption spectroscopy[72,73] was used to describe the Rydberg character of the excited state. Three low-lying transitions centered around 333, 253, and 233 nm were assigned to the 3s, 3p, and 3d transitions, respectively. Several values of the vertical and adiabatic ionization potential of the *t*-butyl radical have been reported,[74,75,76] the most recent of which is an adiabatic value of 6.87 eV.[77]

The reaction kinetics of *t*-butyl have been studied in the condensed phase[78,79,80] and the gas phase.[68,81,82,83,84,85,86,87] The unimolecular decay of *t*-butyl is of particular relevance to this work as a reference point for ground state dissociation dynamics. Knyazev *et al*.[83] determined the rate constant for thermal decomposition of *t*-butyl from 712-779 K using photoionization mass spectrometry. They developed a transition state theory model for the decomposition reaction *t*-$C_4H_9 \rightarrow C_4H_8+H$ that reproduced their temperature-dependent rate constants for *t*-butyl decay as well as rate constants previously measured for the reverse reaction. Their analysis yielded a small exit barrier of 1.5 kcal/mol for H atom loss, a result in agreement with recent electronic structure calculations by Blowers and Zheng.[88]

Electronic excitation of *t*-butyl radical in the ultraviolet can lead to dissociation by multiple pathways:[28]

1) $(CH_3)_3C + h\nu \rightarrow (CH_3)_2CCH_2 + H$ ΔH_0=36 kcal/mol (3.1)

2) $(CH_3)_3C + h\nu \rightarrow CH_3CCH_3 + CH_3$ ΔH_0=88 kcal/mol (3.2)

3) $(CH_3)_3C + h\nu \rightarrow (CH_3)_2CHCH_2 \rightarrow CH_3CHCH_2 + CH_3$ ΔH_0=28 kcal/mol (3.3)

On the ground state surface, and using the above energetics, H atom loss proceeds through a transition state that lies 37.5 kcal/mol above the *t*-butyl minimum. The *t*-butyl radical can lose a methyl radical directly to form singlet dimethylcarbene (channel 2), or it can isomerize to form the *iso*-butyl radical by a [1,2]-H-shift and subsequently undergo CH_3 loss to form propene (channel 3). The calculated barrier height to isomerization is

48 kcal/mol,[89] so channel (1) would be the most facile channel if dissociation were to occur on the ground state surface.

The UV photodissociation of *t*-butyl radical was previously studied by Zierhut *et al*.[90] They excited the radicals from 335 to 266 nm and detected atomic H products by multiphoton ionization. They measured the rate of H atom production to be 10^7-10^8 sec^{-1}, depending on wavelength, and characterized the H atom translational energy distribution by Doppler spectroscopy. At 266 nm, they found a lower reaction rate than expected from a statistical model, and that 38% of the available energy was channelled into translation. Channels (2) and (3), the CH_3 loss channels, could not be detected in their experiment. More recently, Noller *et al*.[89] investigated the femtosecond decay dynamics of *t*-butyl using time-resolved photoelectron spectroscopy. They observed sub-ps lifetimes for the initially excited state upon excitation of the 3s band (~330 nm), and a lifetime of 2 ps upon excitation of the 3p band at 266 nm. Accompanying electronic structure calculations suggested that 3s and 3p excited states interact with a repulsive valence state leading to channel (2) products, although again, this channel was not directly observed.

The UV photoexcitation experiments raise questions regarding whether H atom loss is the sole dissociation pathway, and whether the overall mechanism involves excited state dissociation or internal conversion followed by dissociation on the ground state. These issues motivate the experiments reported here, where we investigate its photodissociation dynamics following excitation at 248 nm, near the maximum of the previously observed 3p band. The experimental technique, photofragment translational spectroscopy,[91] allows all dissociation channels to be monitored, in principle. Our results identify the previously observed H atom loss channel, but also show evidence for a CH_3 loss channel produced with approximately equal intensity. Translational energy distributions are determined for both channels. The data presented here provide new insight into the overall mechanism of *t*-butyl photodissociation, in particular suggesting that dissociation occurs on one or more excited state surfaces rather than the ground state.

3.2 Experiment

A molecular beam photodissociation apparatus with a rotatable detector was used to perform the work shown here. Details of the flash pyrolysis radical source and of the detection scheme employed have been described previously.[10,24,92] In brief, a mixture of azo-*tert*-butane, $C_8H_{18}N_2$, in He was obtained by bubbling 1.5 atm of He through a liquid sample of the parent molecule maintained at 0^0 C in an ice-bath. The *t*-butyl radical beam was subsequently generated from the pyrolysis of azo-*t*-butane molecules within a resistively heated SiC tube mounted to a piezo-activated pulsed valve.

The *t*-butyl radical beam was collimated by two skimmers and crossed at 90^0 with the 2 by 4 mm^2 focused beam spot of the photodissociation laser at 248 nm. Pulse energies of 40 mJ were obtained from an excimer laser (GAM EX100/500). The scattered

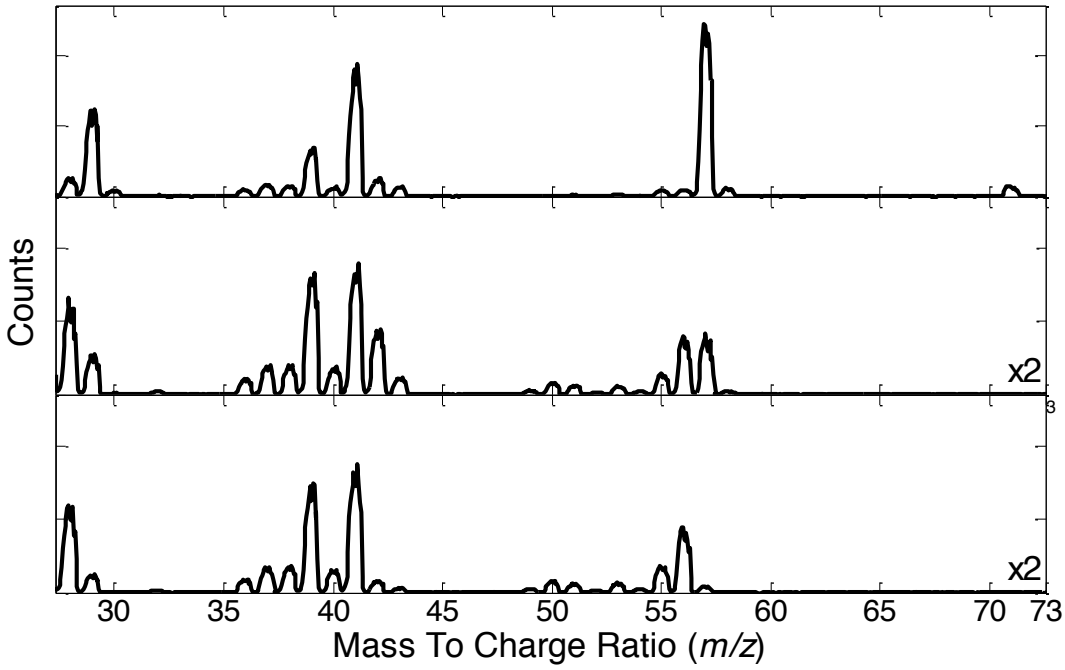

Fig. 3.1 Mass spectra of the azo-*tert*-butane beam at different pyrolysis temperatures. The top trace was taken with a cold pyrolysis tube and shows the presence of the $C_4H_9N^+$ fragment at m/z = 71. The middle trace was collected at an intermediate pyrolysis temperature, while the bottom trace shows the mass spectrum at high pyrolysis temperatures. Experimental data were obtained under conditions used to produce the middle trace, where the intensities of the peaks at m/z = 57 ($C_4H_9^+$) and 56 ($C_4H_8^+$) are about equal.

photofragments were detected in the plane defined by the molecular and laser beams as a function of the laboratory angle, Θ, measured with respect to the molecular beam. The neutral photofragments were ionized with an electron impact ionizer, mass-selected with a quadrupole mass filter, and detected with a Daly style ion detector.[93] Time-of-flight (TOF) spectra consisting of ion counts as a function of arrival time relative to the laser pulse were acquired with the use of a multichannel scaler interfaced to a computer. The pulsed valve and laser repetition rates were 200 Hz and 100 Hz, respectively, to allow for background subtraction. The TOF spectra were analyzed by fitting them to an iterative forward convolution of a center-of-mass photofragment translational energy and angular distribution.

A retractable slotted chopper disk was used for the characterization of the radical beam. Flow velocities were close to 1600 m/s with a speed ratio of ~5. Figure 3.1 shows mass spectra of the molecular beam taken for different SiC tube temperatures. The top trace shows mass spectra acquired with an unheated pyrolysis source. The largest m/z ratio where signal can be observed from the parent molecule is at 71. Although the pyrolysis source is unheated, peaks at m/z = 57 corresponding to $C_4H_9^+$ and several smaller m/z ratios are also observed in this mass spectrum owing to dissociative ionization of the parent molecule. The middle trace shows the mass spectrum obtained with the pyrolysis source heated to intermediate temperatures. Under these operating conditions, the peak previously observed at m/z = 71 is absent. The intensities of the peaks observed at m/z =

56 and *m/z* = 57 are about the same. The bottom trace results from even higher temperatures. Here the peak at *m/z* = 56 is considerably larger than that at 57. This trend is attributed to fragmentation of the *t*-butyl radical in the pyrolysis source by the elimination of an H atom. To minimize this fragmentation, TOF data was collected at SiC tube temperatures corresponding to the middle trace from Figure 3.1 where the ratio of *m/z* = 56 and 57 peaks was close to unity. These conditions also produced the maximum off-axis photodissociation signal at *m/z* = 56, attributed to H atom loss from *t*-butyl.

3.3 Results

Time-of-flight spectra were taken for *m/z* = 56 ($C_4H_8^+$), *m/z* = 42 ($C_3H_6^+$), and *m/z* = 15 (CH_3^+), the primary ionized fragments for the H loss and CH_3 loss channels, and for several of the daughter ions formed by dissociative ionization in the electron impact ionizer. The data shown in Figure 3.2 include representative TOF spectra for *m/z* = 56, *m/z* = 42, and *m/z* = 15 collected at multiple laboratory scattering angles Θ. The TOF data are represented by open circles and are background-subtracted as described above. Simulations obtained via forward convolution (see Analysis Section 3.4) are represented as black lines. Signal was not collected for *m/z* = 1 owing to poor kinematic factors and large background at this mass-to-charge ratio.

The TOF spectra at *m/z* = 56 in Figure 3.2 consist of a single peak with greater intensity at 6^0 than at 4^0. No signal at this *m/z* ratio was observed beyond $\Theta = 17^0$. The *m/z* = 42 signal in Figure 3.2 comprises two peaks. The slower peak is only observed at laboratory angles below 17^0 and occurs at the same flight time as the *m/z* = 56 peak at the same laboratory angle, while the fast peak is present at much larger angles. In turn, three distinct peaks can be identified in the TOF spectra collected for *m/z* = 15, also shown in Figure 3.2. The slowest peak behaves similarly to the peak observed at *m/z* = 56 and is not present in TOF spectra collected at laboratory angles above 17^0. The middle peak is very weak, while the fastest peak can be clearly observed over a large angular range.

A preliminary interpretation of the TOF spectra from Figure 3.2 indicates that at least two dissociation channels are present. Kinematic considerations set a maximum detection angle of $\Theta = 17^0$ for any heavy photofragments resulting from H atom loss from the *t*-butyl radical via channel (1). Since the single peak in the *m/z* = 56 spectra disappears beyond this angle, we attribute this feature to H atom loss from the *t*-butyl radical; other possible sources are considered below. The multiple contributions to the *m/z* = 42 and 15 TOF spectra can be separated into peaks that can be observed over a small and large angular distribution. The peak confined to smaller angles is very similar to the photodissociation signal observed for *m/z* = 56, and is thus believed to originate from dissociative ionization of the heavy fragment formed by H atom loss. The other contributions span a much larger angular range, as seen in Figure 3.2, far beyond the

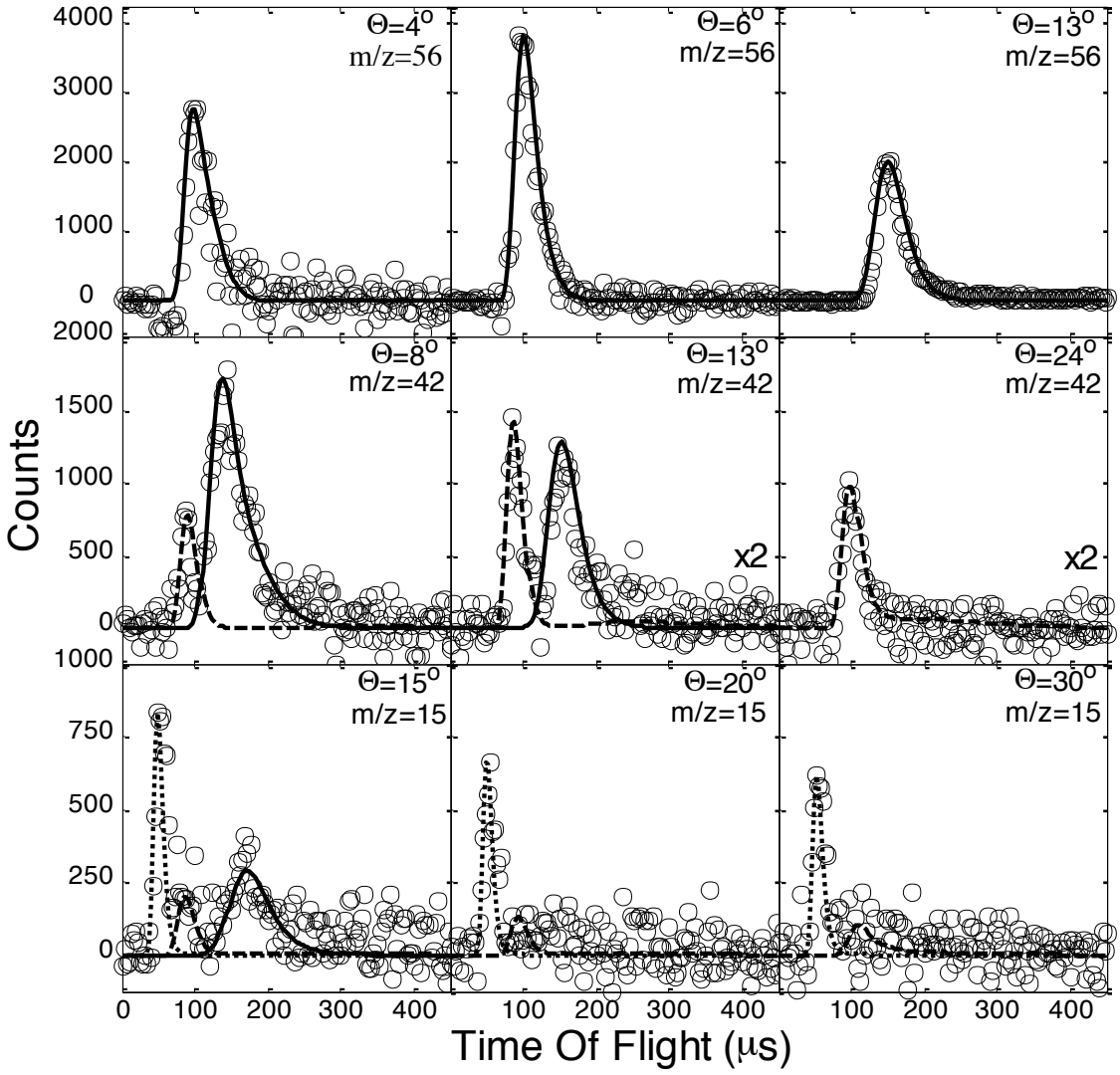

Fig. 3.2 Representative TOF spectra for m/z = 56, 42, and 15 collected at $\Theta_{lab} = 4^0$- 30^0 obtained from 248 nm photodissociation of t-C_4H_9. The TOF data are represented by open circles, while the fits are represented by lines. The solid line fits were generated with the P(E_T) distribution from Figure 3.3 and represent the signal from C_4H_8 photoproducts. The dashed and dotted fits were generated from the P(E_T) distribution from Figure 3.4 and represent C_3H_6 and CH_3 products, respectively.

maximum scattering angle for H atom loss. If these features are from channel (2) or (3), i.e. CH_3 loss from t-butyl, then they should be "momentum-matched," in that a single center-of-mass translational energy distribution should fit the TOF peaks at m/z = 42 and 15. This hypothesis is considered further in the next section.

In assigning the observed features to the photodissociation of t-C_4H_9, one must consider other possible sources of signal from either the parent molecule or other species produced in the pyrolysis source. For example, the azo-t-butane parent used for production of the t-butyl radicals is known to have a strong n→π* absorption band centered around 365 nm,[90] but a low absorption cross section around 250 nm. However, the conditions chosen

for *t*-butyl production, as shown in the middle trace of Figure 3.1, do not show the presence of a peak at *m/z* = 71, indicating minimal presence of the parent in our beam. Another source of signal could be the formation of other chemical species in our pyrolysis source. *t*-Butyl radicals could polymerize to form larger carbon species, but these would be detected by our quadrupole mass spectrometer.

An additional complication arises from the observation that at high source temperatures (bottom panel, Figure 3.1), the *m/z* = 57 peak drops considerably in favour of the *m/z* = 56 peak. This trend presumably reflects unimolecular decay of *t*-butyl to H + C_4H_8 (2-methylpropene), a reaction known to occur above 700 K,[83] and raises the concern that photodissociation products from C_4H_8 can interfere with signal from *t*-butyl dissociation. We attempted to minimize *t*-butyl decomposition in the source by operating under temperatures just high enough to eliminate the peak at *m/z* = 71 (middle panel, Figure 3.1). Moreover, 2-methylpropene has no appreciable absorption cross section at 248 nm, although it does absorb strongly and photodissociate at 193 nm.[94] Finally, we note that scattered dissociation signal at *m/z* = 56 cannot originate from C_4H_8 in the beam, nor can momentum-matched signal at *m/z* = 15 and 42. Based on these considerations and the analysis in Section 3.4, we believe that contributions from C_4H_8 to our data are unimportant.

3.4 Analysis

In this section, center-of-mass photofragment energy and angular distributions, $P(E_T,\theta)$, for the various product channels are obtained by fitting the TOF spectra of the photodissociated fragments. The preliminary interpretation discussed previously is tested by trying to fit the entire data set to only two mass channels: H atom loss (channel 1) and CH_3 loss (channels 2,3) The $P(E_T,\theta)$ distribution can be rewritten in terms of the uncoupled center-of-mass translational energy $P(E_T)$ and angular distribution $I(\theta,E_T)$:

$$P(E_T, \theta) = P(E_T)I(\theta,E_T) \tag{3.4}$$

For the geometry of our experiment, where the rotational axis of the detector is normal to the plane defined by the molecular and laser beams, an anisotropic angular distribution is possible even with unpolarized excimer laser beams. In fact, a satisfactory fit to the data was obtained by assuming an isotropic angular distribution for all values of E_T, and the simulations shown in Figure 3.3 and Figure 3.4 were produced under this assumption. The PHOTRAN[95] forward convolution program was used to fit the TOF spectra for all the data sets according to an assumed $P(E_T)$ distribution. The input $P(E_T)$ for a particular channel was adjusted point-wise until a best fit was simultaneously obtained for all the TOF spectra of that channel. The total center-of-mass translational energy, E_T, is given by

$$E_T = h\upsilon + E_0 - E_{int} - D_0 \tag{3.5}$$

In this equation, $h\upsilon$ is the photon energy (115 kcal/mol at 248 nm), E_0 is the initial energy of the *t*-butyl radicals, E_{int} is the total internal energy of the fragments, and D_0 is the dissociation energy for the channel of interest. The maximum translational energy for a particular dissociation channel is given by $h\upsilon$ - D_0 if the *t*-butyl radicals produced are internally cold, i.e. $E_0 = 0$. These maximum values E_T^{max}, are 79, 27, and 87 kcal/mol for channels (1-3), respectively.

The P(E_T) distribution used to simulate the fit for *m/z* = 56 TOF spectra from Figure 3.2 peaks close to 35 kcal/mol and is shown in Figure 3.3 and is set to zero probability beyond E_T^{max} = 79 kcal/mol. The average translational energy $\langle E_T \rangle$ is 35 kcal/mol. This distribution was also used to fit the slow TOF peak observed in the TOF spectra for $\Theta \leq$ 17° obtained for *m/z* = 42 and 15. This distribution drops to zero well before E_T^{max}, so even allowing for a higher value owing to internal excitation of the radical is unlikely to have a significant effect on its overall shape.

The P(E_T) distribution from Figure 3.4 was used to fit the fast peaks in the TOF spectra of *m/z* = 42 and 15 simultaneously. Since the TOF spectra for the two ion masses are reproduced with only a single P(E_T) distribution, these spectra are assigned to momentum-matched C_3H_6 and CH_3 photofragments from *t*-butyl dissociation at 248 nm. This P(E_T) peaks close to 18 kcal/mol and has an average translational energy of 17 kcal/mol and extends to E_T^{max} = 27 kcal/mol. This P(E_T) distribution cannot be cut off below 27 kcal/mol, but it can be extended out to 35 kcal/mol and still provide an adequate fit to the TOF spectra. As discussed further in the discussion section, this distribution is in considerably better agreement with the energetics for channel (2), CH_3 + dimethylcarbene, than channel (3).

The universal detection scheme used in this experiment enables extraction of the product branching ratio through examination of relative intensities in the TOF spectra at

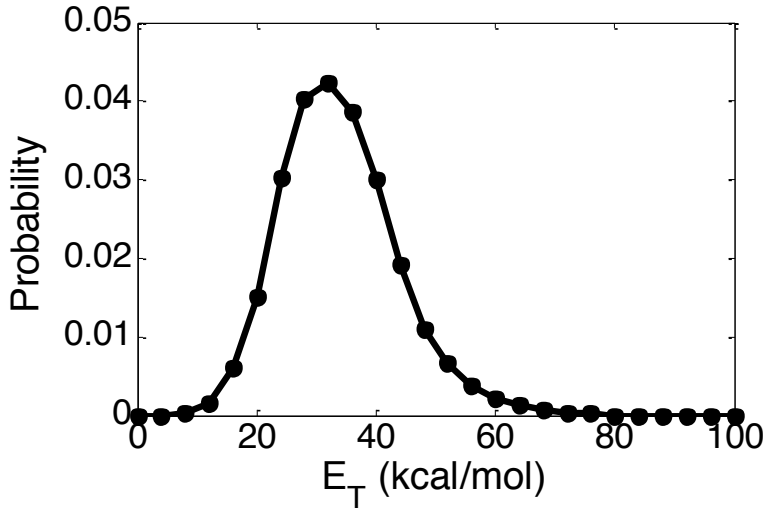

Fig. 3.3 Center-of-mass P(E_T) distribution from *t*-butyl photodissociation at 248 nm to H + C_4H_8. The maximum available translational energy available for channel (1) is 79 kcal/mol.

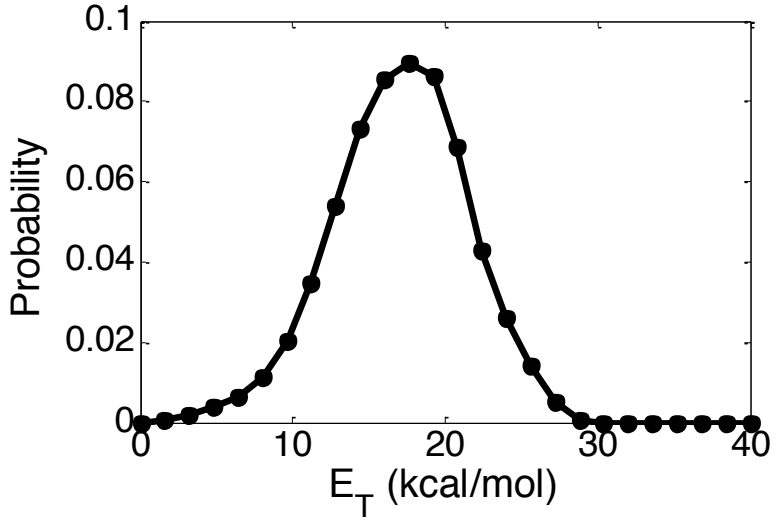

Fig. 3.4 Center-of-mass P(E_T) distribution from *t*-butyl photodissociation at 248 nm used to fit the methyl loss data from Figure 3.2. The maximum available translational energy available for channels (2) and (3) is 27 and 87 kcal/mol, respectively.

scattering angles and ion masses where signal from both channels can be seen. The data at *m/z* = 42 (see Figure 3.2) are best for this determination. The branching ratio between H atom loss and CH_3 loss is given by

$$\frac{H\ loss}{CH_3\ loss} = R \times \frac{\sigma_{C_3H_6}}{\sigma_{C_4H_8}} \times \frac{f_{C_3H_6}}{f_{C_4H_8}} \qquad (3.6)$$

Here R is the ratio of the relative weights of the P(E_T) distributions used by the fitting program to reproduce the relative intensities of the two contributions seen in Figure 3.2 for *m/z* = 42. It is multiplied by the ratio between the relative electron impact cross sections of the C_4H_8 and C_3H_6 photofragments and the ratio between the signal fractions of the two channels observed at *m/z* of 42. Each fraction was calculated by comparing the signal level at *m/z* = 42 to the other *m/z* ratios in the electron impact mass spectrum of that species. The electron impact mass spectrum used for 2-methylpropene was adapted from the literature,[28] while the mass spectrum used for dimethylcarbene was determined by taking photodissociation TOF spectra for all possible daughter ion masses at $\Theta = 18^0$. These spectra were all due to dissociative ionization of the C_3H_6 photofragment and were thus fit with the same P(E_T) distribution. The H loss/ CH_3 loss branching ratio was found to be 1.1 ± 0.3; estimated error bars are adapted from Schmoltner.[96]

3.5 Discussion

This study had two main objectives: to determine if the primary photochemistry of the *t*-butyl radical is limited to H atom loss, and to gain insight into the overall

photodissociation mechanism. We observe both H atom loss and CH_3 loss. The translational and angular energy distributions of these products as well as the branching ratio provide insight into whether CH_3 loss involves channel (2) and/or channel (3), and whether dissociation occurs on an excited state surface or by internal conversion to the ground electronic state.

Photodissociation data attributed to channel (1), H atom loss, was observed at m/z = 56 and is complementary to the previous H atom detection study performed by Zierhut *et al*.[90] The P(E_T) distribution in Figure 3.3 peaks well away from zero with $\langle E_T \rangle$ = 35 kcal/mol. The previously determined P(E_T) for this channel was extracted from the Doppler-profile of the H atom signal and also had a large average energy $\langle E_T \rangle$ = 27 kcal/mol. The differing values of $\langle E_T \rangle$ may reflect the difference of 8 kcal/mol in the excitation energy used in the two experiments as well as possible differences in the internal temperature of the radicals produced. In any case, the calculated ground state exit barrier for channel (1) is only 1-2 kcal/mol.[83,88] Hence, if channel (1) were to occur by internal conversion to the ground state followed by statistical decay, one would expect the associated P(E_T) distribution to peak near E_T = 0, in contrast to the distribution in Figure 3.3. It thus appears that channel (1) occurs on an excited state surface, or by non-statistical decay on the ground state; the latter process cannot be ruled out given that the photon energy exceeds the energy needed to surmount the exit barrier by ~80 kcal/mol.

We also observed significant methyl loss from *t*-butyl at 248 nm, which may proceed by channel (2) or channel (3). Channel (2) is more endothermic by 60 kcal/mol but involves simple C—C bond cleavage to form dimethylcarbene, whereas channel 3 proceeds by a [1,2]-H-shift to form the *iso*-butyl radical followed by dissociation to CH_3 + propene. The barrier to this isomerization on the ground state surface was calculated to be 2.08 eV (48 kcal/mol) by Noller *et al*.[89] The data for CH_3 loss are fit well by the P(E_T) distribution in Figure 3.4, for which the E_T^{max} is 27 kcal/mol, which is the maximum value allowed for channel (2) assuming no reactant internal energy. In contrast, E_T^{max} for channel (3) is 87 kcal/mol, well beyond the range of the distribution in Figure 3.4. Hence, our data indicate that methyl loss proceeds via channel (2), and the derived branching ratio of 1.1±0.3 is assigned to the channel (1)/channel (2) ratio.

These considerations provide insight into whether CH_3 loss occurs on the ground state or on an excited state surface. Several factors argue against ground state dissociation. The P(E_T) distribution for channel (2) peaks well away from E_T = 0, whereas one would expect a distribution peaking much closer to zero for simple bond fission on the ground state surface. Secondly, on the ground state surface, the available energy exceeds the calculated isomerization barrier for the [1,2]-H-shift by 67 kcal/mol, so at least some isomerization followed by dissociation to channel (3) should occur, even if the transition state is tighter than the loose (but considerably higher energy) transition state expected for channel (2) on the ground state. Finally, if CH_3 loss were to occur on the ground state, then significant hydrogen atom loss would also be seen on the ground state, since channel (1) is considerably lower in energy than channel (2) and has a fairly small exit barrier. The approximately equal branching for the two channels does not concur with

the branching ratio expected for statistical dissociation on the ground state surface, which should significantly favour hydrogen atom loss.

Our results and conclusions are of interest in light of the time-resolved photoelectron spectroscopy of *t*-butyl by Noller *et al*.[89] This work found sub-ps lifetimes upon excitation of the 3s state at 324 nm, and a 2 ps lifetime for the 3p state excited at 268 nm; the latter state is the same state accessed in our experiment. These time scales represent considerably faster dynamics than the dissociation rates for H-atom loss (10^9-10^8/sec) reported by Zierhut *et al*.[90] at similar excitation wavelengths. In order to understand this disparity between time scales, Noller *et al*.[89] pointed out the likely presence of a valence state lying above the 3s and 3p states that correlates to CH_3 + singlet dimethylcarbene products, i.e. channel (2). This state crosses the 3p, 3s, and ground states of *t*-butyl en route to dissociation to channel (2). They proposed that these crossings provide an efficient pathway for rapid nonradiative decay of the 3s and 3p states to the ground state, whereupon relatively slow H atom loss could occur. The crossing between the valence and 3p states also provides a direct route for dissociation to channel (2) that bypasses the ground state; such a mechanism may thus explain the excited state dissociation implied by our results.

Given the strong evidence for CH_3 loss occurring on an excited state surface, it seems likely that this is also the case for hydrogen atom loss, particularly in light of the P(E_T) distributions for channel (1) measured by us and by Zierhut *et al*.[90] It remains to be seen how the slow rates for H atom production seen by Zierhut *et al*.[90] can be reconciled with these results.

3.6 Conclusions

The photodissociation dynamics of the *t*-butyl radical have been explored at 248 nm using photofragment translational spectroscopy. Translational energy P(E_T) distributions and product branching ratios were determined for two separate dissociation pathways, one for H atom loss and one for methyl loss. On the ground state potential energy surface, H atom loss (channel 1) is expected to be a nearly barrierless process, while the P(E_T) reveals products with large translational energy. The P(E_T) distribution for the methyl loss channel extends to a maximum of 27 kcal/mol and is attributed to the formation of dimethylcarbene (channel 2), rather than isomerization followed by dissociation to propene. The branching ratio was determined to be 1.1±0.3, indicating approximately equal branching between channels (1) and (2). Neither the P(E_T) distributions for the two channels nor the branching ratio are consistent with statistical dissociation on the ground state surface, and the CH_3 loss channel in particular appears to be an excited state process.

3.7 Acknowledgments

This work was supported by the Director, Office of Basic Energy Sciences, Chemical Science Division of the U.S. Department of Energy Under Contract No. DE-AC02-05CH11231.

Chapter 4

Photodissociation of isobutene at 193 nm

The collisionless photodissociation dynamics of isobutene (*i*-C_4H_8) at 193 nm via photofragment translational spectroscopy (PTS) are reported. Two major photodissociation channels were identified: H + C_4H_7 and CH_3 + CH_3CCH_2. Translational energy distributions indicate that both channels result from statistical decay on the ground state surface. Although the CH_3 loss channel lies 13 kcal/mol higher in energy, the CH_3 : H branching ratio was found to be 1.7 (5), in reasonable agreement with RRKM calculations.

4.1 Introduction

Isobutene, *i*-C_4H_8, (2-methylpropene) is the smallest branched alkene. It plays a key role in combustion chemistry as an intermediate in the pyrolysis of *iso*-octane and in the oxidation of fuel additives such as MTBE and ETBE (methyl and ethyl *t*-butyl ether).[97] The chemistry of isobutene in the Earth's troposphere, notably its reactions with NO_2 and NO_3,[98,99] is of interest, as are its reactions with free radicals in the atmosphere of Titan in order to form larger hydrocarbons.[100] Isobutene has been implicated as a product in the $O(^3P)$ + *t*-C_4H_9(t-butyl) radical-radical reaction[101] and from the photodissociation of *tert*-C_4H_9.[90,102] However, the photodissociation of isobutene itself has not been reported previously. In this paper, we investigate the collisionless photodissociation of isobutene at 193 nm in order to gain new insights into its unimolecular photochemistry and dissociation dynamics.

The work presented here is motivated by numerous studies of the bimolecular and unimolecular kinetics of isobutene in shock tubes and flames.[103,104,105,106,107] These studies have focused on elucidating the mechanisms for the oxidation and pyrolysis of isobutene. An issue arising from this body of work is the identity of the products arising from the unimolecular decay of isobutene. In some kinetics studies, reaction mechanisms are proposed in which only H atom loss is included,[106] whereas others also include the somewhat higher energy CH_3 loss channel.[103,107,108] Photodissociation measurements provide unambiguous identification of the primary products from photoexcitation to an excited electronic state. In cases where dissociation proceeds via internal conversion to the ground state followed by statistical decay, the results of photodissociation experiments can have direct bearing on the interpretation of kinetics experiments in which it is often very difficult to identify product channels for specific reactions.

Photodissociation of isobutene is also of interest in light of previous work by Zierhut *et al.*[90] and our group[109] on the photodissociation of the *t*-C_4H_9 radical near 248 nm. One concern in those experiments was that some observed channels were from the photodissociation of vibrationally hot isobutene produced in the pyrolysis source used to generate *t*-butyl radical rather than from *t*-butyl itself. An independent study of isobutene photodissociation could thus corroborate the interpretation of the previous experiments on *t*-butyl.

The UV absorption spectrum of the isobutene molecule begins around 205 nm and comprises numerous closely spaced bands;[110,111] the band around 193 nm has been assigned to the lowest-lying $\pi\pi^*$ transition.[112,113] Excitation at 193 nm can lead to photodissociation by two bond cleavage channels involving loss of either an H atom or a CH_3 group:

$$1)\quad (CH_3)_2CCH_2 + h\nu \rightarrow \cdot CH_2CH_3CCH_2 + H \qquad \Delta H_0 = 88.3 \text{ kcal/mol} \qquad (4.1)$$

$$2)\quad (CH_3)_2CCH_2 + h\nu \rightarrow CH_3C\cdot CH_2 + CH_3 \qquad \Delta H_0 = 100.9 \text{ kcal/mol} \qquad (4.2)$$

The 2-methylallyl radical from, channel (1), can further dissociate to form allene (C_3H_4) via the loss of a methyl group.[60] The barrier to this dissociation process has been calculated by Li *et al.*[114] to be 55.5 kcal/mol. Furthermore, the 2-propenyl radical from channel (2) can undergo a 1,2-hydrogen shift over an isomerization barrier of 45.4 kcal/mol to form the allyl radical.[49] Figure 4.1 shows the primary energetics for channels (1) and (2) as well as the barrier heights and energies for subsequent dissociation and isomerization.

In this work, we investigate the collisionless photodissociation of isobutene at 193 nm using molecular beam photofragment translational spectroscopy. This experiment yields the kinetic energy and angular distribution for each photofragmentation channel, enabling the direct identification of the primary photofragments and providing insight into the dissociation mechanism. We find here that both channels (1) and (2) occur with kinetic energy distributions consistent with statistical decay on the ground state surface. The

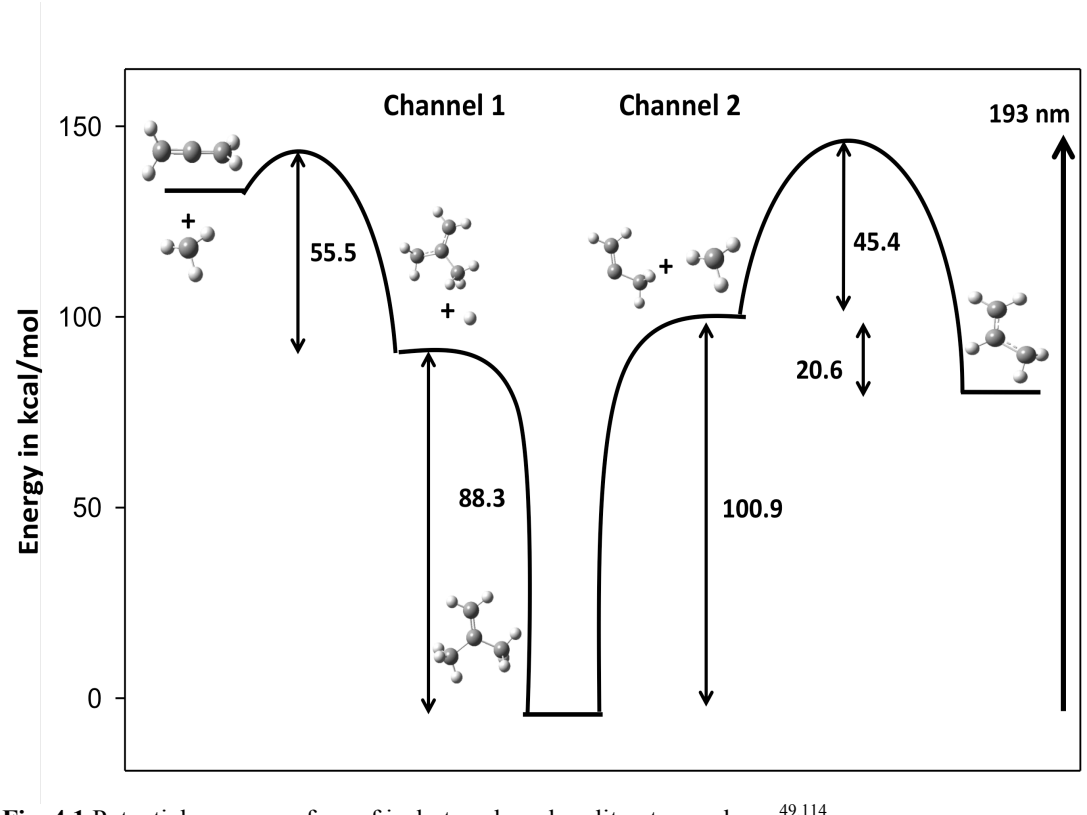

Fig. 4.1 Potential energy surface of isobutene based on literature values. [49,114]

branching ratio is about 1.7 (5) in favour of the higher energy channel (2). These results are interpreted based on simple RRKM considerations.

4.2 Experiment

The molecular beam photodissociation apparatus has been described in previous papers.[10,17,24]A fixed molecular beam is intersected by a pulsed laser and a rotatable detector is used to analyze the photodissociation products via electron impact ionization mass spectroscopy. Photofragment time-of-flight measurements for ion masses of interest are taken at a variety of laboratory scattering angles Θ_{lab}.

In more detail, a pulsed molecular beam of isobutene was formed using a piezo-activated valve (Physik Intrumente ,PI) at a repetition rate of 200 Hz. The gas mixture was 1% isobutene (purity greater than 99%, SynQuest Labs Inc, FL) in helium or neon with a backing pressure of 25 psig. The molecular beam was collimated with two skimmers, one of which separated the source chamber from the main chamber where dissociation and detection occurs. In the main chamber, the molecular beam was crossed at a 90^0 by a focused photodissociation beam (2x4 mm) produced by an ArF (193 nm) excimer laser (Lambda-Physik) operating at a repetition rate of 100 Hz with a typical pulse energy of 40 mJ. The scattered photofragments were detected in the plane defined by the molecular

and laser beams as a function of the laboratory angle, Θ_{lab}, measured with respect to the molecular beam. After reaching the triply differentially pumped detection region, the neutral photofragments were ionized by electron impact ionization (77 eV), mass-selected using a quadrupole mass spectrometer, and observed with a Daly style ion detector. Photofragment time of flight (TOF) spectra with respect to the laser pulse were obtained by measuring ion signal as a function of time and were digitally recorded by the use of a multichannel scaler connected to a PC-computer. Spectra in which helium was the carrier gas were accumulated over 50,000 laser shots; the data acquisition time was increased to 2-300,000 laser shots when Ne was used as the carrier gas. Background subtraction was performed in order to only observe signal relevant to the photodissociation of isobutene.

The molecular beam was characterized using a slotted chopper spinning at a 200 Hz. Characteristic beam velocities of about 1700 m/s were obtained in the present experiment using He as a seed gas. The corresponding speed ratio (beam flow velocity over velocity spread) was consistently in the range of 35-40. When using Ne as a carrier gas, typical beam velocities were 800 m/s with a speed ratio of 20.

4.3 Results

Figure 4.2 shows representative TOF data at m/z = 55 ($C_4H_7^+$), the parent ion for the C_4H_7 fragment that would be formed by H atom loss via channel (1). Three of these spectra were taken using He as the seeding gas, while the fourth, at Θ = 9°, was taken with Ne as the seed gas. Figure 4.3 shows spectra at m/z = 41 ($C_3H_5^+$) and m/z = 15 (CH_3^+), corresponding to the parent ions for channel 2. These spectra were taken with He as the seed gas. In all TOF spectra, open circles represent the data and the solid lines represent the simulated fit to the data obtained using forward convolution of assumed center-of-mass translational energy distributions (see Section 4.4). Many more TOF spectra were taken at various ion masses and angles. For example, Figure 4.4 shows several TOF spectra taken at m/z = 39 ($C_3H_3^+$) using Ne as a seed gas; these spectra are particularly useful for determining the product branching ratio as discussed in Section 4.4.

The TOF spectra for m/z = 55 (Figure 4.2, He and Ne seed gas) consist of a single peak whose intensity decreases with increasing laboratory angle from 4° to 13°. No signal was observed beyond 13°, the kinematic limit for H atom loss at 193 nm based on the appropriate Newton diagram. Hence, it appears that since we are only observing a single peak for m/z = 55 and that this peak disappears beyond 13°, we can attribute this feature

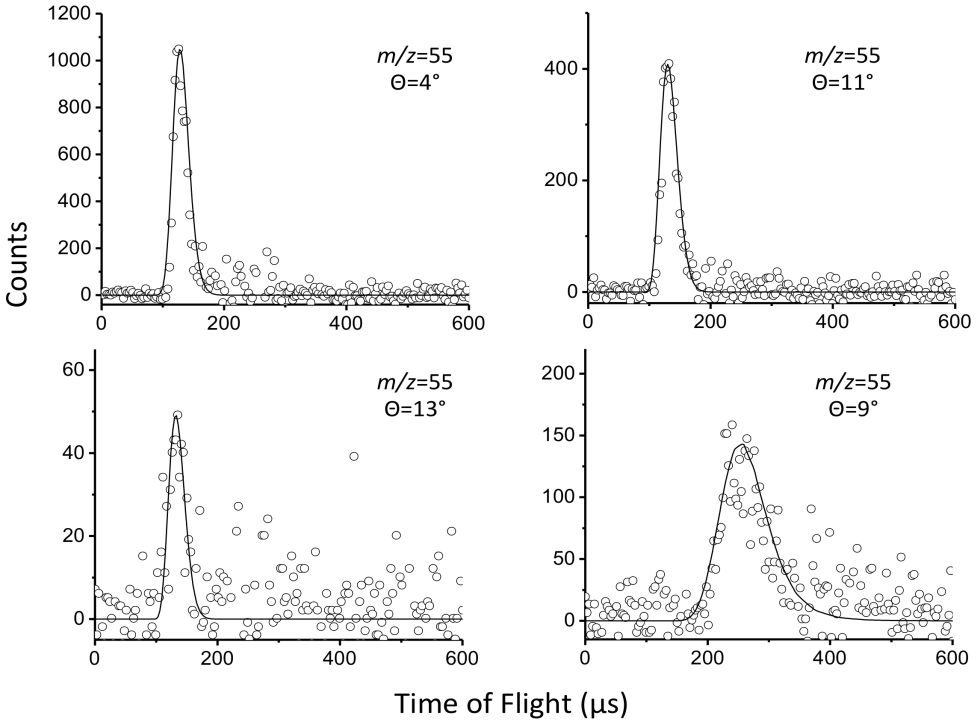

Fig. 4.2 TOF spectra for m/z = 55 ($C_4H_7^+$) fragments collected at Θ_{lab} = 4^0, 11^0 and 13^0 using He as a seeding gas and 9^0 using Ne obtained from 193 nm photodissociation of C_4H_8. The fits to these TOF spectra are generated from the P(E_T) distribution in Figure 4.5.

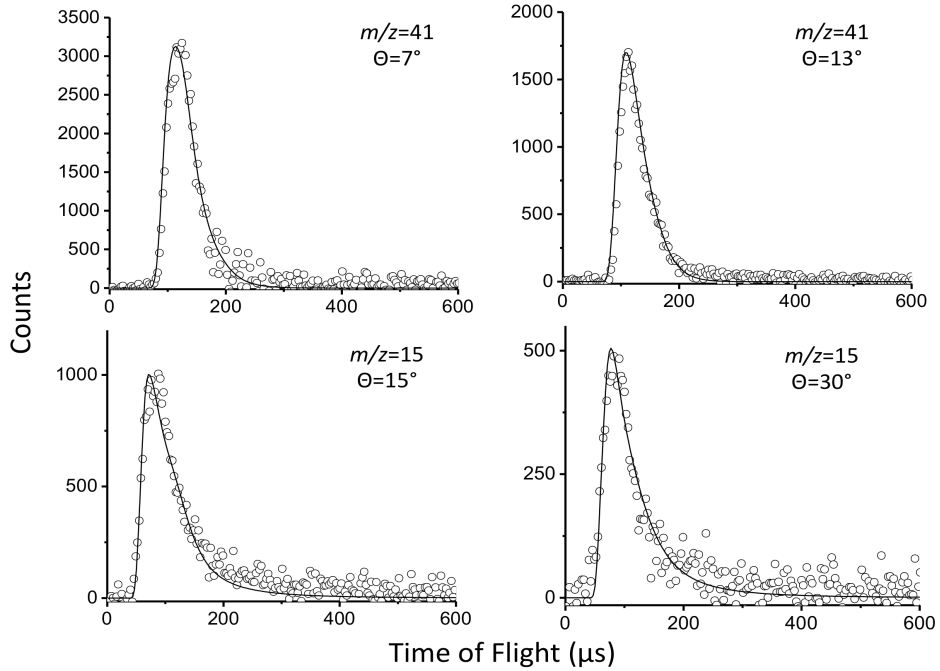

Fig. 4.3 TOF spectra for m/z = 41 ($C_3H_5^+$) and m/z = 15 (CH_3^+) fragments collected at Θ_{lab} = 7^0, 13^0 and Θ_{lab}= 15^0,30^0 respectively obtained from 193 nm photodissociation of isobutene(C_4H_8). A single P(E_T) distribution, shown in Figure 4.6, was used to fit these spectra.

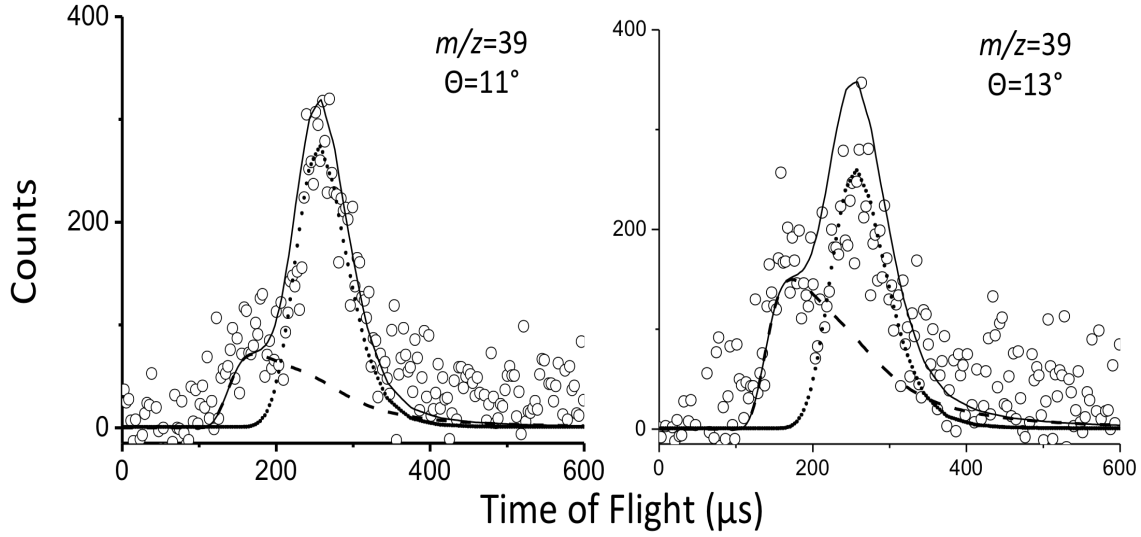

Fig. 4.4 Representative TOF spectra of m/z = 39 ($C_3H_3^+$) at laboratory angles of $\Theta_{lab} = 11^0$ and 13^0. The doted and dashed lines show simulated TOF spectra using the P(E_T) distributions in Figure 4.5 and 4.6 respectively. The solid line shows the sum of blue and red simulations.

to H atom loss from the isobutene molecule at 193 nm. While the m/z = 41 and 15 spectra in Figure 4.3 could, in principle, originate from dissociative ionization of the C_4H_7 fragment, these spectra extend over a much larger angular range, indicating they correspond to at least one additional photodissociation channel, with channel (2) as the likely candidate. The definitive assignment of these features is presented in Section 4.4.

4.4 Analysis

The data were analyzed by constructing photofragment center-of-mass translational energy and angular distributions P(E_T, θ) for all photodissociation channels and using these to simulate the laboratory-frame TOF spectra. For each channel, the overall distribution can be decoupled into a product of center-of-mass translational energy P(E_T) and angular distributions I(θ) as follows:

$$P(E_T, \theta) = P(E_T)I(\theta) \quad (4.3)$$

The TOF spectra were fit by forward convolution of center-of-mass energy and angular distributions using the PHOTRAN software package.[95] In our experimental geometry, an anisotropic angular distribution in the plane of detection can occur even with an unpolarized laser beam since the rotational axis of the detector is orthogonal to the plane defined by the molecular and the laser beam, but a satisfactory fit to all the data was obtained assuming an isotropic distribution. The entire set of TOF data could be fit using the P(E_T) distributions in Figures 4.5 and 4.6 for channels (1) and (2), respectively; the simulated spectra obtained from these distributions are shown as solid lines in Figures 4.2, 4.3, and 4.4.

From conservation of energy, the translational energy E_T, is given by:

$$E_T = h\nu + E_0 - E_{int} - D_0 \quad (4.4)$$

Here $h\nu$ is the photon energy at 193nm, D_0 the dissociation energy of a given photodissociation channel (from Equations 1 and 2), E_{int} is the internal energy of the photofragment and E_0 is the initial energy of the isobutene molecule. Hence, for a given photodissociation channel of cold molecules (i.e., E_0 = 0), the maximum translational energy E_{Tmax} is given by $h\nu$ - D_0, yielding values of 60 and 47 kcal/mol for channels (1) and (2), respectively, based on the energetics of Figure 4.1. This constraint was applied to the P(E_T) distributions used to fit the data; other than that, the point-wise distributions were adjusted freely to obtain the best simulation of the full data set.

The P(E_T) distribution for channel (1) in Figure 4.5 fits the entire set of TOF spectra at m/z = 55. The distribution peaks at 4 kcal/mol with an average translational energy, $\langle E_T \rangle$ = 11.1 kcal/mol, and extends up E_{Tmax}= 60 kcal/mol. The simulations are not particularly sensitive to products with E_T < 4 kcal/mol, a point covered further in Section 4.5, but the tail extending out to E_{Tmax} produces a better fit to our data than distributions with a lower energy cutoff .

Forward convolution of the P(E_T) distribution in Figure 4.6 shows that the TOF spectra for m/z = 41 and m/z = 15 in Figure 4.3 correspond to momentum-matched C_3H_5 and CH_3 photofragments from mass channel (2). The P(E_T) distribution for this channel peaks at 4 kcal/mol with an average translational energy of 5.1 kcal/mol and extends to up to 17

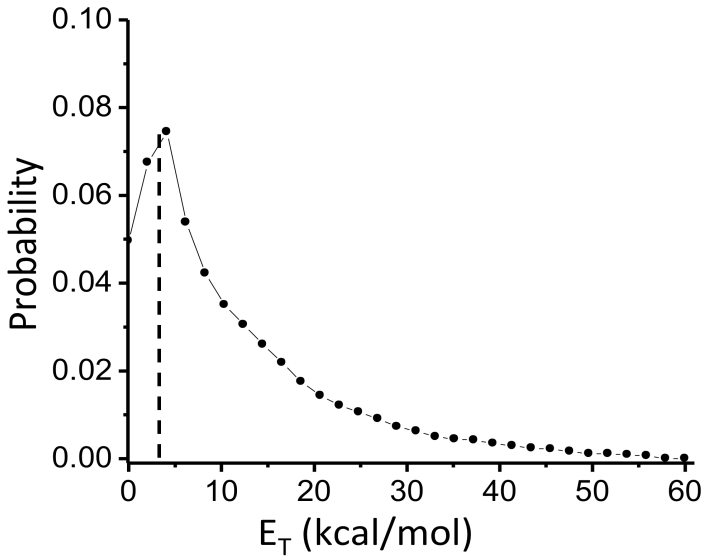

Fig. 4.5 Center-of-mass P(E_T) distribution from isobutene photodissociation at 193 nm to H+C_4H_7. The maximum available translational energy is 60 kcal/mol. Products with E_T < 4.5 kcal/mol can undergo secondary dissociation (see text).

kcal/mol. The P(E_T) distribution could be extended to E_{Tmax} (47 kcal/mol) without degrading the quality of the fit. The analysis shows that contributions to the TOF spectra in Figure 4.3 from dissociative ionization (from *m/z* = 41 and 55) are negligible. Figure 4.1 shows that that the primary product of the photodissociation of isobutene via a methyl loss can further isomerize via a 1,2-hydrogen shift to form the allyl radical,[49] a process considered further in Section 4.5.

The channel (2) : channel (1) branching ratio can be extracted from TOF spectra at ion masses where both channels contribute via dissociative ionization, such as the *m/z* = 39 spectra shown in Figure 4.4. The branching ratio is obtained from Equation 4.5

$$\frac{\mathrm{CH_3\ loss\ channel}}{\mathrm{H\ loss\ channel}} = R \times \frac{\sigma_{\mathrm{C4H_7}}}{\sigma_{\mathrm{C_3H_5}}} \times \frac{\mathrm{f_{C_4H_7}}}{\mathrm{f_{C_3H_5}}} \qquad (4.5)$$

Here, *R* describes the relative weight of the two P(E_T) distributions used to fit the experimental data for both channels in order to reproduce the relative intensity of each contribution of the H loss and CH_3 loss channel. The relative electron impact ionization cross section, σ_i , has been determined using the additivity method proposed by Fitch *et al.*[115] Finally *f* represents the fraction of a given photodissociation channel signal appearing at *m/z* = 39 via dissociative ionization. These fractions, 30% for the H loss channel and 49% for CH_3 loss, were determined by taking TOF spectra at $\Theta_{lab} = 9^0$ at all values of *m/z* that yield to a measurable signal (*m/z* = 55, 54, 53, 52, 51, 50, 49, 41, 40, 39, 38, 37, 36, 27, 26 and 25). Figure 4.4 shows two representative TOF spectra for *m/z* = 39 and indicates the simulated contributions of dissociative ionization from channels (1) and (2); the simulations are generated from the P(E_T) distributions in Figures 4.5 and 4.6. By optimizing *R* to generate the best agreement with the TOF spectra, we obtained a branching ratio of 1.7 (5) in favor of CH_3 loss. The main source of uncertainty for the branching ratio comes from the determination of *R* which may vary between 1.5 and 2.5 with best agreement found at 2.1.

Finally, electronic structure calculations were carried out to characterize the reaction coordinates for channels (1) and (2), i.e. C-H and C-C bond cleavage. The calculations were performed at the MP2/6-311+g(d,p) level of theory and basis set using the GAUSSIAN09[116] software package. The reaction coordinates were mapped out optimizing the geometry as either r_{CH} or r_{CC} was varied. Calculations were carried out to bond lengths as large as 3.8 Å for both bonds. The optimized bond lengths were found to be r_{CH} = 1.093Å and r_{CC} = 1.506Å at the equilibrium geometry. No exit barrier was found for either channel, as expected for simple bond cleavage. Calculated energies along the two reaction coordinates were scaled to match ΔH_0 of Equations 4.1 and 4.2; these scaled energies were used in the RRKM calculations. Harmonic vibrational frequencies were calculated for vibrational modes perpendicular to both reaction coordinates for use in RRKM rate constant calculations.

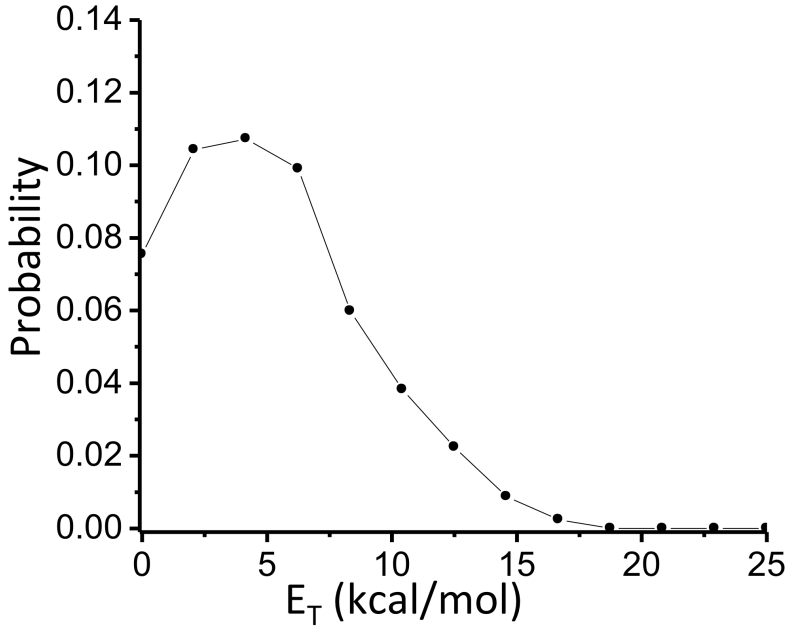

Fig. 4.6 Center-of-mass P(E_T) distribution from isobutene photodissociation at 193 nm to CH_3+C_3H_5. The maximum allowed translational energy is 47 kcal/mol.

4.5 Discussion

The preceding analysis shows that photodissociation of isobutene at 193 nm results in both H and CH_3 loss as primary photofragmentation channels. The P(E_T) distributions for both channels in Figures 4.5 and 4.6 peak at low kinetic energy. This result, in conjunction with our electronic structure calculations that show no exit barrier for either channel, suggests that the overall dissociation mechanism involves internal conversion to the ground state followed by statistical unimolecular decay to products. If this is the case, however, then we need to be able to explain why the CH_3 loss channel is favored even though it lies higher in energy by ~13 kcal/mol, assuming that the other fragment is the 2-propenyl radical. In the remainder of this section, we consider various aspects of the two channels in more detail and conclude by discussing calculations of the branching ratio using RRKM theory.

The P(E_T) distribution for channel (1) shown in Figure 4.5 peaks at 4 kcal/mol. However, as indicated in Figure 4.1, the 2-methylallyl radical formed via H atom loss can undergo further dissociation to CH_3 + C_3H_4; the calculated barrier for this process is 55.5 kcal/mol.[114] Any C_4H_7 fragments from channel 1 with internal energy exceeding this barrier height can undergo secondary dissociation. Since the H atom has no internal excitation, the C_4H_7 internal energy is given by E_{Tmax} - E_T, so fragments with E_T < 4.5 kcal/mol would have enough internal energy to dissociate. We found that a P(E_T) distribution truncated below 4.5 kcal/mol (shown as a dotted line in Figure 4.5) produced fits to our data at m/z = 55 that are indistinguishable from those generated from the

distribution in Figure 4.5, so we cannot claim to see clear evidence for secondary dissociation. However, if this process is occurring, it only affects a small part of the P(E_T) distribution and will not significantly alter the calculated branching ratio.

For channel (2), the C-C bond fission products are CH_3 +CH_3CCH_2, the 2-propenyl radical. As seen in Figure 4.1, this species lies 20.6 kcal/mol above the allyl radical,[49] and one must then consider the possible role of allyl in the dissociation dynamics. For example, it is possible for allyl to be formed directly from the dissociation of isobutene through a multi-center transition state, in which an H atom from the remaining CH_3 group transfers to the central C atom as the methyl fragment departs. Such a transition state typically results in a substantial exit barrier along the reaction coordinate which would then lead to a translational energy distribution peaking well away from $E_T = 0$, in contrast to the distribution in Figure 4.6. Hence concerted production of allyl seems unlikely.

It is also possible for 2-propenyl products formed with more than 45.4 kcal/mol internal energy to isomerize to allyl by a 1,2-hydrogen shift, according to the energetics in Figure 4.1. However, since E_{Tmax} for channel (2) is only 47 kcal/mol at 193 nm, this means that isomerization can only occur for dissociation events with E_T < 1.6 kcal/mol, which corresponds to a very small fraction of the P(E_T) distribution in Figure 4.6. Moreover, this value of E_T assumes no internal excitation of the CH_3 fragment. It thus appears that isomerization to allyl represents a very minor contribution to the overall dynamics and may not occur at all.

It thus appears that our channel (2) : channel (1) branching ratio of 1.7 (5) favors the higher energy C-C bond fission channel over C-H bond fission, a somewhat unexpected result at first glance. However, as discussed in previous work on isobutene kinetics,[107,108] the A-factor for CH_3 loss is higher than for H loss because CH_3 loss results in three more rotational degrees of freedom at the transition state than H loss. As a result, CH_3 loss should become faster than H loss at a sufficiently high temperature.

We have explored this effect from the perspective of our experiment by calculating microcanonical rate constants $k_i(E)$ for the two channels with RRKM theory,[52]

$$k_i(E) = \frac{W^*(E - E_{0)}}{h\rho(E)} \tag{4.6}$$

Here, W^* defines the total number of states of the critical configuration, E_0 is the energy of the transition state, and ρ(E) denotes the density of states of the reactant at total energy E. The density and sum of states were calculated by direct state-count method using the Beyer-Swinehart algorithm,[117,118] using vibrational frequencies obtained from the electronic structure calculations described in Section 4.4. Vibrational frequencies for all modes perpendicular to the reaction coordinate were calculated for both bond fission channels. For r_{CC} > 2.6 Å, we treated torsional motion of the methyl group as a one-dimensional free rotor with a rotational constant of around 5 cm^{-1}.

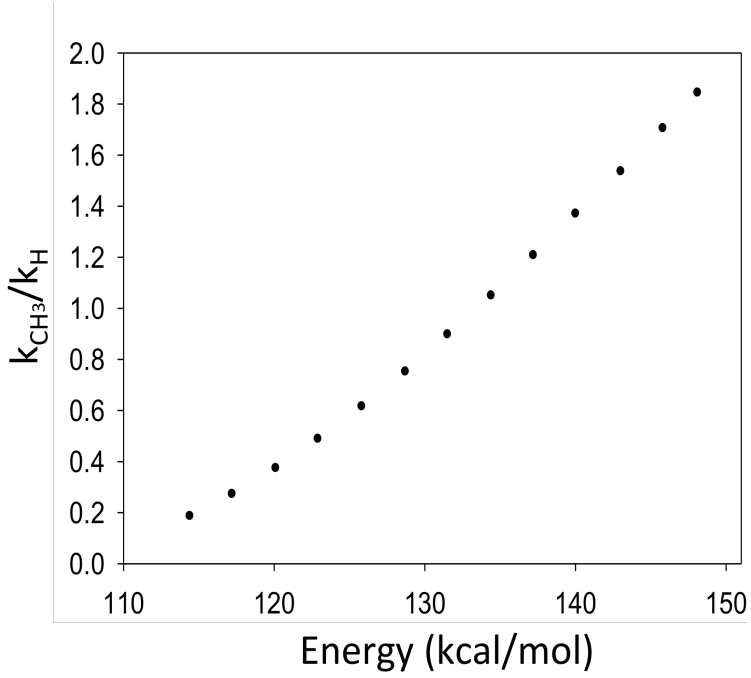

Fig. 4.7 Evolution of the rate constant ratio calculated using RRKM theory between the CH_3loss channel and the H loss channel at fragment separation of 3.4 Å as a function of energy.

By looking at the evolution of the calculated rate constants for both channels as a function of fragment separation, we found minimum values of the rate constants for channels (1) and (2) at r_{CH} = 3.4 Å and r_{CC} = 3.4 Å, respectively. These values were k_{CH3} = 1.55 x 10^8 Hz and k_H = 8.42 x 10^7 Hz, leading to a theoretical branching ratio of CH_3 loss : H loss = 1.8, in remarkably close agreement with experiment. We also calculated the branching ratio as a function of excitation energy at these two transition state geometries as shown in Figure 4.7. At 193 nm excitation (148 kcal/mol), methyl loss dominates over hydrogen atom loss. However, the H loss channel becomes more important with decreasing photon energy (i.e. increasing wavelength) to become the dominant channel at about 133 kcal/mol (215 nm), which is below the 205 nm onset[110] of the isobutene UV absorption spectrum. In any case, our RRKM results are certainly consistent with the arguments put forth in kinetics papers regarding the A-factors for the two bond fission channels and suggest that both channels should be considered when constructing kinetic models for isobutene pyrolysis and oxidation.

4.6 Conclusions

We have investigated the photodissociation dynamics of the isobutene molecule at 193 nm using photofragment translational spectroscopy. The translational energy distribution and the product branching ratio between H and CH_3 loss were obtained. The translational energy distributions indicated that both channels take place via statistical dissociation on the ground state potential energy surface. The branching ratio between both channels was

determined experimentally to be 1.7(5) in favour of the higher energy CH_3 loss channel. Electronic structure calculations combined with RRKM theory showed that such a result is consistent with statistical dissociation at the excitation energy used in our experiment.

4.7 Acknowledgments

This work was supported by the Director, Office of Basic Energy Sciences, Chemical Sciences Division of the U.S. Department of Energy under Contract No. DE-AC02-05CH11231.

Chapter 5

Photodissociation Dynamics of the Phenyl Radical Via Photofragment Translational Spectroscopy

Photofragment translational spectroscopy (PTS) was used to study the photodissociation dynamics of the phenyl radical, C_6H_5, at 248 and 193 nm. At 248 nm, the only dissociation products observed were from H atom loss, attributed primarily to H + *o*-C_6H_4 (*ortho*-benzyne). The observed translational energy distribution was consistent with statistical decay on the ground state surface. At 193 nm, dissociation to H + C_6H_4 and C_4H_3 + C_2H_2 was observed. The C_6H_4 fragment can be either *o*-C_6H_4 or *l*-C_6H_4 resulting from decyclization of the phenyl ring. The C_4H_3 + C_2H_2 products dominate over the two H loss channels. Attempts to reproduce the observed branching ratio by assuming ground state dynamics were unsuccessful. However, these calculations assumed that the C_4H_3 fragment was *n*-C_4H_3, and better agreement would be expected if the lower energy *i*-C_4H_3 + C_2H_2 channel were included.

5.1 Introduction

The phenyl radical, *c*-C_6H_5, plays a central part in the combustion chemistry of aromatic hydrocarbons. Its formation from the bimolecular reaction of smaller aliphatic species has been proposed to be the rate-limiting step in the production of larger aromatic molecules.[119,120] During combustion, the phenyl radical can undergo oxidation to form phenyl peroxy and phenoxy radicals.[121] Phenyl can also polymerize to form polycyclic aromatic hydrocarbons,[122] or it can decompose. The phenyl peroxy radicals are very

reactive species that can further react with other hydrocarbons, while polycyclic aromatic hydrocarbons can further polymerize and lead to soot formation. The phenyl radical is an intermediate in the thermal decomposition of benzene,[123] so its bimolecular reactivity and unimolecular decay kinetics are of considerable interest in formulating a complete mechanism for this process. These considerations motivate the work described herein, in which the collisionless photodissociation decay dynamics of phenyl are investigated using photofragment translational spectroscopy.

Interest in the phenyl radical as a combustion intermediate dates back to the shock tube study by Bauer[123] in 1963 where phenyl was observed as an intermediate in the thermal decomposition of benzene. Subsequent shock-tube studies on benzene decomposition[124,125] confirmed the role of phenyl as an intermediate. Collisionless photodissociation studies of benzene at 193 nm showed phenyl to be the major photoproduct.[126]

Solution phase kinetics of the phenyl radical with multiple substrates were examined by Scaiano and Stewart.[127] Gas phase bimolecular reactions of phenyl with various hydrocarbons have been investigated in a series of kinetics experiments by Lin and co-workers,[128,129,130] in which phenyl radicals were produced by pulsed laser photolysis and rate constants were determined by mass spectrometry and cavity ring-down spectroscopy. Cavity ring-down spectroscopy was also used by Tonokura *et al.*[131] to investigate phenyl radical reactions with Cl, O_2, and Cl_2. Kaiser and co-workers[132,133] have carried out more detailed dynamics studies of phenyl bimolecular chemistry in a series of crossed molecular beams experiments where product kinetic energy and angular distributions were determined.

The spectroscopy of the phenyl radical has been investigated in several laboratories. The ultraviolet absorption spectrum of phenyl was measured in the gas phase by Ikeda *et al.*[134] and in an Ar matrix by Radziszewski *et al.*[135] The resulting electronic bands have been assigned and simulated in theoretical work.[136,137] The high resolution infrared spectrum of phenyl was reported by Sharp *et al.*[138] The photoelectron spectrum of the phenyl radical[139,140] and phenide anion[141] have yielded the ionization potential and electron affinity of phenyl, while Sveum *et al.*[142] determined its photoionization cross section. The geometry, vibrational frequencies, and electron affinity of phenyl have also been investigated with electronic structure calculations.[143]

The work described in this paper is motivated by previous theoretical and experimental studies of the unimolecular decay of the phenyl radical. The relevant potential energy diagram, adapted from a calculation by Madden *et al.*[144] is shown in Figure 5.1, and shows three low-lying decay channels:

1) $c\text{-}C_6H_5 \rightarrow o\text{-}C_6H_4 + H$ ΔH_0=76.0 kcal/mol (5.1)

2) $c\text{-}C_6H_5 \rightarrow l\text{-}C_6H_5 \rightarrow n\text{-}C_4H_3 + C_2H_2$ ΔH_0=98.2 kcal/mol (5.2)

3) $c\text{-}C_6H_5 \rightarrow l\text{-}C_6H_5 \rightarrow l\text{-}C_6H_4 + H$ ΔH_0=91.0 kcal/mol (5.3)

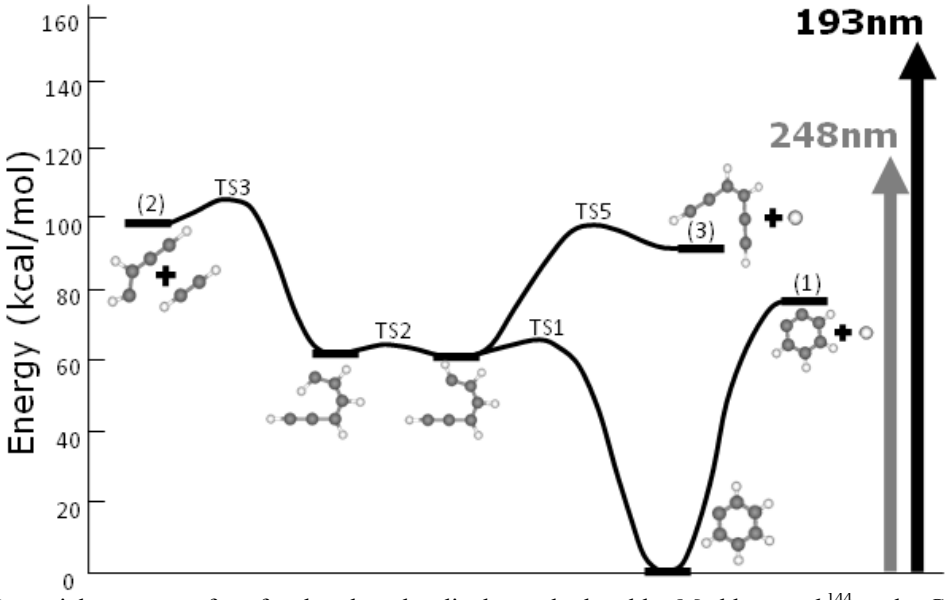

Fig. 5.1 Potential energy surface for the phenyl radical as calculated by Madden *et al.*[144] at the G2M level of theory. The asymptotic channels 1, 2, and 3 are indicated.

These energetics are very similar to those reported recently by Lories *et al.*[145]

Channel (1), the lowest energy channel, involves simple C—H bond fission to form *ortho*-benzyne, whereas channels (2) and (3) involve ring opening as the reaction proceeds over TS1 (decyclization) followed by either C—C or C—H bond fission. Early theoretical work[146,147] that focused on phenyl radical formation and dissociation focused only on channel (2) and did not consider H atom loss via channel (1). Experiments performed on the pyrolysis of benzene and chlorobenzene[148] were interpreted in the context of these earlier studies; the H atom signal observed in this work was attributed to further dissociation of the C_4H_3 fragment produced by channel (2). However, theoretical work by Madden *et al.*[144] and Wang *et al.*[149] has questioned these conclusions, since the earlier studies did not take into account that both fragmentation barriers for linear C_6H_5, depicted in Figure 5.1, are higher in energy than the recyclization barrier, and that the energy required for *o*-C_6H_5 + H formation is substantially smaller than for *n*-C_4H_3 +C_2H_2 formation. These calculations raise the issue of the competition between H + *o*-benzyne channel, which can occur via simple C—H bond fission, with the two decay channels that ensue upon decyclization. Rate constants as a function of energy calculated by Madden indicate that the H + *o*-benzyne channel dominates at low energy, but that the other channels become progressively more important with increasing energy. Work by Wang indicated that tighter transition states for H atom loss than that used by Madden are needed to model shock tube data. Experiments by Tseng and co-workers[150] found that 10% of the phenyl radicals formed from the photodissociation of C_6H_5NO at 193 nm further decomposed into H + benzyne, thus providing direct evidence for the importance of this channel.

In order to more directly address the above issues regarding unimolecular decay of the phenyl radical, we have investigated the collisionless decomposition dynamics of the phenyl radical using photofragment translational spectroscopy[91] at 248 and 193 nm in order to characterize the primary photochemistry of phenyl. Following the assignments of Kim *et al.,*[136] excitation at 248 nm accesses the 1^2B_2 and 3^2A_1 states via π-π^* transitions, while at 193 nm, the 2^2B_2 state is accessed by a stronger π-*n* transition, populating the σ orbital at the site of the missing H atom in phenyl. At 248 nm, only H atom loss was observed, but at 193 nm, channel (2) was also seen and, somewhat unexpectedly, was found to dominate over H atom loss.

5.2 Experiment

The work presented here was performed on a molecular beam photodissociation apparatus with a fixed source and a rotatable detector in which photodissociation products were analyzed with electron impact ionization mass spectrometry. Details of our detection scheme are sketched in Figure 5.2 and have been described previously.[10,24] Phenyl radicals were produced with a newly built flash pyrolysis source following the design of Kohn *et al.*[151] A piezo-activated valve was used to produce a pulsed nitrosobenzene (C_6H_5NO) beam seeded in helium. A mixture of 0.2% C_6H_5NO was obtained by flowing 4 atm of He over a solid sample of nitrosobenzene at room temperature and applying 1 atm of this mixture to the pulsed valve with a vacuum regulator. The phenyl radical beam was generated via pyrolysis of the nitrosobenzene beam within a resistively heated SiC tube. This pyrolytic source is shown in Figure 5.2 and consists of a SiC tube supported by a pair of molybdenum electrodes attached to the pulsed valve by a water-cooled copper block and an electrically-insulating alumina spacer.

The phenyl radical beam was collimated by two skimmers that separated the source chamber from the main chamber. Within the main chamber, the radical beam was crossed at 90^0 with the 2 x 4 mm^2 focused beam spot of the photodissociation laser. Pulse energies of 40 mJ were obtained from a GAM excimer laser at 248 nm or a Lambda-Physik excimer laser at 193 nm. The scattered photofragments were detected as a function of laboratory angle, Θ, in the plane defined by the molecular beam and laser beam. After entering the triply differentially pumped detector, the neutral photofragments were ionized by electron impact, mass selected with a quadrupole mass filter, and detected with a Daly style ion detector. The acquired time of flight (TOF) spectra consisted of ion counts as a function of time and were obtained with using a multichannel scaler interfaced to a computer. Each spectrum shown was accumulated over 300-500,000 laser shots at a laser repetition rate of 100 Hz. The pulsed valve, however, was operated at 200 Hz so that background subtraction could be performed. An iterative forward convolution method was used to simulate the TOF spectra and thus determine the photofragment translational energy distributions in the center-of-mass frame of reference.

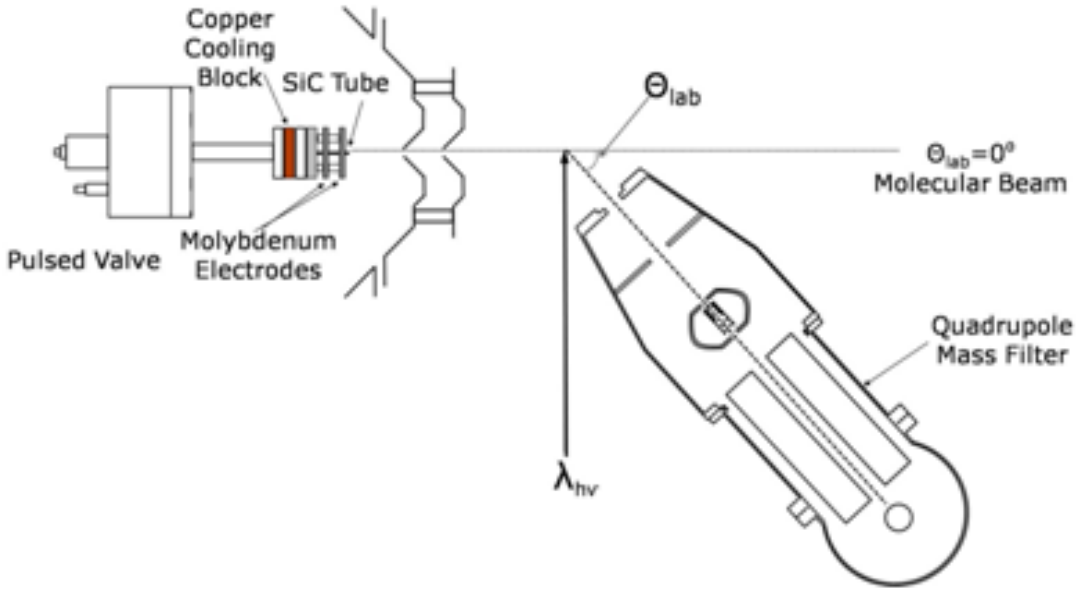

Fig. 5.2 Schematic of apparatus, showing the radical source, photodissociation laser, and rotating mass spectrometer detector.

The radical beam was characterized using a spinning, retractable slotted chopper disk. Beam velocities were typically ~2200 m/s. The speed ratio, defined as the ratio between the beam flow velocity and velocity spread, is in the range of 4 to 6. Mass spectra of the molecular beam taken with the SiC tube unheated and subsequently heated to a temperature of about 1700^{O}C are shown in Figure 5.3. There is significant dissociative ionization(DI) induced by electron impact ionization. Signal at *m/z* = 77 corresponding to $C_6H_5^+$ is seen even from the unheated source, presumably from DI of nitrosobenzene. The phenyl photodissociation experiments were conducted by passing the minimum current through the SiC tube needed to eliminate fully the nitrosobenzene parent ion signal at *m/z* = 107. Under these operating conditions, the *m/z* = 77 signal in the bottom trace should be from the phenyl radical; this assumption was tested experimentally as discussed in Section 5.3.

5.3 Results

TOF spectra were taken for *m/z = 76* ($C_6H_4^+$), *m/z* = 51 ($C_4H_3^+$), and *m/z = 26* ($C_2H_2^+$), the ionized primary fragments for channels (1)-(3), and for several of the daughter ions formed by dissociative ionization in the electron impact ionizer. Figure 5.4 shows TOF spectra of the *m/z* = 76 signal obtained from 248 and 193 nm photodissociation collected at laboratory scattering angles Θ ranging from 3°-8°. Figure 5.5 shows the TOF spectra for the *m/z* = 51 and *m/z* = 26 photofragments at Θ = 9°-15°. Figure 5.6 shows TOF

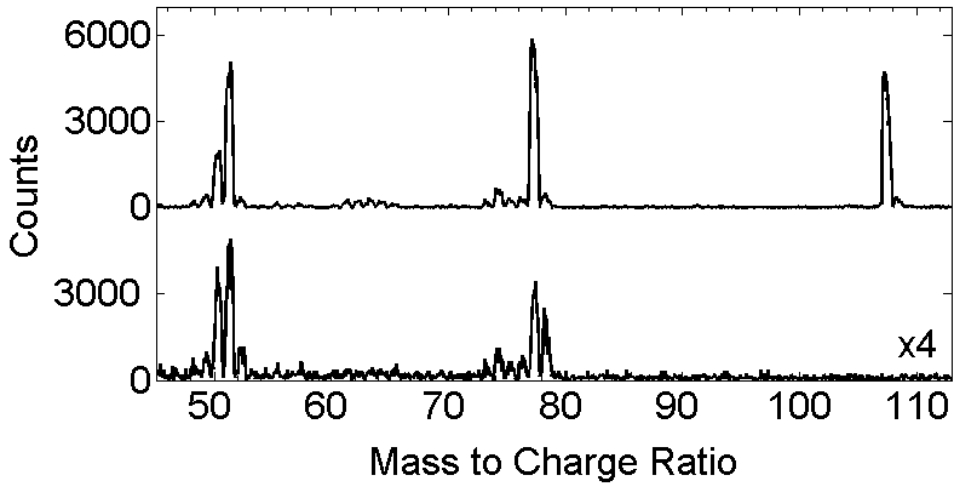

Fig. 5.3 Mass spectra of the molecular beam of nitrosobenzene in helium taken with the pyrolytic source unheated in the upper trace and heated in the lower trace.

spectra taken at 193 nm for Θ = 6-8° at *m/z* = 50; these spectra were used to obtain product branching ratios as described in Section 5.4. In these figures, the TOF data are represented with open circles, while simulations obtained via forward convolution (see Section 5.4) are represented with solid lines. All spectra are background-subtracted as described above. TOF spectra were not collected for *m/z* = 1 owing to kinematic factors that cause this signal to be very low, along with high background at this mass-to-charge ratio.

Fragments with *m/z* = 76 were observed at both photodissociation wavelengths but only over a very narrow range of laboratory scattering angles near the molecular beam. The observed angular range is larger at 193 nm, reflecting more translational energy release at the higher photon energy. This signal was also more intense at 193 nm than at 248 nm, consistent with the larger phenyl absorption cross section at 193 nm.[135] TOF signal for the lighter masses (*m/z* = 51, 26) was considerably weaker, and signal at angles $\Theta \geq 9^0$ was seen only at 193 nm.

The raw TOF data suggest the presence of H atom loss at both wavelengths and channel (2) at 193 nm only, but several checks are required to confirm this assignment. For example, a possible concern in this experiment is that photodissociation of any benzene or nitrosobenzene in the beam will produce C_6H_5 and C_6H_4 photofragments, thereby interfering with C_6H_4 photofragments created from phenyl photodissociation. Nitrosobenzene photodissociation studies[150] at both 248 and 193 nm show the presence of only one dissociation channel, the production of C_6H_5 and NO. To check for this channel, we looked for photodissociation signal at *m/z* = 77 ($C_6H_5^+$). These spectra did not show distinguishable signal at 248 or 193 nm, consistent with complete decomposition of the parent compound in the pyrolysis source. At 193 nm, the major benzene photodissociation channel is phenyl + H.[126] The absence of signal at *m/z* = 77 rules out contamination from benzene at this wavelength. At 248 nm, benzene

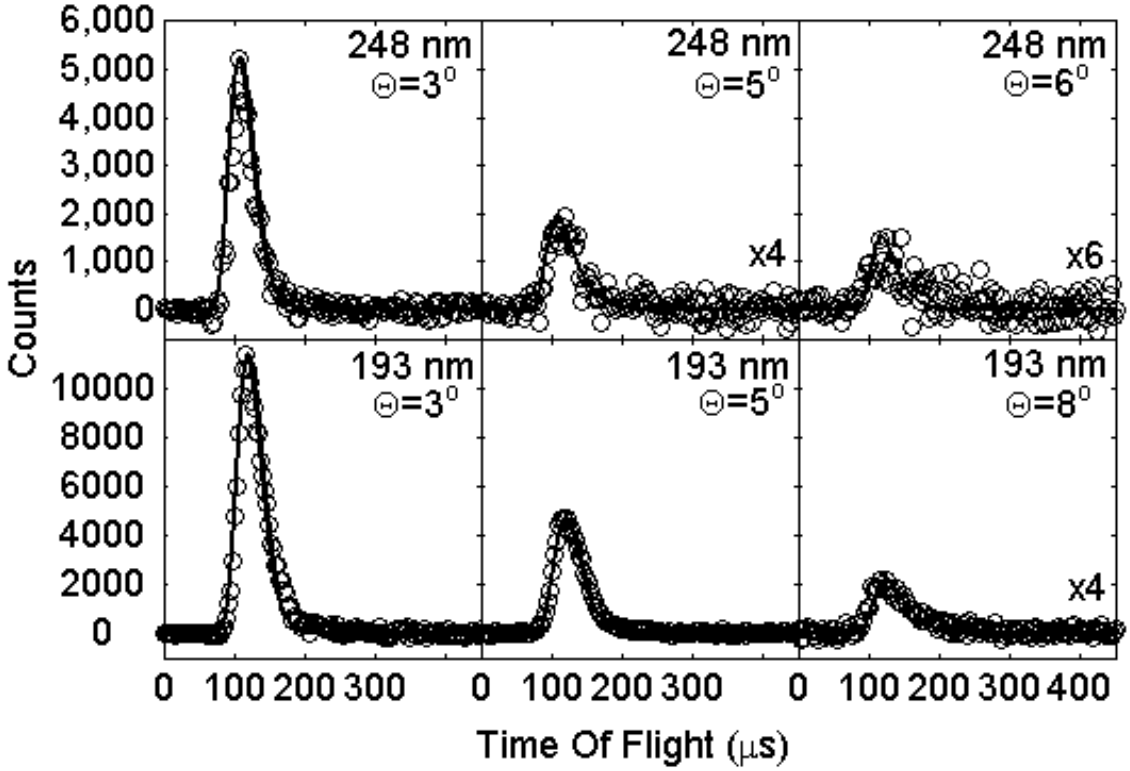

Fig. 5.4 Characteristic TOF spectra for m/z = 76 ($C_6H_4^+$) fragments collected at Θ_{lab} = 3^0, 5^0, 6^0, and 8^0 obtained from 248 and 193 nm photodissociation of c-C_6H_5. The fits to these TOF spectra (solid lines) are generated from the P(E_T) distributions in Figures 5.8 and 5.9, respectively.

dissociates to C_6H_4 + H_2, which could interfere with the m/z = 76 signal from phenyl photodissociation. To check for this, TOF data were simulated with the previously published translational energy distribution for this channel.[126] This procedure yielded significantly faster C_6H_4 photoproducts than were seen in our experiment. Hence, we can rule out interference from benzene at both wavelengths.

The assignment of the TOF features to phenyl dissociation must also be consistent with the photodissociation kinematics, as outlined in the Newton diagram in Figure 5.7 for 193 nm excitation. Each circle represents the maximum speed in the center-of-mass frame for the detected fragments produced from radical photodissociation. From the measured phenyl beam velocity, the maximum laboratory angle for a particular channel can then be determined from the diagram. The solid black circles correspond to C_6H_4 fragments from channel (1) and channel (3); the small diameter of these circles reflect the large mass ratio of the fragments for these channels (76:1) and results in a very restricted range of laboratory angles over which C_6H_4 product can be observed from phenyl dissociation. The fact that the experimental TOF signal for m/z = 76 ions falls within these limits here as well as within the corresponding limits at 248 nm supports our attribution of this signal to phenyl photodissociation.

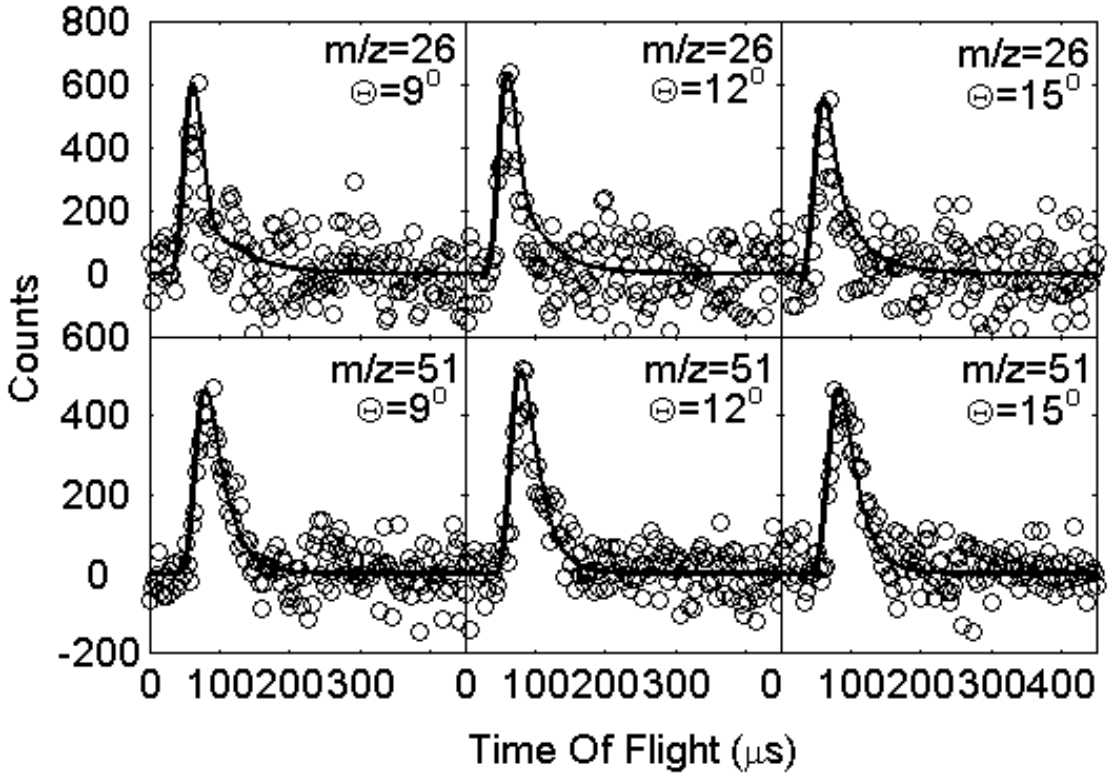

Fig. 5.5 Characteristic TOF spectra for m/z = 51($C_4H_3^+$) and m/z = 26($C_2H_2^+$) fragments collected at Θ_{lab} = 9^0, 12^0, and 15^0 obtained from 193 nm photodissociation of *c*-C_6H_5. A single P(E_T) distribution, shown in Figure 5.10, was used to simulate these spectra.

The dotted black circle on Figure 5.7 represents the C_4H_3 product from channel (2) at 193 nm; the corresponding circle for its C_2H_2 counterpart is much larger and is not shown. The Newton circles for both products are considerably larger than that for C_6H_4. As a result, these fragments can be observed over a larger spread of laboratory angles, consistent with the data in Figure 5.5. These kinematic considerations rule out dissociative ionization of C_6H_4 as the source of the signal at m/z = 51 and 26 in Figure 5.5, since the laboratory angles at which these data were taken lie beyond the maximum laboratory scattering angle of C_6H_4.The other key kinematic consideration is that if the m/z = 51 and 26 signals come from phenyl dissociation, they should be "momentum-matched", i.e. their TOF distributions should be reproduced from the same center-of-mass translational energy distribution. This point is considered further in the next section.

5.4 Analysis

The above results show that there are at least two phenyl photodissociation channels present: H atom loss at both wavelengths and, at 193 nm, an additional channel involving fragmentation to two heavy fragments. Center-of-mass photofragment energy

and angular distributions, $P(E_T,\theta)$, for each of these reaction channels were obtained by fitting the TOF spectra of the photodissociated fragments. The $P(E_T,\theta)$ distribution can be rewritten in terms of the uncoupled center-of-mass translational energy $P(E_T)$ and angular distribution $I(\theta,E_T)$:

$$P(E_T,\theta) = P(E_T)I(\theta,E_T) \tag{5.4}$$

In our experimental geometry, where the rotational axis of the detector is normal to the plane defined by the molecular and laser beams, an anisotropic angular distribution is possible even with unpolarized excimer laser beams, but a satisfactory fit to the data was obtained assuming an isotropic distribution for all values of E_T. The PHOTRAN[95] forward convolution program was used to simulate TOF spectra for all the data sets according to an assumed $P(E_T)$ distribution. The input $P(E_T)$ distribution for a channel was adjusted point-wise until a best fit was simultaneously obtained for all the TOF spectra of that channel. By conservation of energy, the total center-of-mass translational energy, E_T, is given by Equation 5.5,

$$E_T = h\upsilon + E_0 - E_{int} - D_0. \tag{5.5}$$

Here $h\upsilon$ is the photon energy, D_0 is the dissociation energy for the channel of interest (from Equations 5.1-5.3), E_{int} is the total internal energy of the fragments, and E_0 is the initial energy of the phenyl radicals. The maximum translational energy for a particular channel for cold radicals ($E_0 = 0$) is given by $h\upsilon - D_0$.

The best simulations obtained for the H loss channel at 248 nm are superimposed on the TOF spectra from Figure 5.4. The $P(E_T)$ distribution in Figure 5.8 used to simulate these

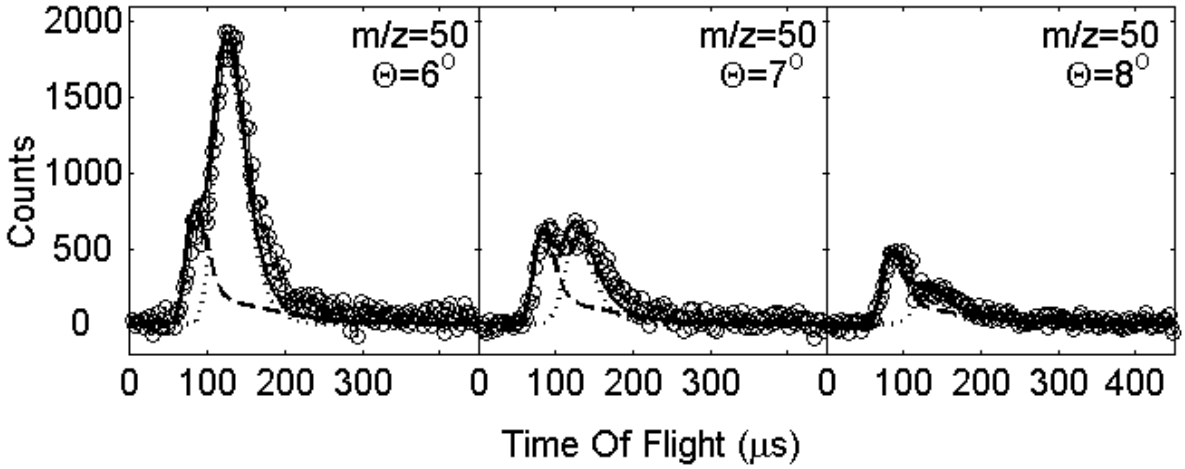

Fig. 5.6 TOF spectra of m/z = 50 ($C_4H_2^+$) at 193 nm showing contributions from daughter ions of mass 76 and mass 51 fragments. In each spectrum, these contributions are fit, respectively, with a dotted line using the $P(E_T)$ distribution in Figure 5.9 and a dashed line using the $P(E_T)$ distribution in Figure 5.10. The solid black line shows the sum of the dashed and dotted simulations.

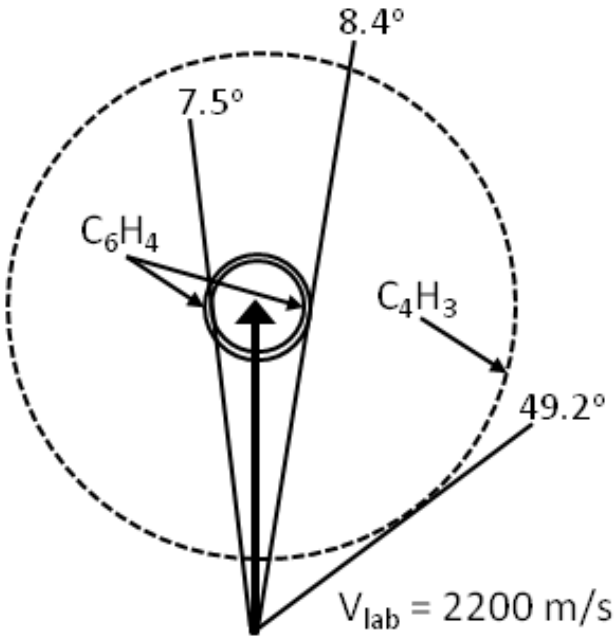

Fig. 5.7 Newton diagram for the phenyl radical photodissociation at 193 nm. Each circle represents the maximum center-of-mass speeds of product photofragments. The solid black circles represent the C_6H_4 fragments, while the dotted circle represents the *n*-C_4H_3 fragment. Maximum laboratory scattering angles for the fragments are shown.

TOF spectra peaks close to 0 kcal/mol, with an average translational energy $\langle E_T \rangle$ = 9 kcal/mol, and extends to 37 kcal/mol, the maximum translational energy available for channel (1). The P(E_T) distribution that fits the H loss channel from 193 nm photodissociation is shown in Figure 5.9. The corresponding TOF simulations are superimposed on the data in Figure 5.4. For this distribution, $\langle E_T \rangle$ = 16 kcal/mol. It also extends to the maximum allowed translational energy for channel (1), 72 kcal/mol, otherwise its overall form is similar to that in Figure 5.8. Note that channel (3) can contribute to H atom loss at both wavelengths; this channel would result in slower products that would be difficult to distinguish from channel (1). However, if we attempted to simulate the TOF spectra at either wavelength with a P(E_T) distribution that extended only to the maximum energy allowed for channel (3), i.e. 22 kcal/mol at 248 nm and 57 kcal/mol at 193 nm, the fit was noticeably poorer near the largest scattering angles where signal at *m/z* = 76 was observed.

The TOF spectra in Figure 5.5 for *m/z* = 51 and 26 can be fit with the P(E_T) distribution shown in Figure 5.10; the simulated TOF spectra are superimposed on the data in Figure 5.5. Since the TOF spectra for the two ion masses are reproduced with only a single P(E_T) distribution, these spectra are assigned to momentum-matched C_4H_3 and C_2H_2 photofragments from phenyl dissociation at 193 nm. The P(E_T) distribution in Figure 5.10 peaks at 8 kcal/mol with an average translational energy of $\langle E_T \rangle$ = 13 kcal/mol, and extends to 50 kcal/mol, the maximum allowed translational energy at this dissociation wavelength.

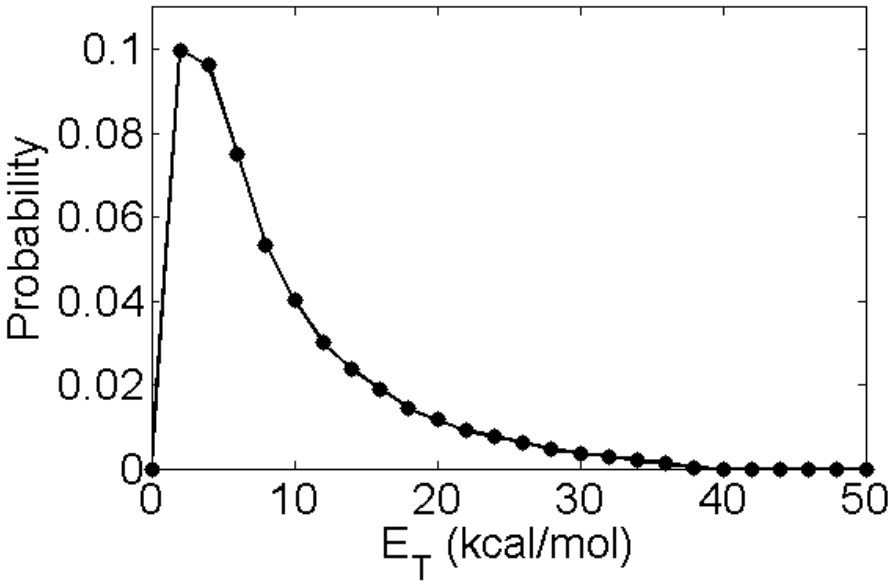

Fig. 5.8 Center-of-mass P(E_T) distribution from phenyl photodissociation at 248 nm to H + C_6H_4. The maximum available translational energy assumed for channel (1) is set at 37 kcal/mol. Due to the minimum laboratory detection angle of 3^0 for the current experimental setup, points below 5 kcal/mol are less reliable than those at higher energy.

All TOF spectra at 248 nm were fit with the P(E_T) distribution in Figure 5.8, while those at 193 nm were fit using one or, in the case of Figure 5.6, both of the P(E_T) distributions in Figures 5.9 and 5.10. Hence, there is no evidence for any primary photoproducts other than those associated with H atom loss and channel (2).

The universal detection scheme used in this experiment enables extraction of the branching ratio for channels (1) and (2) at 193 nm.

$$\frac{channel\ (2)}{channel(1+3)} = R \times \frac{\sigma_{C_6H_4}}{\sigma_{C_4H_3}} \times \frac{f_{C_6H_4}}{f_{C_4H_3}} \qquad (5.6)$$

The ratio R represents the relative weights of the P(E_T) distributions used by the fitting program to reproduce the relative intensities of contributions of H atom loss and channel (2) to the TOF spectra shown in Figure 5.6. The values of σ denote the relative electron impact cross sections of the C_6H_4 and C_4H_3 photofragments determined by the additivity scheme of Fitch and Sauter[115] while f is the fraction of channel (1) (or channel 2) signal appearing at m/z = 50 via dissociative ionization. These fractions, 56 % for channel (1)

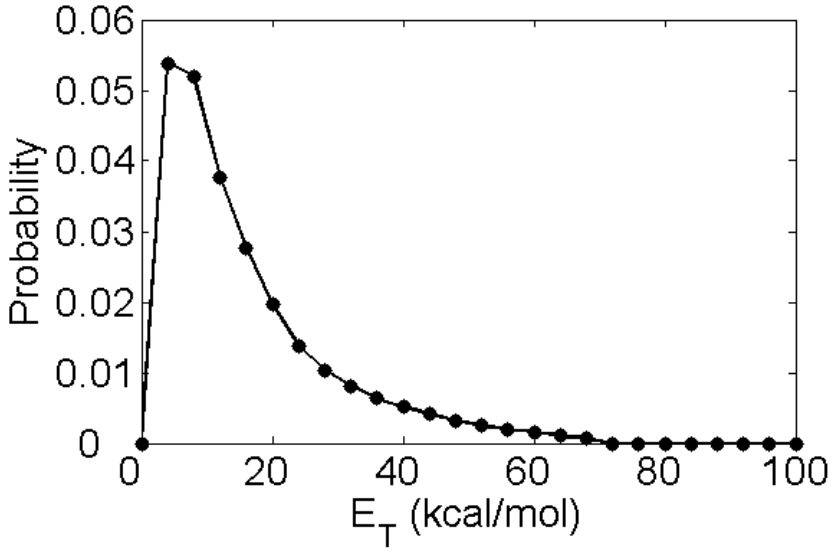

Fig. 5.9 Center-of-mass P(E_T) distribution from phenyl photodissociation at 193 nm to form H + C_6H_4. The maximum available translational energy assumed for channel (1) is set at 72 kcal/mol. Due to the minimum laboratory detection angle of 3^0 for the current experimental setup, points below 5 kcal/mol are less reliable than those at higher energy.

and 43% for channel (2), were determined by taking TOF spectra at $\Theta = 4°$ and 12° at all values of *m/z* that yielded measurable photodissociation signal (*m/z* = 76, 75,74,73,61,60,51,50,49,48,37, and 36). The channel (2)/channel(1+3) branching ratio was thus found to be 5.3 ± 0.8; estimated error bars are from Schmoltner.[96]

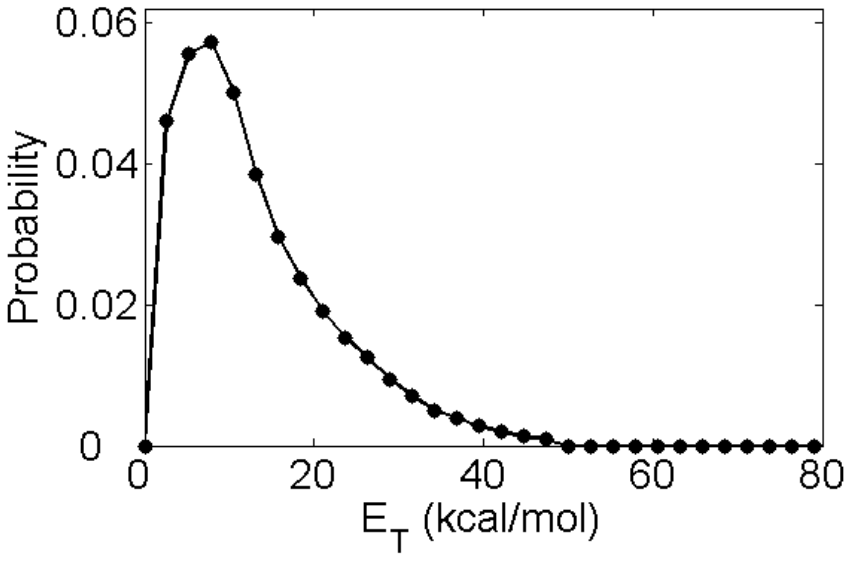

Fig. 5.10 Center-of-mass P(E_T) distribution for the C_4H_3+ C_2H_2 channel shown in Figure 5.6. This distribution was used to fit the TOF spectra for both *m/z* = 51 and 26. The maximum allowed translational energy is set at 50 kcal/mol.

5.5 Discussion

The main objectives of this study are to (a) determine the primary photochemistry of the phenyl radical and (b) to gain insight into the overall photodissociation mechanism. The key mechanistic question is whether dissociation occurs on one or more excited state surfaces or by internal conversion to the ground state followed by statistical decay. This issue can be addressed by considering the translational and angular energy distributions of the various product channels as well as the product branching ratios, and determining if these attributes are consistent with statistical decay on the ground state surface.

The unimolecular decomposition pathways of the phenyl radical on its ground state as determined by the electronic structure calculations by Madden *et al.*[144] are shown in Figure 5.1. On this surface, the lowest energy dissociation channel, channel (1), proceeds via C—H bond cleavage with no exit barrier. The higher energy channels (2) and (3) involve decyclization of phenyl via TS1 and dissociation over TS3 and TS5, respectively; the calculated barrier heights of TS3 and TS5 with respect to the associated product channels are 7.4 and 6.0 kcal/mol. If dissociation does occur on the ground state surface, one would expect channel (1) to dominate at low excitation energies, while channels (2) and (3) would become progressively more important at higher excitation energies. Moreover, based on the calculated topography of the ground state surface, ground state dissociation would result in a P(E_T) distribution for channel (1) peaking at very low E_T, while the distributions for channels (2) and (3) would peak at higher kinetic energies owing to the small exit barriers for both channels.

These expectations are largely borne out by the experimental data. At 248 nm, only H-atom loss is observed. The P(E_T) distribution for this channel peaks below 5 kcal/mol; C_6H_4 fragments with lower kinetic energy cannot be seen beyond the minimum laboratory scattering angle (3°) at which we can collect data. In contrast, in the photodissociation of comparably sized polyatomic molecules that undergo H atom loss on an excited state surface, the kinetic energy distributions peak much closer to the maximum allowed value.[152] Overall, the P(E_T) distribution in Figure 5.8 and the associated isotropic angular distribution are consistent with ground state dissociation. Assuming this to be the case, elementary considerations of statistical unimolecular decay would predict that channel (1) will dominate at this wavelength, even though channel (3) is accessible and cannot be easily distinguished from channel (1) in our data. We have performed a more quantitative analysis of the branching between channels (1) and (3) using the microcanonical rate constants reported by Madden *et al.*[144] and indeed find this to be the case, with channel (1) accounting for over 90% of the products. Hence, at 248 nm, simple C—H bond fission to form H + *o*-benzyne is the dominant dissociation mechanism.

At 193 nm, phenyl dissociates via H atom loss and by channel (2), with channel (2) as the dominant pathway. The P(E_T) distribution for H atom loss is similar to that at 248 nm, except that it extends to higher E_T and, as a consequence, $\langle E_T \rangle$ is higher. The P(E_T)

distribution for channel (2) peaks around 9 kcal/mol. As was the case at 248 nm, all data could be fit assuming an isotropic angular distribution. The P(E_T) distribution for channel (2) is consistent with ground state dissociation over the small exit barrier (TS3) on the surface shown in Figure 5.1. Under these circumstances, one would expect the H atom loss channel at 193 nm to have significant contributions from channels (1) and (3), because once decyclization of the phenyl radical occurs, channel (3) should occur in addition to channel (2).

One must also consider the product branching ratios in evaluating the dissociation mechanism at 193 nm. We find the channel (2)/channel (1+3) ratio to be 5.3 ± 0.8. For ground state dissociation, this value implies that (a) decyclization dominates over C—H bond fission to generate H + *o*-benzyne, and that (b) once decyclization does occur, channel (2) dominates over channel (3). Both results are rather surprising, at first glance. Channel (1) is not only lower in energy than the two decyclization channels but also, according to Figure 5.1, proceeds without an exit barrier, in contrast to channels (2) and (3). Under these circumstances, one would expect a larger unimolecular rate constant for a low energy channel that proceeds by a loose transition state compared to a higher energy channel involving a tight transition state. Moreover, it is not obvious by inspection of Figure 5.1 why channel (2) should prevail over channel (3).

These questions can be addressed by considering the variational Rice-Ramsperger-Kassel-Marcus (RRKM) calculations by Madden *et al.*,[144] in which microcanonical rate constants as a function of energy were calculated for C-H bond fission (channel 1), decyclization (over TS1), recyclization (the reverse reaction over TS1), and dissociation of the decyclized intermediate to channels (2) and (3). These calculations showed that the transition state for channel (1) is not as loose as, for example, the transition state for the H + CH_3 recombination reaction [r(C-H)=3.4 Å at T=300K],[153] and that it moved inward along the reaction coordinate with increasing internal energy, thereby reducing the rate constant for channel (1). Specifically, the value of r(C-H) that produced the smallest rate constant for channel (1) dropped from 2.9 Å at 300 K to 2.3 Å at 2500 K. In addition, although TS5 leading to channel (3) is lower in energy than TS3 leading to channel (2), the rate constant for dissociation over TS3 becomes larger at a total energy of 150 kcal/mol, presumably reflecting the larger number of available states at TS3 with increasing energy. Using the microcanonical rate constants from Madden *et al.*[144] with r(C-H)=2.3 Å for the channel (1) transition state, we calculated the product branching ratios by solving their kinetic model . We found that by 155 kcal/mol total energy, which is comparable to the energy of a 193 nm photon (148 kcal/mol), channel (2) was larger than either channel (1) or channel (3), and that as the energy was further increased, so did the relative contribution from channel (2). However, the channel (2) yield did not equal the sum of channels (1) and (3) until considerably higher energy (190 kcal/mol), and certainly did not approach the experimental branching ratio under any circumstances. It thus appears that the experimental product branching ratio is not consistent with statistical unimolecular decay on the potential energy surface in Figure 5.1, suggesting either that the surface needs to be improved, or that non-statistical dynamics are at play at 193 nm.

In fact, the surface in Figure 5.1 is incomplete as it only considers the *n*-C_4H_3 + C_2H_2 channel and does not include *i*-C_4H_3 + C_2H_2. Two recent high-level electronic structure calculations[154,155] find that *i*-C_4H_3 (H_2CCCCH) lies 12 kcal/mol lower in energy than *n*-C_4H_3 (HCC(H)CCH). Moreover, calculations by Lories *et al.*[145] find that the exit barrier for dissociation to *i*-C_4H_3 + C_2H_2 is 7.9 kcal/mol. These values, when applied to Figure 5.1, result in a transition state lying at 94.1 kcal/mol with respect to the bottom of the C_6H_5 well, lower than either TS3 (105.6 kcal/mol) or TS5 (97.0 kcal/mol). While additional hydrogen-shifting is required to reach *i*-C_4H_3 + C_2H_2 from phenyl, Lories *et al.*[145] find the barriers for these processes to be considerably lower than the exit barrier, indicating that dissociation of energized phenyl to *i*-C_4H_3 + C_2H_2 is feasible. The implications of this new pathway for our experiment are significant, as it represents a channel that would compete more effectively with both channels (1) and (3) on the ground state surface. In particular, the lower exit barrier relative to TS5 would drop the yield of channel (3) substantially. Hence, while rate constants for dissociation to *i*-C_4H_3 + C_2H_2 have not been reported to date, inclusion of this channel in an overall kinetic model would clearly produce better agreement with our experimental branching ratio at 193 nm.

5.6 Conclusions

The photodissociation dynamics of the phenyl radical have been explored at 248 and 193 nm using photofragment translational spectroscopy. Translational energy P(E_T) distributions and product branching ratios were determined. At 248 nm, only H + C_6H_4 products were observed. The P(E_T) distribution indicated a reaction coordinate with little or no barrier, and this channel was attributed primarily to H + *o*-C_6H_4 (channel 1) formed by C—H bond fission on the ground state surface.

At 193 nm, H atom loss was observed along with momentum-matched C_4H_3 + C_2H_2 products. The P(E_T) distributions for H atom loss again peaked at very low energy, while that for C_4H_3 + C_2H_2 (channel 2) peaked around 8 kcal/mol, consistent with dissociation over a small exit barrier. This channel results from decyclization of the phenyl radical prior to dissociation. The decyclized radical can also dissociate to H + *l*-C_6H_4 (channel 3), so this channel along with the lower energy channel (1) can contribute to the overall dissociation via hydrogen atom loss at 193 nm. The branching ratio, channel (2)/channel (1+3), was 5.3±0.8. The kinetic energy distributions for the two mass channels were suggestive of ground state dissociation dynamics. However, using microcanonical rate constants previously determined by Madden *et al.*,[145] we were unable to reproduce the experimental branching ratio, finding too little channel (2). These calculations, however, assumed that channel (2) was *n*-C_4H_3 + C_2H_2, and we would expect that incorporation of the lower energy *i*-C_4H_3 + C_2H_2 channel into the overall kinetics would result in considerably better agreement with experiment.

5.7 Acknowledgments

This work was supported by the Director, Office of Basic Energy Sciences, Chemical Sciences Division of the U.S. Department of Energy under Contract No. DE-AC02-05CH11231. The authors also thank Ralf Kaiser and Stephen Klippenstein for helpful discussions.

Chapter 6

Photodissociation Dynamics of the Phenyl Radical at 193 nm

Previous work in our group examined the unimolecular photodissociation dynamics of the phenyl radical at 193 nm. A flash pyrolysis source was used for the production of the phenyl radical and photofragment translational spectroscopy (PTS) was used to identify two dissociation pathways forming H + C_6H_4 and C_4H_3 + C_2H_2. Acetylene loss (C_2H_2) was found to dominate over the combined H atom loss channels (resulting in either *o*-C_6H_4 or *l*-C_6H_4) with a branching ratio of 5.3±0.8. Attempts to reproduce this branching ratio by solving the kinetic model while assuming ground state dynamics were unsuccessful. Recent work in our group used a grid discharge source, colder pyrolysis temperatures, and different carrier gasses to reinvestigate the photodissociation dynamics of this radical at 193 nm. Acetylene loss was yet again found to dominate the dissociation dynamics of the phenyl radical.

6.1 Introduction

The phenyl radical, *c*-C_6H_5, is an important intermediate in the combustion of aromatic hydrocarbons. The phenyl radical is the simplest aromatic species and it can polymerize readily to form polyaromatic hydrocarbons.[122] The formation of this radical from smaller aliphatic species is considered to be the rate determining step in the production of large aromatic hydrocarbons.[119,120] The unimolecular decay of this radical is also of considerable interest since shock-tube studies have found it to be an intermediate in the thermal decomposition of benzene.[123,124,125]

The dissociation channels accessible with the absorption of a single 193 nm photon by the phenyl radical consist of two H atom loss channels and an acetylene loss channel:

1) $c\text{-}C_6H_5 \rightarrow o\text{-}C_6H_4 + H$ ΔH_0=76.0 kcal/mol (6.1)

2) $c\text{-}C_6H_5 \rightarrow l\text{-}C_6H_5 \rightarrow n\text{-}C_4H_3 + C_2H_2$ ΔH_0=98.2 kcal/mol (6.2)

3) $c\text{-}C_6H_5 \rightarrow l\text{-}C_6H_5 \rightarrow l\text{-}C_6H_4 + H$ ΔH_0=91.0 kcal/mol (6.3)

Channel (1) is the lowest energy pathway and it involves simple C—H bond fission at the *ortho* position to form a hydrogen atom and *ortho*-benzyne, a cyclic molecule. Ring opening proceeds over a transition state located 64 kcal/mol above the ground state and forms $l\text{-}C_6H_5$, a linear conformer which can subsequently progress to the higher energy dissociation pathways shown above.

The importance of ring-opening is the main question regarding the dissociation dynamics of the phenyl radical. While the two H atom loss channels have somewhat similar energetics, and might not be easily distinguished from one another, detection of channel (2) would be a clear indication on the decyclization of the phenyl radical. Previous theoretical work[144,149] and experimental work[150] concluded H atom loss from the cyclic conformer to dominate. This theoretical work, however, allowed for the augmented importance of ring-opening with increasing excitation energy. Previous work performed in our group at 248 nm[92] agreed with these conclusions and found H atom loss to be the only photodissociation channel to be accessed at this wavelength. The same study, further investigated the dissociation dynamics at higher energies using 193 nm photons. Unexpectedly, C_2H_2 loss was found to dominate at this wavelength, a result that could not be explained with the kinetic model of the previously published theoretical work.[144] Our result concluded that ring-opening is the major pathway for phenyl radical decomposition at higher excitation energies. We were not able to justify this result, but we did however propose that the internal energy of the phenyl radicals as well as the possibility of a second C_2H_2 loss channel[154,155,145] forming $i\text{-}C_4H_3$ could make our experimental result plausible.

In the work presented here we want to investigate the possibility that phenyl radicals created with a pyrolysis source can contain large amounts of internal energy, which could affect the observed branching ratio. This possibility was investigated by producing phenyl radicals in different ways; with a direct current discharge source as well as under a variety of pyrolysis source conditions. The collisionless photodissociation decay dynamics of phenyl radical at 193 nm are thus investigated once more while using the same experimental technique, photofragment translational spectroscopy. The previously observed dissociation channels were identified in the study presented here, and C_2H_2 loss was found to dominate once more.

6.2 Experiment

The work presented here was performed on the same apparatus previously used for investigating the collisionless photodissociation dynamics of the phenyl radical. The detection scheme used has been described previously[10,92] and will only be presented very briefly in this section. This study was performed on a molecular beam photodissociation apparatus with a fixed source and a rotatable detector. The nitrosobenzene sample was maintained at room temperature under a 4 atmosphere backing pressure containing 90% helium with 10% argon. The pulsed valve was backed by a pressure of about 1000 Torr of this mixture with the help of a vacuum regulator. A helium and argon mix was prepared to produce a slower molecular beam than would normally be obtained with pure He.

The molecular beam was produced with a piezo-activated pulsed valve and collimated by two skimmers that separate the source chamber from the main scattering chamber, where the molecular beam is crossed at 90^0 with the 2 x 4 mm^2 focused beam spot of the photodissociation laser. A Lambda-Physik excimer laser at 193 nm was used to create pulses with about 30 mJ of energy. The scattered photofragments were detected as a function of the laboratory angle, Θ, by a triply-differentially pumped detector that uses electron impact ionization coupled to a quadrupole mass filter and a Daly style ion counting setup.[93] A multichannel scaler was used to bin ion counts as a function of detection time to create time-of-flight (TOF) spectra. Every spectrum shown was collected by maintaining the laser repetition rate at 100 Hz and the pulsed valve at 200 Hz, so that background subtraction could be achieved. An iterative forward convolution method that takes into account all the machine parameters was used to simulate the TOF spectra and thus determine the translational energy distributions, $P(E_T)$, in the center-of-mass frame of reference,[95] distributions that are not machine dependent and thus can be used to understand the dissociation mechanism.

The important difference in the study presented here from previous work performed by our group[92] is in the method used for radical production. Our previous study used a SiC flash pyrolysis source[151] to produce the phenyl radical by pyrolysis of the C—N bond in nitrosobenzene (C_6H_5NO) entrained in a pure helium beam. The temperature of the pyrolysis source can be controlled by changing the power applied to the SiC tube; where higher powers increase the temperature. Previously, the temperature of the pyrolysis source was increased until the nitrosobenzene parent was fully depleted.[92] In other work by our group, use of the pyrolysis source to form the *tert*-butyl radical showed that temperature can strongly influence the chemistry taking place inside the source.[109] For this study, phenyl radicals were produced at colder temperatures as well where the nitrosobenzene parent was not fully depleted from the beam. This process can be monitored quite easily by obtaining mass spectra of the molecular beam with the detector rotated at a lab angle of 0^o. Depletion of C_6H_5NO in the beam can be monitored by looking at m/z = 107 ($C_6H_5NO^+$). If nitrosobenzene is not fully depleted from the molecular beam it will absorb at 193 nm and contaminate the photodissociation signal.[150]

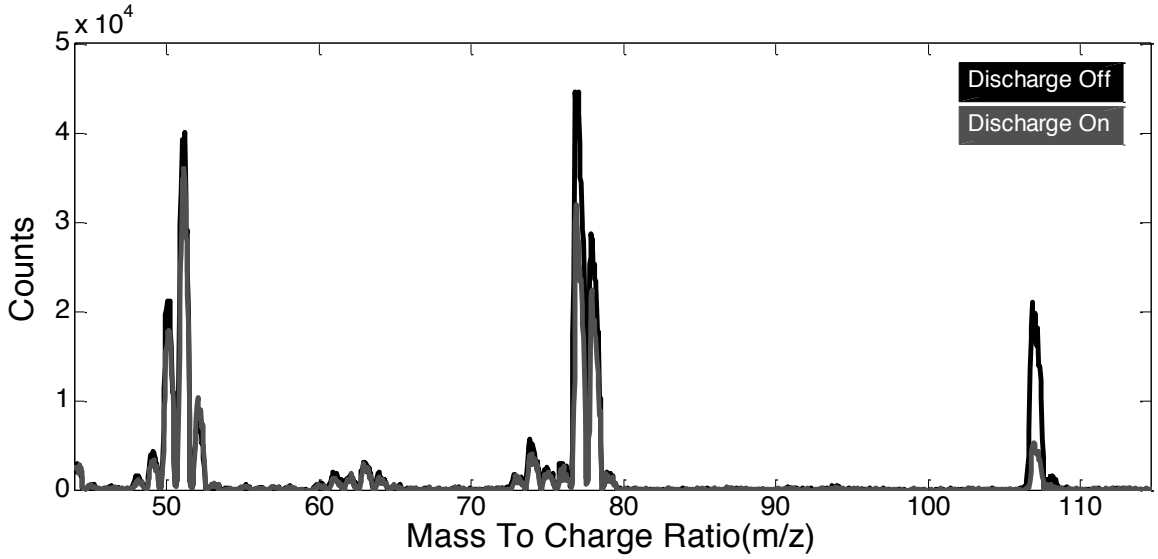

Fig. 6.1 Mass spectrum of nitrosobenzene molecules seeded in a helium beam taken with the discharge source off (in black) and at a voltage of 1.4 kV (in gray).

However, colder source temperatures were sampled since high temperatures can lead to the formation of other products in the source. With this in mind, the photodissociation signal was monitored at different source temperatures.

As an alternative to the pyrolysis source a direct current grid discharge source[46] was also employed for radical production. Discharge sources of this type have been shown to produce internally colder ions when compared to ions obtained with other discharge source designs.[45] This source consists of two mesh electrodes sandwiched between three polyoxymethylene plastic spacers that are mounted directly to the pulsed valve. The thickness of the polyoxymethylene spacers is about 1 mm each. The nozzle inner diameter used for the electrical discharge and radical expansion is 2 mm. A negative voltage between 1000 and 1500V was applied to the electrode closest to the valve, while the second electrode was grounded. Discharge between the electrodes was triggered by the passage of nitrosobenzene molecules seeded in helium. The mass spectra of the molecular beam with discharge on and off are shown in Figure 6.1 and show depletion of the nitrosobenzene parent at m/z = 107. This is similar to the depletion obtained with the use of the pyrolysis source except that is not complete and that parent is still present in the beam regardless of how high a voltage is applied to the electrodes.

6.3 Results

TOF spectra were taken for m/z = 76 ($C_6H_4^+$), m/z = 51 ($C_4H_3^+$), and m/z = 26 ($C_2H_2^+$), the ionized primary fragments for channels (1)-(3), and for m/z = 50 ($C_4H_2^+$), a daughter ion formed by dissociative ionization in the electron impact ionizer where fragments resulting from H atom loss and C_2H_2 loss can be observed simultaneously. The TOF spectra shown in Figure 6.2 were collected at m/z = 50 at multiple laboratory scattering

angles Θ of 7° and 8°. In these figures, the open circles represent the TOF data, while solid lines represent forward convolution simulations obtained with the PHOTRAN[95] fitting routine. All spectra are background-subtracted as described in the previous section.

The TOF spectra shown in Figure 6.2 panels a) through e) were obtained from use of the pyrolysis source while the discharge source was used for the spectrum in panel f). The width of the TOF peaks in Figure 6.2 varies significantly due to differences in beam

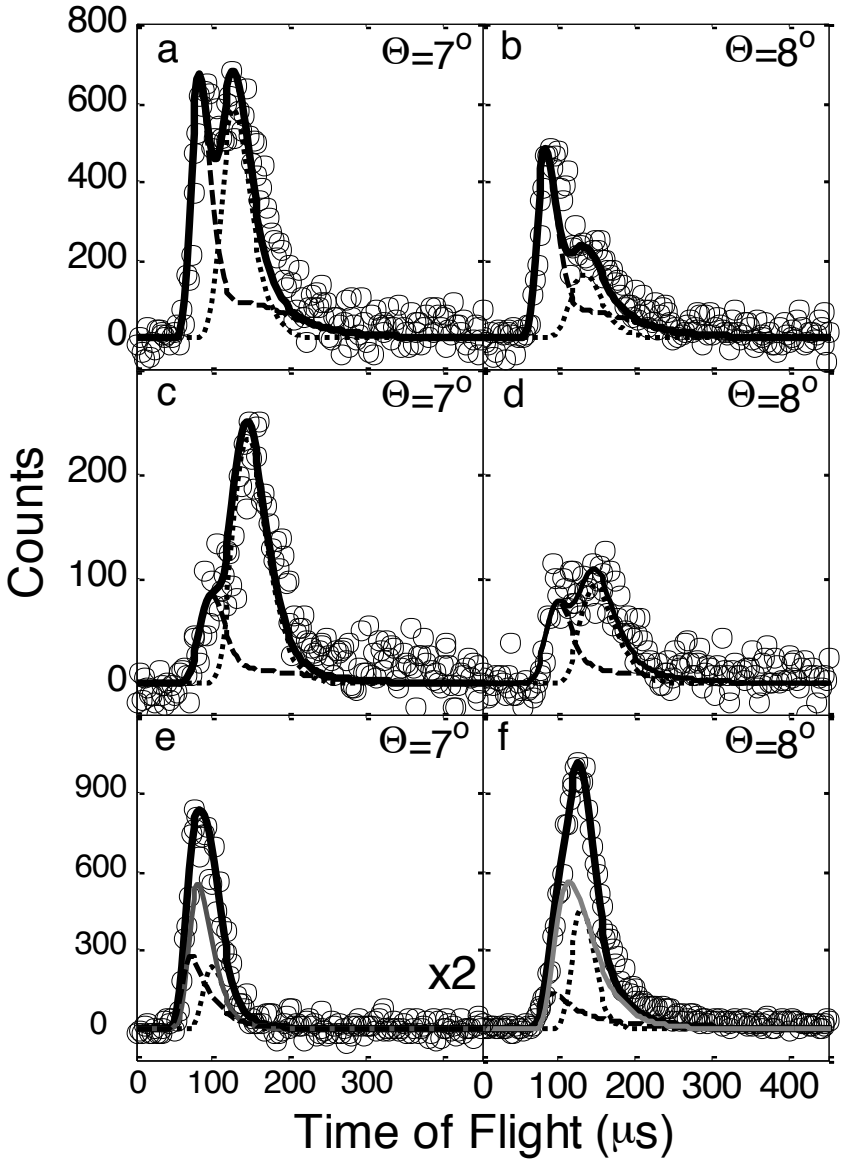

Fig. 6.2 Characteristic TOF spectra at *m/z* = 50 (C_4H_2) taken with multiple sources and source conditions. Panels a) and b) are reprinted for comparison from our previous investigation[92] of the dissociation dynamics of the phenyl radical. Panels c) and d) show TOF spectra taken with a hot pyrolysis source, while panel e) shows a spectrum taken under colder conditions. Panel f) shows representative TOF spectrum of the photodissociation signal obtained with a discharge source. See text for details.

velocities while acquiring data. The data in panels a) and b) were acquired with a beam velocity of around 1650 m/s, the data in panels c) and d) were acquired with a beam velocity of around 1450 m/s, and the data in panels e) and f) with beam velocities of 2200 and 1600 m/s, respectively. The TOF spectra acquired with high pyrolysis temperatures, panels a) through d), show the presence of only two peaks, while the TOF spectra taken with lower pyrolysis temperatures (e) and with the discharge source (f) show the presence of a single peak. The TOF spectra in panels a) and b) were previously published[92] and are shown here for reference. These spectra were taken under conditions where the nitrosobenzene parent was fully depleted form the molecular beam. The spectra in panels c) and d) were taken under similar source conditions, where the nitrosobenzene parent was fully depleted from the argon-helium molecular beam. The spectrum in panel e) of Figure 6.2 was taken at lower source temperatures where the nitrosobenzene parent was not fully depleted from the molecular beam. The spectrum in panel f) was obtained with the discharge source under conditions similar to the ones that produced the mass spectrum in Figure 6.1.

6.4 Analysis

The above results show that there are at least three photodissociation channels present. Two of the channels are very likely due to hydrogen atom loss and acetylene loss, the two previously observed dissociation pathways of the phenyl radical at this wavelength. The additional contribution that appears in the TOF spectra from panels e) and f) of Figure 6.2 is very likely caused by nitrosobenzene photodissociation. As evidenced by the persistent peak at m/z = 107 in Figure 6.1 nitrosobenzene is present in the beam, and since it undergoes NO loss at 193 nm[150] this contribution should be detected at m/z = 50. Center-of-mass photofragment energy and angular distributions, $P(E_T, \theta)$, can be obtained by fitting the TOF spectra. The $P(E_T, \theta)$ distribution can be rewritten in terms of the uncoupled center-of-mass translational energy $P(E_T)$ and angular distribution $I(\theta, E_T)$:

$$P(E_T, \theta) = P(E_T)I(\theta, E_T) \tag{6.4}$$

The PHOTRAN[95] forward convolution program was used to simulate TOF spectra for all the data sets according to an assumed $P(E_T)$ distribution. The input $P(E_T)$ distribution for a particular channel can be adjusted point-wise until the TOF spectra pertaining to that channel are simultaneously fit. Conservation of energy allows us to calculate the total translational energy, E_T, in the center-of-mass frame:

$$E_T = h\upsilon + E_0 - E_{int} - D_0. \tag{6.5}$$

In this equation $h\upsilon$ is the photon energy, D_0 is the dissociation energy for the channel of interest, E_{int} is the total internal energy of the fragments, and E_0 is the initial energy of the phenyl radicals. Equation 6.5 can be used to calculate the maximum translational energy

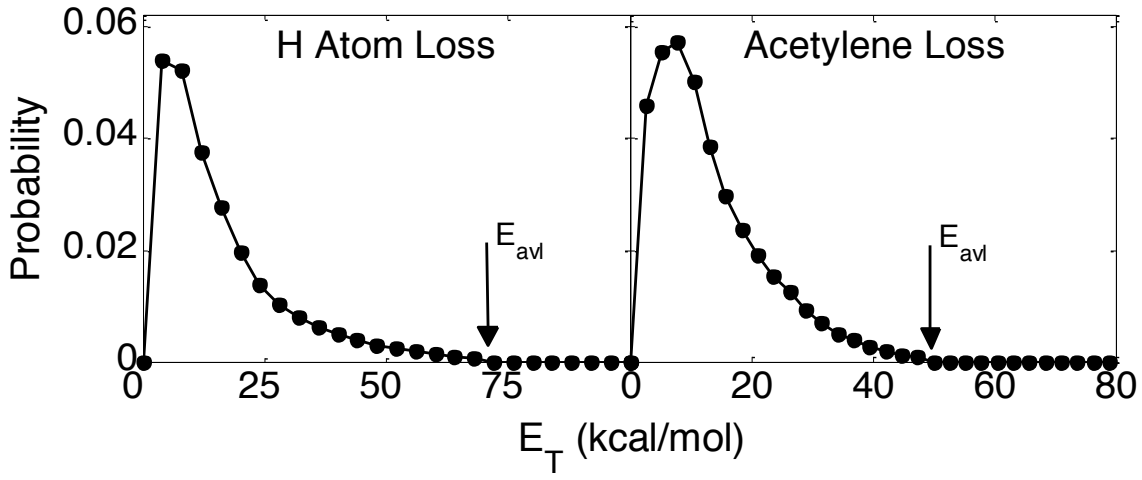

Fig. 6.3 Previously published[92] center-of-mass translational energy distributions for the photodissociation dynamics of the phenyl radical at 193 nm, representing the H atom loss channels and C_2H_2 loss channels.

possible for the photoproduct of interest if the photoproducts are assumed to contain no internal energy.

The input translational energy distributions used to produce the dotted and dashed simulations were identical to the previously published P(E_T) distributions[92] reprinted in Figure 6.3. These simulations were superimposed on the TOF data obtained for all the different source designs and parameters. Further optimization of the translational energy distributions was not necessary since the simulations were found to be adequate for the collected data. As such, the dashed line in Figure 6.2 was generated with the P(E_T) distribution previously used to fit the acetylene loss channel of the phenyl radical to form C_4H_3. This distribution peaks at 8 kcal/mol with an average translational energy of 13 kcal/mol, and extends to the maximum allowed translational energy of 50 kcal/mol. The dotted line was created with the H atom loss P(E_T) distribution from Figure 6.3. This is a distribution with an average translational distribution $<E_T>$ = 16 kcal/mol that extends to the maximum allowed energy at this dissociation wavelength of 72 kcal/mol.

The third simulation, shown in panels e) and f) of Figure 6.2 as a gray line, for the TOF spectra taken with lower pyrolysis temperatures and with the discharge source was necessary to properly simulate those spectra, as the translational energy distributions shown in Figure 6.3 cannot fit the TOF data adequately. The best fits obtained for this peak were generated with a P(E_T) distribution that has an average translational energy distribution of $<E_T>$ = 8 kcal/mol and extends to 40 kcal/mol. One possibility for the source of this signal is nitrosobenzene contamination of the beam. To test this possibility, the nitrosobenzene photodissociation dynamics at 193 nm were also investigated. The only photodissociation channel previously observed[150] and also identified in this work consists of NO loss to form the phenyl radical. The distribution used to produce the gray fits in Figure 6.2 was the same distribution used to simulate the nitrosobenzene photodissociation signal.

The universal detection scheme used in this experiment enables extraction of the branching ratio for channels (1-3) and (2) at 193 nm.

$$\frac{channel\ (2)}{channel(1+3)} = R \times \frac{\sigma_{C_6H_4}}{\sigma_{C_4H_3}} \times \frac{f_{C_6H_4}}{f_{C_4H_3}} \tag{6.6}$$

The ratio R represents the relative weights of the P(E_T) distributions used by the fitting program to reproduce the relative intensities of the observed contributions. The values of σ denote the relative electron impact cross sections of the photofragments[115] while f is the signal fraction of the photofragment of interest that appears at m/z = 50 via dissociative ionization. The branching ratio was only calculated between H atom loss and C_2H_2 loss channels of the phenyl radical. The signal produced by nitrosobenzene was not taken into account since the amount of nitrosobenzene in the beam depends on source conditions and is not a meaningful parameter. For this study, the branching ratio was found to be 3.6.

6.5 Discussion

The principal objective of this study was to address the apparent discrepancy between the experimentally observed and the theoretically predicted branching ratio. If dissociation takes place on the ground state surface, channel (1) would be expected to dominate. When faced with this dilemma in our previous study we presented two possible reasons for this discrepancy. One reason addressed the potential energy surface of this system and suggested the possibility of C_2H_2 loss forming *i*-C_4H_3 in addition to *n*-C_4H_3. The *iso* conformer is lower in energy[154,155] and this could potentially make this exit channel competitive with H atom loss from *c*-C_6H_5. The second reason considered the theoretical work of Madden *et al*.[144] where the authors predicted the linearization of phenyl radicals to play a progressively more important role at higher and higher excitation energies. This idea suggested that if the internal energy of the radicals is substantial it could potentially explain the observed branching ratio.

Extra internal energy of the phenyl radicals could be caused by the high temperature of the pyrolysis source. The design of the pyrolysis source used[151] was conceived in such a way that the supersonic expansion would cool and isolate the newly formed radicals. While supersonic expansions are known to effectively cool the internal temperature of the expanded species, this cooling could depend on the environment inside the pyrolysis tube. The hope for the study presented here was that using a colder pyrolysis source would produce internally colder radicals. The observation of a different branching ratio under these conditions would support this hypothesis. This, however, was not possible due to nitrosobenzene contamination of the radical beam. This contamination is problematic in two ways: the NO loss contribution washes out the phenyl radical photodissociation signal, and ten percent of the phenyl radicals formed by this pathway undergo spontaneous secondary dissociation to form *ortho*-benzyne and hydrogen atoms.

For these reasons, it was not possible to obtain a branching ratio from these spectra. The photodissociation spectra obtained from radicals produced with the discharge source, represented by a TOF spectrum in panel f) of Figure 6.2, suffered from nitrosobenzene contamination since it was not possible to fully deplete the precursor.

The pyrolysis source was once more heated to the temperature necessary to fully deplete the nitrosobenzene precursor. The TOF spectra obtained are shown in Figure 6.2 panel c) and panel d). Although the lab-frame velocities of the molecular beams used to obtain the spectra in panels a) through d) were very similar, the branching ratios for phenyl dissociation are clearly different between the current and old data. This translates into a different branching ratio, although the source conditions were very similar. The only notable difference is the use of 10% arogon in the gas mix instead of pure helium. This mix was used to slow down the molecular beam so that the two channels could be better resolved. The previously obtained spectra[92] were taken with pure helium, and the exact reason for the relatively low beam velocity for that data set is not known. The newly observed ratio of 78:22 instead of the previously observed 84:16 is still in favor of dissociation via channel (2) and thus decyclization. This gives a ratio of 3.6 as opposed to the previously published 5.3 ± 0.8. The argon gas that was also incorporated in the molecular beam can more efficiently cool radicals in the supersonic expansion, which could explain the difference observed in the branching ratio.

The TOF spectra are clearly different, so it is not surprising that the new branching ratio is outside the uncertainty of our previous measurement.[92] While the newly measured branching ratio is closer to theoretical predictions,[144] it is still in great favor of C_2H_2 loss and decyclization. While the exact reasons for this discrepancy are still not clear, recent work that investigated the H atom loss channels in the ultraviolet photodissociation of the phenyl radical[156] found a translational energy distribution compatible with the distribution in Figure 6.3. This study was performed using high-*n* Rydberg time-of-flight mass spectrometry and while looking at the dissociation dynamics in the wavelength region of 268-215 nm concluded that the electronically excited phenyl radical underwent unimolecular dissociation after internal conversion to the ground state.

6.6 Conclusions

The photodissociation dynamics of the phenyl radical at 193 nm have been revisited. Phenyl radicals are very reactive species, so they must be produced in a collisionless environment. This was accomplished with the use of a flash pyrolysis source and a grid discharge source. Although the newly formed radicals are jet-cooled by supersonic expansion in both cases, it is possible that a grid discharge source would produce internally colder radicals. The principal goal of the study presented in this chapter was to determine if acetylene loss would still be the major dissociation pathway for radicals formed with a grid discharge source. Unfortunately, it was not possible to measure a reliable branching ratio for phenyl dissociation pathways due to nitrosobenzene precursor contamination of the molecular beam.

6.7 Acknowledgments

This work was supported by the Director, Office of Basic Energy Sciences, Chemical Sciences Division of the U.S. Department of Energy under Contract No. DE-AC02-05CH11231.

Chapter 7

Photodissociation dynamics of the Ethoxy Radical at 248 nm and 193 nm Via Photofragment Translational Spectroscopy

The photodissociation dynamics of the ethoxy radical have proven to be very complex. The potential energy surface for this system has been studied with many experimental and theoretical techniques. Despite the amount of attention that the ethoxy radical has received, questions regarding the dissociation mechanism require further investigations. The study presented in this chapter studied the photodissociation dynamics of ethoxy radicals at 248 nm. One dissociation pathway proceeding to methyl radical (CH_3) loss to form formaldehyde (CH_2O) was identified. The translational energy distribution used to fit this channel peaks at 6 kcal/mol and is consistent with statistical dissociation on the ground state surface.

7.1 Introduction

Alkoxy radicals are neutral free radicals composed of an alkyl group and an oxygen atom. They are important intermediates in combustion and atmospheric chemistry,[157,158,159,160] such as the tropospheric degradation of volatile organic compounds.[160] The chemistry of alkoxy radicals is directly responsible for the composition of the first-generation end-products of hydrocarbon oxidation, and since most hydrocarbons in Earth's troposphere are of biogenic origin[161] this is an important process for large regions of the globe. One of the simplest and most studied alkoxy radicals is the ethoxy radical, $C_2H_5O^{\bullet}$. In combustion chemistry, this radical is believed to be an intermediate in the combustion of ethanol and other oxygen containing compounds.[160] More specifically, it is an intermediate in the reaction of ethyl radical with an oxygen atom[162,163,164,165] as well as in the reaction of ethylene with the hydroxyl radical.[166,167,168,169,170,171,172,173,174,175,176,177,178,179,180,181,182,183,184] In atmospheric[175,178,184,185] chemistry, the ethoxy radical is a tropospheric intermediate species in the degradation of

volatile organic compounds[186] where it can be formed from the self-reaction of ethyl peroxy radicals, or from the reaction of ethyl peroxy with NO.[187] The fate of ethoxy radicals formed in the atmosphere is to most likely react with O_2[188,189,190] or with NO_X,[160,190] to undergo unimolecular dissociation,[160] or to isomerize to α-hydroxyethyl (CH_3CHOH) or β-hydroxyethyl (CH_2CH_2OH).[191,181,192]

The ethoxy radical can react, decompose, or isomerize. A lot of the measurements mentioned above were interested in the reaction kinetics between ethoxy and other atmospheric species. The rate constants for multiple bimolecular reactions involving the ethoxy radical under tropospheric conditions show that reaction with molecular oxygen is the major removal process.[193,194,195,157] Ethoxy radicals can also decompose in the atmosphere, and a wide array of kinetic studies explored this process. Chemically excited ethoxy radicals were most commonly produced by the reaction of O^3P with the ethyl radical or from isomerization of the β-hydroxyethyl radical produced by the reaction of hydroxyl radical with ethylene. These theoretical and experimental studies converge on the same dissociation channels for the three C_2H_5O isomers. For ethoxy, CH_3 loss and H atom loss are considered to be the major dissociation channels. The α-hydroxyethyl radical can decompose by two distinct H atom loss channels while the β-hydroxyethyl radical can proceed through either H atom loss or OH loss. Isomerization between ethoxy and the hydroxyl radicals, however, is a process that takes place through highly strained cyclic transition states. For this reason, isomerization is not considered to be kinetically significant in the atmospheric and combustion chemistry of alkoxy radicals containing fewer than four carbon atoms.[160]

Recent experimental work[196] performed in our group investigated ethoxy radical dissociation dynamics with fast radical beam photodissociation coupled to coincidence photofragment detection. Many of the dissociation pathways listed above have similar fragment mass ratios and insufficient mass resolution intrinsic to the detector used made it impossible for the authors to unmistakably assign the dissociation products. However, after deuteration of the ethoxy radical and on the shifts observed in fragment masses vinyl radical resulting from H_2O loss was identified.[196] This result was suspect due to the two high energy isomerization barriers that must be overcome for this channel to take place. Upon the acquisition of a new coincidence imaging detector with enhanced fragment mass resolution the photodissociation dynamics of the ethoxy radical were reevaluated with the same technique.[197] This study identified the presence of three dissociation channels in equal yields: methyl radical loss to form formaldehyde (CH_2O), hydrogen atom loss to form acetaldehyde (CH_3CHO), and hydroxyl radical loss to form ethane (C_2H_4). Hydroxyl radical loss can only take place after isomerization to the β-hydroxyethyl radical. The observed fragment translational energy distributions, angular distributions, and branching ratio suggest that statistical dissociation on the ground state surface does not take place, but rather that isomerization to β-hydroxyethyl takes place on an excited state surface.

The photodissociation experiments described above motivate the work presented here. Photofragment translational spectroscopy was used to probe the photodissociation dynamics of ethoxy radicals at 248 nm, which excite the radicals to the $\tilde{C}^2A''$ state from

the $\tilde{X}^2A''$ ground state.[197] Ethoxy radicals were produced from the pyrolysis of ethyl nitrite and supersonically expanded into vacuum. Only one photodissociation pathway was observed, consisting of methyl radical loss to form formaldehyde.

7.2 Experiment

A molecular beam photodissociation apparatus with a rotatable detector was used to perform the work shown here. Details of the flash pyrolysis radical source and of the detection scheme employed have been described in previous chapters. An ethoxy radical beam was generated from the pyrolysis of ethyl nitrite (CH_3CH_2ONO) molecules with a resistively heated SiC tube mounted to a piezoactivated pulsed valve. The ethyl nitrite beam was obtained by bubbling 1.5 atm of high purity He through a liquid sample of the parent molecule submerged in an acetone and dry ice slush. Ethyl nitrite and deuterated ethyl nitrite were synthesized in-house[198] by the acid mediated substitution of the OH group of ethanol with the nitrite group of sodium nitrite ($NaNO_2$). In short, this was accomplished by slowly adding sulfuric acid to a stirred and chilled solution of ethanol, water, and sodium nitrite. The ethyl nitrite was isolated with a separatory funnel and stored at liquid nitrogen temperatures. For deuterated ethyl nitrite (CD_3CD_2ONO) fully deuterated ethanol was used. The mass spectra for the deuterated and non-deuterated ethyl nitrite are shown in Figure 7.1. The mass spectrum did not show substantial change in structure with pyrolysis temperatures except for a loss in intensity, and are very similar to the spectra shown here.

It was observed that increasing the temperature of the source pyrolysed the parent molecules completely but also destroyed the observed photodissociation signal. For this reason, photodissociation signal was obtained at intermediate source temperatures where ethyl nitrite parent was still present in the molecular beam. This means that the photodissociation signal could originate from ethyl nitrite photodissociation at 248 nm. To account for this contribution, photodissociation data was collected with a cold source where the only components of the molecular beam are the ethyl nitrite parent and helium gas.

The radicals produced in this manner were subsequently expanded supersonically into the source chamber, collimated by two skimmers and photodissociated by the light of an excimer laser at 248 nm. The photodissociation laser beam was focused to a spot of 1 by 3 mm^2 and used to cross the ethoxy radical beam at 90^0. Pulse energies of about 30 mJ were obtained from a GAM excimer laser at 248 nm. The scattered photofragments were detected by a rotatable detector in the plane defined by the molecular and laser beams as described in previous chapters.

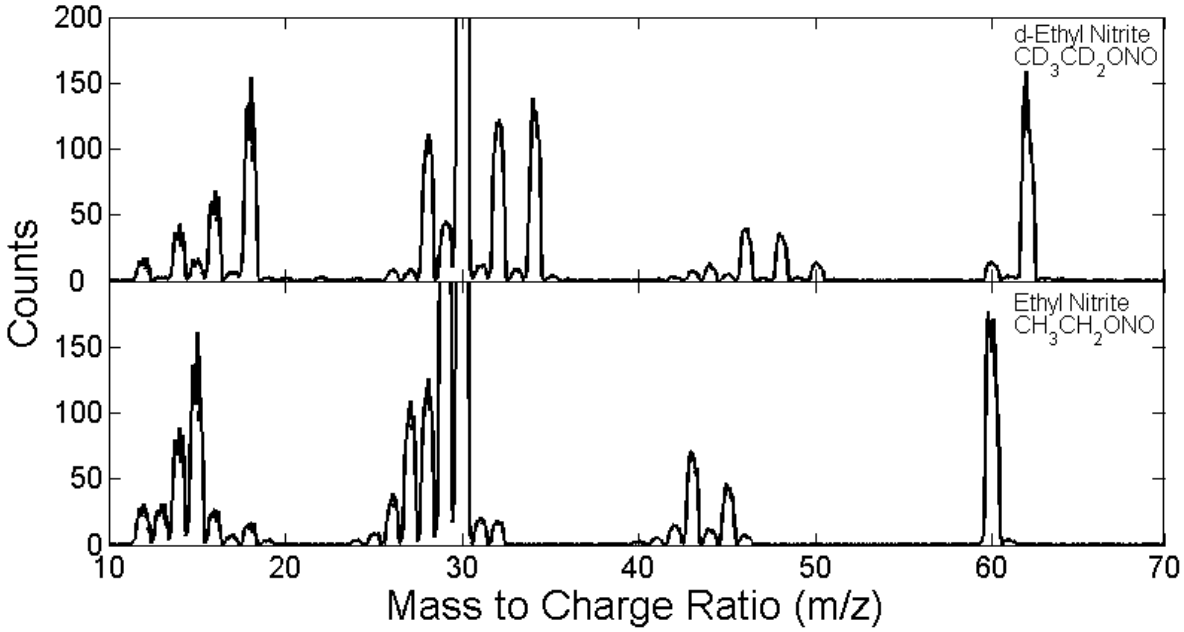

Fig. 7.1 Mass spectrum of ethyl nitrite molecules seeded in helium. The top trace shows the mass spectrum of fully deuterated ethyl nitrite.

The top trace of Figure 7.1 contains a peak at m/z = 62 while the bottom trace includes a peak at m/z = 60. These peaks are due to CH_2ONO^+ and CD_2ONO^+ and can only be formed from dissociative ionization of the parent. This mass to charge value is due to CH_2ONO and CD_2ONO respectively, a fragment that can only be obtained from dissociative ionization of the parent molecule, ethyl nitrite.

7.3 Results

The top trace of Figure 7.1 contains a peak at m/z = 62 while the bottom trace includes a peak at m/z = 60. The spectrum obtained for the deuterated ethyl nitrite beam also displays peaks at mass to even mass to charge ratios, indicating that the fully deuterated precursor was successfully synthesized. The two spectra are obtained under comparable conditions, so the identity of the different peaks can be deduced.

The photodissociation dynamics of both ethoxy and deuterated ethoxy radicals were probed at 248 nm, which is an excitation energy of 5 eV. For ethoxy radical photodissociation, time of flight spectra were collected at m/z = 43 (CH_2CHO^+), m/z = 30 (CH_2O^+), m/z = 29 (CHO^+), m/z = 26 ($C_2H_4^+$), m/z = 17 (OH^+), and m/z = 15 (CH_3^+). The mass to charge ratios selected were chosen to show the primary ionized fragments for the H atom loss, CH_3 loss, and OH loss channels, as well as daughter ions formed by dissociative ionization in the electron impact ionizer. Spectra were not collected for m/z = 44 (CH_3CHO^+) and m/z = 16 (CH_4^+) due to high background signal caused by residual

gas in our detection chamber. This is the principal reason why the fully deuterated precursor was synthesized; meaning that the CD_3CDO and CD_4 fragment could be observed background free at *m/z* = 48 and 20 respectively.

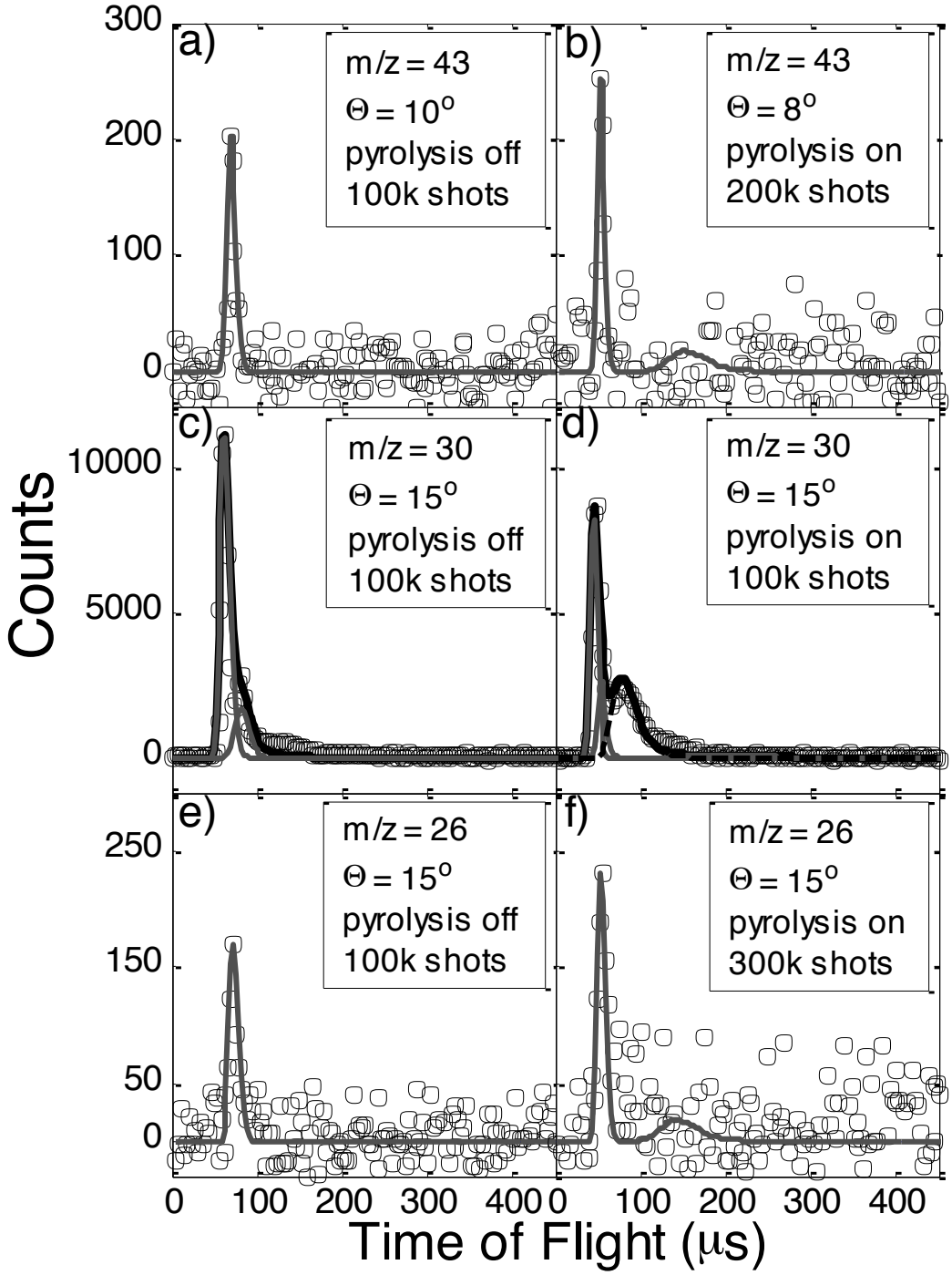

Fig. 7.2 Characteristic TOF spectra at *m/z* = 43, 30, and 26 taken with the pyrolysis source turned on and off from photodissociation at 248 nm. All TOF spectra shown are from non-deuterated precursor.

Figure 7.2 shows representative time of flight spectra for *m/z* = 43, 30, and 26 obtained with the pyrolysis source off for the left hand spectra and on for the right hand spectra. While the pyrolysis source is turned off the photodissociation signal is expected to originate from ethyl nitrite photodissociation only. At higher temperatures, where part of the ethyl nitrite precursor is depleted, part of the photodissociation signal could originate from ethoxy radicals produced in the pyrolysis source. The TOF spectra in panels a), b), c), e), and f) appears to be composed of a sharp feature, while the spectra in panel d) of Figure 7.2 contains an additional slower and broader peak. The width of the sharp feature in the spectra collected with the pyrolysis source off and the spectra collected with the pyrolysis source on is not the same due to the velocity difference between the beams obtained with the pyrolysis source on or off. At higher source temperatures the molecular beam becomes faster and faster approaching velocities more than twice as fast as those obtained with a cold source; 1000 m/s as compared to 2200 m/s. The intensity of the sharp feature is also lower in the time of flight spectra obtained with the pyrolysis source turned on, a difference that could be in part due to depletion of ethyl nitrite molecules under the hotter conditions, and to the faster lab-frame velocity of the photodissociated fragments.

7.4 Analysis

The detector used for performing the study presented here was a universal detector since it used electron impact ionization as the first step of the detection process. Electron impact ionization can be used to obtain a mass spectrum of the species of interest. Unfortunately, the identity of the different components forming a peak in the mass spectrum is not always known which can complicate analysis, especially for a system like ethyl nitrite where a peak at the parent mass to charge ratio (*m/z* = 75 for $CH_3CH_2ONO^+$) is not observed. Observing the parent peak is important for studies that use a pyrolysis source since depletion of the parent can most easily be accomplished by monitoring the intensity of the parent peak. The peak at *m/z* = 60 from Figure 7.2 can be due to either CH_3CHON^+ or to CH_2ONO^+ ions. Upon deuteration, this peak is observed at *m/z* = 62 so the majority of this peak must be formed by CH_2ONO^+ ion species. Given that these peaks are due to CH_2ONO^+ and CD_2ONO^+ they can only be formed from dissociative ionization of the parent, and can be used to monitor the amount of parent in the molecular beam. The same analysis can be used to characterize the rest of the mass spectrum.

The TOF data obtained from ethoxy radical and deuterated ethoxy radical photodissociation at 248 and 193 nm suggest the presence of at least one decomposition channel. Center-of-mass photofragment energy and angular distributions, $P(E_T, \theta)$, for the two product channels were obtained by fitting the TOF spectra of the photofragments. The $P(E_T, \theta)$ distribution can be rewritten in terms of the uncoupled center-of-mass translational energy distribution $P(E_T)$ and angular distribution $I(\theta,E_T)$ according to $P(E_T, \theta) = P(E_T)I(\theta, E_T)$. Although the laser beams used for this photodissociation study were

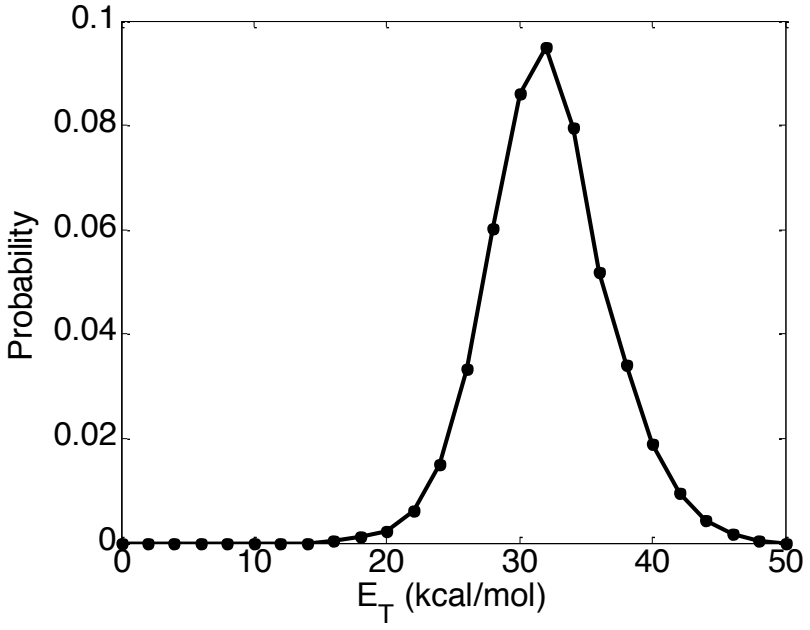

Fig. 7.3 Center-of-mass P(E_T) distribution from ethyl nitrite photodissociation at 248 nm to form CH_3CH_2O +NO. This distribution is quite narrow and peaks at around 30 kcal/mol.

unpolarized, it is possible for the photodissociation signal to be anisotropic in the plane defined by the molecular and laser beams. Since this is the plane in which the detector rotates, anisotropy must be taken into consideration while fitting the TOF spectra. However, the fits obtained for the TOF data were satisfactory while assuming an isotropic distribution for all values of E_T. The PHOTRAN,[95] CMLAB3,[199] and ANALMAX[200] forward convolution programs allowed the input of a point-wise adjustable P(E_T) distribution until a best fit was simultaneously obtained for all the TOF spectra attributed to that channel.

The total center-of-mass translational energy, E_T, is equal to the sum of the photon energy (115 kcal/mol) and the internal energy of the photodissociated radicals (E_0) minus the internal energy of the photofragments (E_{int}) and the bond dissociation energy, D_0. The maximum translational energy for a particular dissociation channel is $h\upsilon - D_0$, as long as the radicals in question are internally cold with E_0 equal to zero.

The translational energy distribution from Figure 7.3 was used to simulate the gray contributions from Figure 7.2, obtained from the photodissociation of the ethyl nitrite precursor. The spectra in panels c) and d) of Figure 7.2 show the presence of two momentum matched contributions pertaining to the NO^+ ion generated from the ionization of the NO photofragment and the CH_2O^+ ion generated from the ionization of the CH_3CH_2O counterpart. These two contributions are momentum matched since they are formed in the same dissociation event. The TOF spectra shown for m/z = 43 and 26

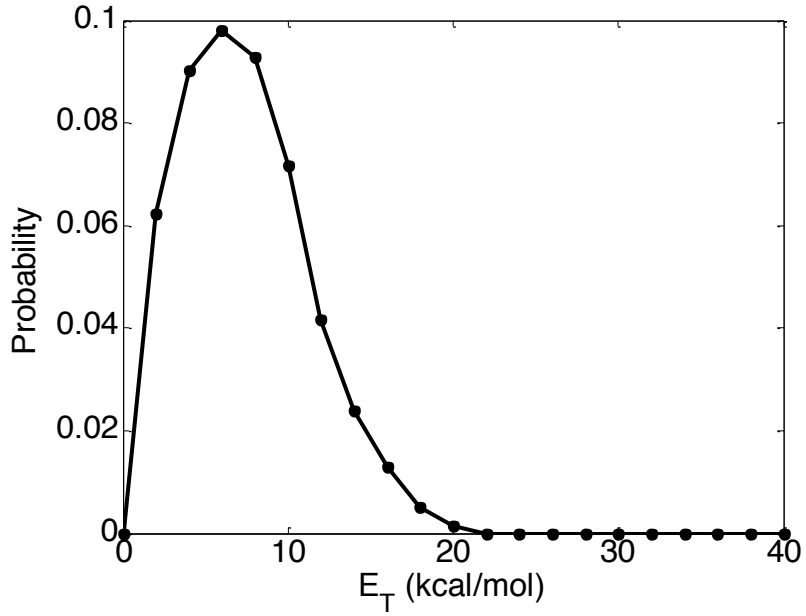

Fig. 7.4 Center-of-mass P(E_T) distribution from ethoxy radical photodissociation at 248 nm to form CH_3 + CH_2O. The maximum available energy for this channel is of about 106 kcal/mol.

contain only one gray fit since the NO photofragment does not dissociatively ionize to those mass to charge ratios. This P(E_T) distribution is consistent with previously published distribution observed for the photodissociation of ethyl nitrite at 248 nm.[201] The slow peak of the TOF spectra printed in panel d) of Figure 7.2 could not be simulated with the same translational energy distribution. This peak can be fit with the P(E_T) distribution from Figure 7.4. This distribution peaks at 6 kcal/mol and extends to about 22 kcal/mol, while the maximum available energy for this channel is more than 100 kcal/mol.

7.5 Discussion

This study was performed with two main objectives in mind: to determine a more precise branching ratio between the previously determined H loss and CH_3 loss channels, and to confirm the presence of the OH loss channel. Previous studies show the dissociation pathways accessible to the ethoxy radical as well as the dissociation pathways only accessible after isomerization to the α or β-hydroxyethyl radicals. The photodissociation data collected after excitation at 248 nm show the presence of at least one dissociation pathway pertaining to methyl radical loss to form formaldehyde, CH_2O. The translational energy distribution used to fit the spectrum obtained for m/z = 30 peaks at low translational energies and is consistent with statistical dissociation from the ground state surface.

The translational energy distribution is not consistent with the previously published translational energy distribution of Foulhaber *et al.*, since it is not consistent with

dissociation taking place on an excited state surface. Regardless of the dissociation mechanism, hydrogen atom loss is also expected, and the branching ratio with respect to methyl radical loss would reveal more about the mechanism of the dissociation process. With this in mind, TOF spectra were collected for *m/z* = 43 and represented in panels a) and b) of Figure 7.2, but only revealed the presence of a single peak that could be explained by ethyl nitrite dissociation, and thus simulated with the translational energy distribution from Figure 7.3. Hydrogen atom loss from the ethoxy radical proceeds to the formation of acetaldehyde whose parent ion can be detected at *m/z* = 44 (CH_3CHO^+). TOF spectra were collected at this mass to charge ratio, however, due to the high background signal caused by the presence of CO_2 gas in our detector chamber no photodissociation signal was observed. The maximum available energy for the acetaldehyde molecules produced along this pathway from excitation at 248 nm is of about 100 kcal/mol, which, if internal, is sufficient energy for acetaldehyde to undergo multiple dissociation pathways[56,202,203,204,205] including methane (CH_4) loss to form carbon monoxide. Secondary dissociation of the acetaldehyde formed by H atom loss could thus explain the lack of ethoxy photodissociation signal at *m/z* = 43. The CH_4 loss channel of acetaldehyde is the major dissociation pathway that leads to molecular products and is believed to take place along a roaming pathway.[206] Methane formation (CH_4) is not predicted from ethoxy or hydroxyethyl radical dissociation so it's detection would be direct proof of the hydrogen atom loss channel. Unfortunately, TOF spectra collected at *m/z* = 16 (CH_4^+) were not very revealing due to the high background caused by the residual O^+ signal present in our detector. The inability to obtain background free time-of-flight spectra for *m/z* = 44 and 16 directed us to synthesize the fully deuterated ethyl nitrate precursor. Deuterium atom loss would thus produce photodissociation signal at *m/z* = 48 (CD_3CDO^+) and perhaps *m/z* = 20 (CD_4^+) signal caused by secondary dissociation of the photolytically produced deuterated acetaldehyde. Unfortunately, photodissociation signal that could be attributed to hydrogen atom loss could not be detected, and thus it is not known whether the ethoxy radical decomposes along this dissociation pathway upon excitation at a wavelength of 248 nm.

Hydroxyl radical loss from the ethoxy radical would proceed to the formation of ethene and thus be detected at *m/z* ratio of 17 and 28. While the background is high at *m/z* = 28 from CO^+ and N_2^+ present in our detector, *m/z* = 26 is relatively free of background. The mass spectrum of ethene is known, and the signal at *m/z* = 26 ($C_2H_2^+$) is expected to be at least half as intense as the signal at *m/z* = 28.[28] The TOF spectra collected at this mass to charge ratio are represented in panels e) and f) of Figure 7.2 and did not reveal any new information about the photodissociation dynamics of the ethoxy radical. All of the TOF spectra obtained at *m/z* = 26 was adequately fit with the translational energy distribution shown in Figure 7.3.

The photodissociation dynamics observed at 248 nm excitation do not agree with previous work in our group. The spectra collected are consistent with statistical dissociation following internal conversion to the ground state surface. The lack of evidence for the hydrogen atom loss and hydroxyl radical loss channels does not prove that these pathways do not take place, it just raises further questions about the dissociation dynamics of this radical. The large amount of excess energy available

complicates the TOF spectra, making it impossible to differentiate other contributions. The dissociation dynamics of the ethoxy radical were also investigated at 193 nm, producing even more cluttered spectra. At 193 nm the photodissociation of ethyl nitrite is even more complex, containing a larger contribution from secondary dissociation of the ethoxy photofragments, thus making it even harder to distinguish the dissociation dynamics of the ethoxy radical. The use of a ninety degree photolysis source, as explained in Chapter 2, at 248 nm would be a great way of investigating the photodissociation dynamics of the ethoxy radicals since they can be produced in a background free environment.

Our study of the ethoxy radical was not limited to the work presented in this chapter. To fully understand the dissociation dynamics of this system the hydroxyethyl radicals[207,208,209,210,211,185,212] must also be produced and photodissociated. Attempts at producing the β–hydroxyethyl radical from pyrolysis or photolysis of 2-iodoethanol (ICH_2CH_2OH) resulted in failure. Detection of the OH loss channel in the photodissociation dynamics of this isomer would enforce the results observed for ethoxy photodissociation. While more than 10% of parent molecules were successfully depleted at 248 nm, radical photodissociation signal was not observed. It is believed that the large mass ratio between the iodine atom and the hydroxyethyl radical formed during photolysis causes the radicals to be scattered away from the molecular beam, thus never making it to the interaction region. This system would once again benefit from a non-collinear photolysis source.

7.6 Conclusions

The photodissociation dynamics of the ethoxy radical at 248 nm have been explored using photofragment translational spectroscopy. The ethoxy radicals were produced by the pyrolysis of ethyl nitrite entrained in a helium beam. Translational energy distributions were determined for the NO loss channel of ethyl nitrite and the CH_3 loss channel of the ethoxy radical. The P(E_T) distribution for the methyl loss channel extends to 22 kcal/mol and is attributed to the formation of formaldehyde on the ground state surface by means of a statistical process. Evidence for the previously observed hydrogen atom loss channel and hydroxyl radical loss channel were not obtained, raising additional questions about the dissociation dynamics of the ethoxy radical.

Chapter 8

Summary and Future Directions

The aim of this dissertation is to detail the workings of the B Machine and the photofragment translational spectroscopy studies of neutral free radicals. Hydrocarbon radicals are very reactive species, so their formation and investigation pose significant experimental challenges. The previous chapters reveal this struggle and various solutions implemented to achieve a better understanding of the dissociation dynamics of neutral free radicals. Radicals are very important intermediates that are created in extremely complex environments, such as combustion and atmospheric processes. The investigation of isolated radicals will extend our knowledge and increase the database so that we may better understand and model these environments.

Translational spectroscopy was used to investigate photochemistry of the phenyl and *tert*-butyl radicals formed in a collisionless environment by way of a supersonic expansion coupled to a flash pyrolysis or electrical discharge source. The photodissociation dynamics of *t*-butyl radical at 248 nm were show to consist of two dissociation pathways. One pathway proceeds by means of hydrogen atom loss to form isobutene, and the other by methyl radical loss to primarily form dimethylcarbene. Neither the translational energy distributions that characterize these processes nor the product branching ratio, which is close to unity, are consistent with statistical dissociation on the ground state surface of this system. In this study *t*-butyl radicals were formed by flash pyrolysis of azo-*t*-butane, a process that proved to be a wonderful system to characterize the functionality of the pyrolysis source. This work revealed that the chemistry of the source can be controlled by tuning the temperature. At high temperatures the azo-*t*-butane precursor was pyrolyzed into isobutene, while at intermediate temperatures it was pyrolyzed to form the *t*-butyl radical. This observation was confirmed by direct investigation of the photodissociation dynamics of isobutene, presented in chapter 4.

The photodissociation dynamics of the phenyl radical were probed at two wavelengths, 248 and 193 nm. Upon excitation at 248 nm only one dissociation pathway was observed, proceeding by way of hydrogen atom loss to form *ortho*-benzyne. At 193 nm, however, an additional dissociation pathway was observed, consisting of acetylene loss

subsequent to ring opening of the phenyl radical. This dissociation channel was found to dominate; a result that could not be explained with theoretically predicted ground state dynamics. This discord prompted a reinvestigation of the system, in which phenyl radicals were produced with different pyrolysis conditions and with a different source altogether, a grid discharge source. These measurements, however, were less than revealing due to congestion of the time-of-flight spectra caused by photodissociation signal originating from nitrosobenzene precursor contamination of the molecular beam.

While the research reported in this dissertation has provided insights into the photochemistries of a few neutral free radicals, there are countless radicals systems that can be produced and studied with the experimental techniques described herein. This new direction can provide unlimited subjects for collisionless dynamics investigations. This is especially true since neutral free radicals are not the only important intermediate that can be investigated. Carbenes, also known as diradicals, are present in much of the same environments as radicals, and they are just as reactive.[213] Carbenes can be produced with the same source designs used for radical production,[214,215] so they provide a very tangible future direction for the research being performed on B Machine.

Even though the tools necessary for future research with B Machine are mostly developed, changes to the experimental setup will be implemented in the future. A new commercial ionizer that can more efficiently produce lower energy electrons is awaiting installation. This ionizer has been assembled for more than four years, but was not installed because the detector of B Machine has not been vented since. When the ionizer filament will burn out the detector will be vented and the new ionizer installed. This installation will be postponed until then since the detector must be maintained under vacuum for several months before it can reach the low pressures currently achieved. The B Machine will also be automated in the near future with the installation of the Labview software to control and monitor timings, pressures, and the data acquisition software. To this end, a new data acquisition card and multichannel scalar have been purchased. These changes forebode a bright scientific future for the B Machine.

References

[1] T. Baer and W. L. Hase, *Unimolecular Reaction Dynamics: Theory and Experiments*. (Oxford University Press, Oxford, 1996).

[2] R. Schinke, *Photodissociation Dynamics*. (Cambridge University press, Cambridge, 1993).

[3] R. N. Zare and D. R. Herschbach, Proceedings of the Ieee **51** (1), 173 (1963).

[4] R. J. Vanbrunt and R. N. Zare, Journal of Chemical Physics **48** (9), 4304 (1968).

[5] G. E. Busch, Corneliu.Jf, R. T. Mahoney, R. I. Morse, Schlosse.Dw, and K. R. Wilson, Review of Scientific Instruments **41** (7), 1066 (1970).

[6] G. E. Busch and K. R. Wilson, Journal of Chemical Physics **56** (7), 3626 (1972).

[7] G. E. Busch and K. R. Wilson, Journal of Chemical Physics **56** (7), 3638 (1972).

[8] G. E. Busch and K. R. Wilson, Journal of Chemical Physics **56** (7), 3655 (1972).

[9] edited by A. G. Suits and R. E. Continetti (American Chemical Society, 2000).

[10] Y. T. Lee, J. D. McDonald, P. R. Lebreton, and D. R. Herschbach, Review Of Scientific Instruments **40** (11), 1402 (1969).

[11] J. C. Robinson, Ph. D. Thesis, University of California, Berkeley, 2002.

[12] A. M. Schmoltner, P. M. Chu, and Y. T. Lee, Journal of Chemical Physics **91** (9), 5365 (1989).

[13] A. M. Schmoltner, P. M. Chu, R. J. Brudzynski, and Y. T. Lee, Journal of Chemical Physics **91** (11), 6926 (1989).

[14] A. M. Schmoltner, S. Y. Huang, R. J. Brudzynski, P. M. Chu, and Y. T. Lee, Journal of Chemical Physics **99** (3), 1644 (1993).

[15] S. W. North, C. A. Longfellow, and Y. T. Lee, Journal of Chemical Physics **99** (6), 4423 (1993).

[16] S. North, D. A. Blank, and Y. T. Lee, Chemical Physics Letters **224** (1-2), 38 (1994).

[17] S. J. Goncher, N. E. Sveum, D. T. Moore, N. D. Bartlett, and D. M. Neumark, Journal of Chemical Physics **125** (22), 10 (2006).

[18] T. K. Minton, P. Felder, R. J. Brudzynski, and Y. T. Lee, Journal of Chemical Physics **81** (4), 1759 (1984).

[19] D. Krajnovich, L. J. Butler, and Y. T. Lee, Journal of Chemical Physics **81** (7), 3031 (1984).

[20] D. Krajnovich, Z. Zhang, L. Butler, and Y. T. Lee, Journal Of Physical Chemistry **88** (20), 4561 (1984).

[21] T. K. Minton, G. M. Nathanson, and Y. T. Lee, Journal of Chemical Physics **86** (4), 1991 (1987).

[22] S. W. North, D. A. Blank, J. D. Gezelter, C. A. Longfellow, and Y. T. Lee, Journal of Chemical Physics **102** (11), 4447 (1995).

[23] J. C. Robinson, W. Z. Sun, S. A. Harris, F. Qi, and D. M. Neumark, Journal of Chemical Physics **115** (18), 8359 (2001).
[24] J. C. Robinson, S. A. Harris, W. Z. Sun, N. E. Sveum, and D. M. Neumark, Journal of the American Chemical Society **124** (34), 10211 (2002).
[25] S. J. Goncher, D. T. Moore, N. E. Sveum, and D. M. Neumark, Journal of Chemical Physics **128** (11), 8 (2008).
[26] D. Proch and T. Trickl, Review of Scientific Instruments **60** (4), 713 (1989).
[27] G. O. Brink, Review of Scientific Instruments **37** (7), 857 (1966).
[28] Nist Webbook, http://webbook.nist.gov/chemistry/.
[29] D. R. Herschbach, Discussions of the Faraday Society (33), 149 (1962).
[30] R. N. Zare, Molecular Photochemistry **4**, 1 (1972).
[31] P. M. Kroger and S. J. Riley, Journal of Chemical Physics **67** (10), 4483 (1977).
[32] A. S. Sudbo, P. A. Schulz, D. J. Krajnovich, Y. T. Lee, and Y. R. Shen, Optics Letters **4** (7), 219 (1979).
[33] D. Krajnovich, Ph. D. Thesis, University of California, Berkeley, 1983.
[34] D. R. Cyr, D. J. Leahy, D. L. Osborn, R. E. Continetti, and D. M. Neumark, Journal of Chemical Physics **99** (11), 8751 (1993).
[35] D. L. Osborn, H. Choi, D. H. Mordaunt, R. T. Bise, D. M. Neumark, and C. M. Rohlfing, Journal of Chemical Physics **106** (8), 3049 (1997).
[36] R. T. Bise, A. A. Hoops, and D. M. Neumark, Journal of Chemical Physics **114** (20), 9000 (2001).
[37] A. E. Faulhaber, J. R. Gascooke, A. A. Hoops, and D. M. Neumark, Journal of Chemical Physics **124** (20), 8 (2006).
[38] D. E. Szpunar, J. L. Miller, L. J. Butler, and F. Qi, Journal of Chemical Physics **120** (9), 4223 (2004).
[39] L. R. McCunn, M. J. Krisch, K. Takematsu, L. J. Butler, and J. N. Shu, Journal of Physical Chemistry A **108** (39), 7889 (2004).
[40] J. L. Miller, M. J. Krisch, L. J. Butler, and J. N. Shu, Journal of Physical Chemistry A **109** (18), 4038 (2005).
[41] B. W. Alligood, C. C. Womack, D. B. Straus, F. R. Blase, and L. J. Butler, Journal of Chemical Physics **134** (19), 11 (2011).
[42] Y. R. Lee, C. L. Chiu, and S. M. Lin, Journal of Chemical Physics **100** (10), 7376 (1994).
[43] Y. Ohshima and Y. Endo, Journal of Molecular Spectroscopy **153** (1-2), 627 (1992).
[44] M. Nakajima, T. W. Schmidt, Y. Sumiyoshi, and Y. Endo, Chemical Physics Letters **449** (1-3), 57 (2007).
[45] E. Garand, T. I. Yacovitch, and D. M. Neumark, Journal of Chemical Physics **130** (6), 7 (2009).
[46] E. Garand and D. M. Neumark, Journal of Chemical Physics **135** (2), 8 (2011).
[47] P. Chen, S. D. Colson, and W. A. Chupka, Chemical Physics Letters **147** (5), 466 (1988).
[48] J. A. Blush, J. Park, and P. Chen, Journal of the American Chemical Society **111** (24), 8951 (1989).
[49] H. J. Deyerl, I. Fischer, and P. Chen, Journal of Chemical Physics **110** (3), 1450 (1999).
[50] H. J. Deyerl, I. Fischer, and P. Chen, Journal of Chemical Physics **111** (8), 3441 (1999).
[51] A. K. Vasiliou, K. M. Piech, B. Reed, Z. Xu, M. R. Nimlos, M. Ahmed, A. Golan, O. Kostko, D. L. Osborn, D. E. David, K. N. Urness, J. W. Daily, J. F. Stanton, and G. B. Ellison, Journal of Chemical Physics **137** (16), 164308 (14 pp.) (2012).
[52] R. A. Marcus and O. K. Rice, Journal of Physical and Colloid Chemistry **55** (6), 894 (1951).

[53] O. K. Rice and H. C. Ramsperger, Journal of the American Chemical Society **49**, 1617 (1927).
[54] O. K. Rice and H. C. Ramsperger, Journal of the American Chemical Society **50**, 617 (1928).
[55] L. S. Kassel, Journal Of Physical Chemistry **32** (2), 225 (1928).
[56] A. Vasiliou, K. M. Piech, X. Zhang, M. R. Nimlos, M. Ahmed, A. Golan, O. Kostko, D. L. Osborn, J. W. Daily, J. F. Stanton, and G. B. Ellison, Journal of Chemical Physics **135** (1), 5 (2011).
[57] C. K. Westbrook and F. L. Dryer, Progress in Energy and Combustion Science **10** (1), 1 (1984).
[58] E. H. Wilson, S. K. Atreya, and A. Coustenis, Journal of Geophysical Research-Planets **108** (E2), 5014 (2003).
[59] E. Herbst, H. H. Lee, D. A. Howe, and T. J. Millar, Monthly Notices of the Royal Astronomical Society **268** (2), 335 (1994).
[60] J. L. Miller, Journal of Physical Chemistry A **108** (12), 2268 (2004).
[61] T. A. Miller, Molecular Physics **104** (16-17), 2581 (2006).
[62] M. C. R. Symons, Tetrahedron Letters (3), 207 (1973).
[63] L. Bonazzola, N. Leray, and J. Roncin, Journal of the American Chemical Society **99** (25), 8348 (1977).
[64] D. E. Wood, L. F. Williams, R. F. Sprecher, and W. A. Lathan, Journal of the American Chemical Society **94** (17), 6241 (1972).
[65] P. J. Krusic and P. Meakin, Journal of the American Chemical Society **98** (1), 228 (1976).
[66] M. N. Paddonrow and K. N. Houk, Journal of the American Chemical Society **103** (17), 5046 (1981).
[67] J. Berkowitz, G. B. Ellison, and D. Gutman, Journal of Physical Chemistry **98** (11), 2744 (1994).
[68] P. W. Seakins, M. J. Pilling, J. T. Niiranen, D. Gutman, and L. N. Krasnoperov, Journal of Physical Chemistry **96** (24), 9847 (1992).
[69] J. Pacansky, J. S. Chang, and D. W. Brown, Tetrahedron **38** (2), 257 (1982).
[70] B. Schrader, J. Pacansky, and U. Pfeiffer, Journal of Physical Chemistry **88** (18), 4069 (1984).
[71] J. Pacansky, W. Koch, and M. D. Miller, Journal of the American Chemical Society **113** (1), 317 (1991).
[72] D. A. Parkes and C. P. Quinn, Chemical Physics Letters **33** (3), 483 (1975).
[73] H. R. Wendt and H. E. Hunziker, Journal of Chemical Physics **81** (2), 717 (1984).
[74] T. Koenig, T. Balle, and W. Snell, Journal of the American Chemical Society **97** (3), 662 (1975).
[75] J. Dyke, N. Jonathan, E. Lee, A. Morris, and M. Winter, Physica Scripta **16** (5-6), 197 (1977).
[76] F. A. Houle and J. L. Beauchamp, Journal of the American Chemical Society **101** (15), 4067 (1979).
[77] W. R. Stevens, S. H. Walker, N. S. Shuman, and T. Baer, Journal of Physical Chemistry A **114** (2), 804 (2010).
[78] E. L. Metcalfe, Journal of the Chemical Society (JUL), 3560 (1963).
[79] H. Schuh and H. Fischer, International Journal of Chemical Kinetics **8** (3), 341 (1976).
[80] A. R. Costello, J. R. L. Smith, M. S. Stark, and D. J. Waddington, Journal of the Chemical Society-Faraday Transactions **92** (19), 3497 (1996).

[81] M. J. Rossi and D. M. Golden, International Journal of Chemical Kinetics **15** (12), 1283 (1983).
[82] W. Tsang, Journal of Physical and Chemical Reference Data **19** (1), 1 (1990).
[83] V. D. Knyazev, I. A. Dubinsky, I. R. Slagle, and D. Gutman, Journal of Physical Chemistry **98** (20), 5279 (1994).
[84] J. A. Seetula and I. R. Slagle, Journal of the Chemical Society-Faraday Transactions **93** (9), 1709 (1997).
[85] H. Dilger, M. Stolmar, U. Himmer, E. Roduner, and I. D. Reid, Journal of Physical Chemistry A **102** (34), 6772 (1998).
[86] J. H. Choi, International Reviews in Physical Chemistry **25** (4), 613 (2006).
[87] M. P. Rissanen, S. L. Arppe, A. J. Eskola, M. M. Tammi, and R. S. Timonen, Journal of Physical Chemistry A **114** (14), 4811 (2010).
[88] X. Zheng and P. Blowers, AIChE Journal **52** (9), 3216 (2006).
[89] B. Noller, R. Maksimenka, I. Fischer, M. Armone, B. Engels, C. Alcaraz, L. Poisson, and J. M. Mestdagh, Journal of Physical Chemistry A **111** (10), 1771 (2007).
[90] M. Zierhut, W. Roth, and I. Fischer, Journal of Physical Chemistry A **108** (39), 8125 (2004).
[91] L. J. Butler and D. M. Neumark, Journal Of Physical Chemistry **100** (31), 12801 (1996).
[92] B. Negru, S. J. Goncher, A. L. Brunsvold, G. M. P. Just, D. Park, and D. M. Neumark, Journal of Chemical Physics **133** (7), 8 (2010).
[93] N. R. Daly, Review of Scientific Instruments **31** (3), 264 (1960).
[94] G. M. P. Just, B. Negru, D. Park, and D. M. Neumark, Physical Chemistry Chemical Physics **14** (2), 675 (2012).
[95] S. A. Harich, PHOTRAN (2003).
[96] A. M. Schmoltner, Ph. D. Thesis, University of California, Berkeley, 1989.
[97] V. Dias and J. Vandooren, Fuel **89** (9), 2633 (2010).
[98] S. Sato and R. J. Cvetanovic, Canadian Journal of Chemistry-Revue Canadienne De Chimie **36** (6), 970 (1958).
[99] T. Berndt and O. Boge, Journal of Atmospheric Chemistry **21** (3), 275 (1995).
[100] D. E. Woon and J. Y. Park, Icarus **202** (2), 642 (2009).
[101] G. Nam, I. V. Tokmakov, J. Park, and M. C. Lin, Proceedings of the Combustion Institute **31**, 249 (2007).
[102] B. Negru, D. Park, and D. M. Neumark, Abstracts of Papers of the American Chemical Society **239**, 1 (2012).
[103] J. N. Bradley and K. O. West, Journal of the Chemical Society-Faraday Transactions I **72**, 558 (1976).
[104] K. Brezinsky and F. L. Dryer, Combustion Science and Technology **45** (5-6), 225 (1986).
[105] J. C. Bauge, F. Battin-Leclerc, and F. Baronnet, International Journal of Chemical Kinetics **30** (9), 629 (1998).
[106] S. Santhanam, J. H. Kiefer, R. S. Tranter, and N. K. Srinivasan, International Journal of Chemical Kinetics **35** (8), 381 (2003).
[107] K. Yasunaga, Y. Kuraguchi, R. Ikeuchi, H. Masaoka, O. Takahashi, T. Koike, and Y. Hidaka, Proceedings of the Combustion Institute **32**, 453 (2009).
[108] A. Fahr, J. B. Halpern, and D. C. Tardy, Journal of Physical Chemistry A **111** (29), 6600 (2007).
[109] B. Negru, D. Park, and D. M. Neumark, Abstracts of Papers of the American Chemical Society **239**, 1 (2011).

[110] E. P. Carr and H. Stucklen, Journal of Chemical Physics **4** (12), 760 (1936).
[111] M. Caricato, G. W. Trucks, M. J. Frisch, and K. B. Wiberg, Journal of Chemical Theory and Computation **6** (2), 370 (2010).
[112] M. H. Palmer, A. J. Beveridge, I. C. Walker, and T. M. Abuain, Chemical Physics **117** (1), 51 (1987).
[113] K. B. Wiberg, A. E. de Oliveira, and G. Trucks, Journal of Physical Chemistry A **106** (16), 4192 (2002).
[114] Y. Li, H. L. Liu, Z. J. Zhou, X. R. Huang, and C. C. Sun, Journal of Physical Chemistry A **114** (35), 9496 (2010).
[115] W. L. Fitch and A. D. Sauter, Analytical Chemistry **55** (6), 832 (1983).
[116] M. J. Frisch, G. W. Trucks, H. B. Schlegel, G. E. Scuseria, M. A. Robb, J. R. Cheeseman, G. Scalmani, V. Barone, B. Mennucci, G. A. Petersson, H. Nakatsuji, M. Caricato, X. Li, H. P. Hratchian, A. F. Izmaylov, J. Bloino, G. Zheng, J. L. Sonnenberg, M. Hada, M. Ehara, K. Toyota, R. Fukuda, J. Hasegawa, M. Ishida, T. Nakajima, Y. Honda, O. Kitao, H. Nakai, T. Vreven, J. A. Montgomery, J. Peralta, J. E. , F. Ogliaro, M. Bearpark, J. J. Heyd, E. Brothers, K. N. Kudin, V. N. Staroverov, R. Kobayashi, J. Normand, K. Raghavachari, A. Rendell, J. C. Burant, S. S. Iyengar, J. Tomasi, M. Cossi, N. Rega, J. M. Millam, M. Klene, J. E. Knox, J. B. Cross, V. Bakken, C. Adamo, J. Jaramillo, R. Gomperts, R. E. Stratmann, O. Yazyev, A. J. Austin, R. Cammi, C. Pomelli, J. W. Ochterski, R. L. Martin, K. Morokuma, V. G. Zakrzewski, G. A. Voth, P. Salvador, J. J. Dannenberg, S. Dapprich, A. D. Daniels, Ö. Farkas, J. B. Foresman, J. V. Ortiz, J. Cioslowski, and F. J., Gaussian 09 (Gaussian, Inc., Wallingford, CT, 2009).
[117] T. Beyer and D. F. Swinehart, Communications of the ACM **16** (6), 379 (1973).
[118] R. G. Gilbert and S. C. Smith, *Theory of unimolecular and recombination reactions*. (Blackwell Scientific PublicationsJournal, Oxford, 1990).
[119] M. Frenklach, Physical Chemistry Chemical Physics **4** (11), 2028 (2002).
[120] H. Richter and J. B. Howard, Physical Chemistry Chemical Physics **4** (11), 2038 (2002).
[121] I. V. Tokmakov, G. S. Kim, V. V. Kislov, A. M. Mebel, and M. C. Lin, Journal of Physical Chemistry A **109** (27), 6114 (2005).
[122] M. Shukla, A. Susa, A. Miyoshi, and M. Koshi, Journal of Physical Chemistry A **112** (11), 2362 (2008).
[123] S. H. Bauer and C. F. Aten, Journal of Chemical Physics **39** (5), 1253 (1963).
[124] M. Braun-Unkhoff, P. Frank, and T. Just, Proceedings of the Combustion Institute **22**, 8 (1988).
[125] A. Laskin and A. Lifshitz, Proceedings of the Combustion Institute **26**, 6 (1996).
[126] A. Yokoyama, X. Zhao, E. J. Hintsa, R. E. Continetti, and Y. T. Lee, Journal of Chemical Physics **92** (7), 4222 (1990).
[127] J. C. Scaiano and L. C. Stewart, Journal of the American Chemical Society **105** (11), 3609 (1983).
[128] T. Yu and M. C. Lin, Journal of Physical Chemistry **99** (21), 8599 (1995).
[129] I. V. Tokmakov, J. Park, and M. C. Lin, Chemphyschem **6** (10), 2075 (2005).
[130] J. Park, G. J. Nam, I. V. Tokmakov, and M. C. Lin, Journal of Physical Chemistry A **110** (28), 8729 (2006).
[131] K. Tonokura, Y. Norikane, M. Koshi, Y. Nakano, S. Nakamichi, M. Goto, S. Hashimoto, M. Kawasaki, M. P. S. Andersen, M. D. Hurley, and T. J. Wallington, Journal of Physical Chemistry A **106** (24), 5908 (2002).

[132] R. I. Kaiser, L. Vereecken, J. Peeters, H. F. Bettinger, P. V. Schleyer, and H. F. Schaefer, Astronomy & Astrophysics **406** (2), 385 (2003).
[133] X. B. Gu and R. I. Kaiser, Accounts of Chemical Research **42** (2), 290 (2009).
[134] N. Ikeda, N. Nakashima, and K. Yoshihara, Journal of the American Chemical Society **107** (11), 3381 (1985).
[135] J. G. Radziszewski, Chemical Physics Letters **301** (5-6), 565 (1999).
[136] G. S. Kim, A. M. Mebel, and S. H. Lin, Chemical Physics Letters **361** (5-6), 421 (2002).
[137] M. Biczysko, J. Bloino, and V. Barone, Chemical Physics Letters **471** (1-3), 143 (2009).
[138] E. N. Sharp, M. A. Roberts, and D. J. Nesbitt, Physical Chemistry Chemical Physics **10** (44), 6592 (2008).
[139] V. Butcher, M. L. Costa, J. M. Dyke, A. R. Ellis, and A. Morris, Chemical Physics **115** (2), 261 (1987).
[140] J. Hrusak, D. Schroder, and S. Iwata, Journal Of Chemical Physics **106** (18), 7541 (1997).
[141] R. F. Gunion, M. K. Gilles, M. L. Polak, and W. C. Lineberger, International Journal of Mass Spectrometry and Ion Processes **117** (1-3), 601 (1992).
[142] N. E. Sveum, S. J. Goncher, and D. M. Neumark, Physical Chemistry Chemical Physics **8** (5), 592 (2006).
[143] J. C. Rienstra-Kiracofe, D. E. Graham, and H. F. Schaefer, Molecular Physics **94** (5), 767 (1998).
[144] L. K. Madden, L. V. Moskaleva, S. Kristyan, and M. C. Lin, Journal of Physical Chemistry A **101** (36), 6790 (1997).
[145] X. Lories, J. Vandooren, and D. Peeters, Physical Chemistry Chemical Physics **12** (15), 3762 (2010).
[146] M. J. S. Dewar, W. C. Gardiner, M. Frenklach, and I. Oref, Journal of the American Chemical Society **109** (15), 4456 (1987).
[147] S. P. Walch, Journal of Chemical Physics **103** (19), 8544 (1995).
[148] V. S. Rao and G. B. Skinner, Journal of Physical Chemistry **92** (9), 2442 (1988).
[149] H. Wang, A. Laskin, N. W. Moriarty, and M. Frenklach, Proceedings of the Combustion Institute **28**, 1545 (2000).
[150] C. M. Tseng, Y. M. Choi, C. L. Huang, C. K. Ni, Y. T. Lee, and M. C. Lin, Journal of Physical Chemistry A **108** (39), 7928 (2004).
[151] D. W. Kohn, H. Clauberg, and P. Chen, Review of Scientific Instruments **63** (8), 4003 (1992).
[152] M. N. R. Ashfold, G. A. King, D. Murdock, M. G. D. Nix, T. A. A. Oliver, and A. G. Sage, Physical Chemistry Chemical Physics **12** (6), 1218 (2010).
[153] W. L. Hase, S. L. Mondro, R. J. Duchovic, and D. M. Hirst, Journal Of the American Chemical Society **109** (10), 2916 (1987).
[154] S. E. Wheeler, W. D. Allen, and H. F. Schaefer, Journal of Chemical Physics **121** (18), 8800 (2004).
[155] S. J. Klippenstein and J. A. Miller, Journal of Physical Chemistry A **109** (19), 4285 (2005).
[156] Y. Song, M. Lucas, M. Alcaraz, J. S. Zhang, and C. Brazier, Journal of Chemical Physics **136** (4), 10 (2012).
[157] J. J. Orlando, G. S. Tyndall, and T. J. Wallington, Chemical Reviews **103** (12), 4657 (2003).
[158] R. Atkinson and S. M. Aschmann, Environmental Science & Technology **29** (2), 528 (1995).
[159] R. Atkinson, E. S. C. Kwok, J. Arey, and S. M. Aschmann, Faraday Discussions **100**, 23 (1995).

[160] R. Atkinson, International Journal of Chemical Kinetics **29** (2), 99 (1997).
[161] G. P. Brasseur, J. J. Orlando, and G. S. Tyndall, *Atmospheric Chemistry and Global Change*. (Oxford University Press, New York, 1999).
[162] K. Hoyermann, M. Olzmann, J. Seeba, and B. Viskolcz, Journal of Physical Chemistry A **103** (29), 5692 (1999).
[163] J. P. Reid, T. P. Marcy, S. Kuehn, and S. R. Leone, Journal of Chemical Physics **113** (11), 4572 (2000).
[164] L. Batt, International Journal of Chemical Kinetics **11** (9), 977 (1979).
[165] I. R. Slagle, D. Sarzynski, D. Gutman, J. A. Miller, and C. F. Melius, Journal of the Chemical Society-Faraday Transactions Ii **84**, 491 (1988).
[166] N. R. Greiner, Journal of Chemical Physics **53** (3), 1284 (1970).
[167] E. D. Morris, D. H. Stedman, and H. Niki, Journal of the American Chemical Society **93** (15), 3570 (1971).
[168] I. W. M. Smith and R. Zellner, Journal of the Chemical Society-Faraday Transactions Ii **69** (11), 1617 (1973).
[169] A. V. Pastrana and R. W. Carr, Journal of Physical Chemistry **79** (8), 765 (1975).
[170] J. N. Bradley, W. D. Capey, R. W. Fair, and D. K. Pritchard, International Journal of Chemical Kinetics **8** (4), 549 (1976).
[171] C. J. Howard, Journal of Chemical Physics **65** (11), 4771 (1976).
[172] A. C. Lloyd, K. R. Darnall, A. M. Winer, and J. N. Pitts, Journal of Physical Chemistry **80** (8), 789 (1976).
[173] R. Overend and G. Paraskevopoulos, Journal of Chemical Physics **67** (2), 674 (1977).
[174] F. P. Tully, Chemical Physics Letters **96** (2), 148 (1983).
[175] T. Klein, I. Barnes, K. H. Becker, E. H. Fink, and F. Zabel, Journal of Physical Chemistry **88** (21), 5020 (1984).
[176] R. Zellner and K. Lorenz, Journal of Physical Chemistry **88** (5), 984 (1984).
[177] C. Sosa and H. B. Schlegel, Journal of the American Chemical Society **109** (23), 7007 (1987).
[178] E. W. G. Diau and Y. P. Lee, Journal of Chemical Physics **96** (1), 377 (1992).
[179] T. Yamada, J. W. Bozzelli, and T. Lay, Journal of Physical Chemistry A **103** (38), 7646 (1999).
[180] M. C. Piqueras, R. Crespo, I. Nebot-Gil, and F. Tomas, Journal of Molecular Structure-Theochem **537**, 199 (2001).
[181] H. Hippler and B. Viskolcz, Physical Chemistry Chemical Physics **2** (16), 3591 (2000).
[182] R. S. Zhu, J. Park, and M. C. Lin, Chemical Physics Letters **408** (1-3), 25 (2005).
[183] P. A. Cleary, M. T. B. Romero, M. A. Blitz, D. E. Heard, M. J. Pilling, P. W. Seakins, and L. Wang, Physical Chemistry Chemical Physics **8** (48), 5633 (2006).
[184] J. P. Senosiain, S. J. Klippenstein, and J. A. Miller, Journal of Physical Chemistry A **110** (21), 6960 (2006).
[185] B. J. Ratliff, C. C. Womack, X. N. Tang, W. M. Landau, L. J. Butler, and D. E. Szpunar, Journal of Physical Chemistry A **114** (14), 4934 (2010).
[186] W. P. L. Carter, K. R. Darnall, A. C. Lloyd, A. M. Winer, and J. N. Pitts, Chemical Physics Letters **42** (1), 22 (1976).
[187] G. S. Tyndall, R. A. Cox, C. Granier, R. Lesclaux, G. K. Moortgat, M. J. Pilling, A. R. Ravishankara, and T. J. Wallington, Journal of Geophysical Research-Atmospheres **106** (D11), 12157 (2001).

[188] O. Setokuchi, S. Matuzawa, and Y. Shimizu, Chemical Physics Letters **284** (1-2), 19 (1998).
[189] C. Fittschen, P. Devolder, S. Dusanter, and B. Lemoine, Chemical Physics Letters **417** (1-3), 154 (2006).
[190] A. Miyoshi, H. Matsui, and N. Washida, Journal Of Physical Chemistry **94** (7), 3016 (1990).
[191] F. Caralp, P. Devolder, C. Fittschen, N. Gomez, H. Hippler, R. Mereau, M. T. Rayez, F. Striebel, and B. Viskolcz, Physical Chemistry Chemical Physics **1** (12), 2935 (1999).
[192] Y. P. Park, K. W. Kang, S. H. Jung, and J. H. Choi, Physical Chemistry Chemical Physics **12** (26), 7098 (2010).
[193] R. A. Cox, K. F. Patrick, and S. A. Chant, Environmental Science & Technology **15** (5), 587 (1981).
[194] D. Gutman, N. Sanders, and J. E. Butler, Journal Of Physical Chemistry **86** (1), 66 (1982).
[195] P. Devolder, Journal of Photochemistry and Photobiology a-Chemistry **157** (2-3), 137 (2003).
[196] H. Choi, R. T. Bise, and D. M. Neumark, Journal of Physical Chemistry A **104** (45), 10112 (2000).
[197] A. E. Faulhaber, D. E. Szpunar, K. E. Kautzman, and D. M. Neumark, Journal of Physical Chemistry A **109** (45), 10239 (2005).
[198] A. I. Vogel, (Longmans, London, 1956).
[199] S. A. Harich, (1989).
[200] A. M. Wodtke, (2004).
[201] P. Felder, B. A. Keller, and C. S. Effenhauser, Berichte Der Bunsen-Gesellschaft-Physical Chemistry Chemical Physics **92** (3), 426 (1988).
[202] O. K. Abou-Zied and J. D. McDonald, Journal of Chemical Physics **109** (4), 1293 (1998).
[203] K. C. Thompson, D. L. Crittenden, S. H. Kable, and M. J. T. Jordan, Journal of Chemical Physics **124** (4), 15 (2006).
[204] L. Rubio-Lago, G. A. Amaral, A. Arregui, J. G. Izquierdo, F. Wang, D. Zaouris, T. N. Kitsopoulos, and L. Banares, Physical Chemistry Chemical Physics **9** (46), 6123 (2007).
[205] B. R. Heazlewood, S. J. Rowling, A. T. Maccarone, M. J. T. Jordan, and S. H. Kable, Journal of Chemical Physics **130** (5), 8 (2009).
[206] B. R. Heazlewood, M. J. T. Jordan, S. H. Kable, T. M. Selby, D. L. Osborn, B. C. Shepler, B. J. Braams, and J. M. Bowman, Proceedings of the National Academy of Sciences of the United States of America **105** (35), 12719 (2008).
[207] C. Anastasi, V. Simpson, J. Munk, and P. Pagsberg, Journal of Physical Chemistry **94** (16), 6327 (1990).
[208] S. P. Sapers and W. P. Hess, Journal of Chemical Physics **97** (5), 3126 (1992).
[209] V. A. Shubert and S. T. Pratt, Journal of Physical Chemistry A **114** (42), 11238 (2009).
[210] L. W. Edwards, M. Ryazanov, H. Reisler, and S. J. Klippenstein, Journal of Physical Chemistry A **114** (17), 5453 (2010).
[211] E. Kamarchik, L. Koziol, H. Reisler, J. M. Bowman, and A. I. Krylov, Journal of Physical Chemistry Letters **1** (20), 3058 (2010).
[212] C. C. Womack, B. J. Ratliff, L. J. Butler, S. H. Lee, and J. J. M. Lin, Journal of Physical Chemistry A **116** (24), 6394 (2012).
[213] M. Albrecht, Science **326** (5952), 532 (2009).
[214] H. P. Reisenauer, J. Romanski, G. Mloston, and P. R. Schreiner, European Journal of Organic Chemistry (21), 4813 (2006).

[215] P. R. Schreiner, H. P. Reisenauer, F. C. Pickard, A. C. Simmonett, W. D. Allen, E. Matyus, and A. G. Csaszar, Nature **453** (7197), 906 (2008).